JAERI-M
93-141

TWO-DIMENSIONAL OVER-ALL NEUTRONICS ANALYSIS OF THE ITER DEVICE

July 1993

Sergei ZIMIN[*1], Hideyuki TAKATSU
Seiji MORI[*2], Koichi MAKI[*3], Yasushi SEKI
Satoshi SATOH and Eisuke TADA

日本原子力研究所
Japan Atomic Energy Research Institute

JAERI-Mレポートは，日本原子力研究所が不定期に公刊している研究報告書です。
入手の問合わせは，日本原子力研究所技術情報部情報資料課（〒319－11茨城県那珂郡東海村）あて，お申しこしください。なお，このほかに財団法人原子力弘済会資料センター（〒319-11茨城県那珂郡東海村日本原子力研究所内）で複写による実費頒布をおこなっております。

JAERI-M reports are issued irregularly.
Inquiries about availability of the reports should be addressed to Information Division, Department of Technical Information, Japan Atomic Energy Research Institute, Tokai-mura, Naka-gun, Ibaraki-ken 319-11, Japan.

編集兼発行　日本原子力研究所
印　　刷　日立高速印刷株式会社

Two-dimensional Over-all Neutronics Analysis of the ITER Device

Sergei ZIMIN[*1], Hideyuki TAKATSU, Seiji MORI[*2]
Koichi MAKI[*3], Yasushi SEKI[+], Satoshi SATOH[+]
and Eisuke TADA[+]

Department of ITER Project
Naka Fusion Research Establishment
Japan Atomic Energy Research Institute
Naka-machi, Naka-gun, Ibaraki-ken

(Received June 10, 1993)

The present work attempts to carry out a comprehensive neutronics analysis of the International Thermonuclear Experimental Reactor (ITER) developed during the Conceptual Design Activities (CDA). The two-dimensional cylindrical over-all calculational models of ITER CDA device including the first wall, blanket, shield, vacuum vessel, magnets, cryostat and support structures were developed for this purpose with a help of the DOGII code. Two dimensional DOT 3.5 code with the FUSION-40 nuclear data library was employed for transport calculations of neutron and gamma ray fluxes, tritium breeding ratio (TBR) and nuclear heating in reactor components. The induced activity calculational code CINAC was employed for the calculations of exposure dose rate after reactor shutdown around the ITER CDA device.

The two-dimensional over-all calculational model includes the design specifics such as the pebble bed Li_2O/Be layered blanket, the thin double wall vacuum vessel, the concrete cryostat integrated with the

+ Department of Fusion Engineering Research
*1 Research Fellow
*2 On leave from Kawasaki Heavy Industries, Ltd.
*3 Hitachi Ltd.

over-all ITER design, the top maintenance shield plug, the additional ring biological shield placed under the top cryostat lid around the above-mentioned top maintenance shield plug etc. All the above-mentioned design specifics were included in the employed calculational models. Some alternative design options, such as the water-rich shielding blanket instead of lithium-bearing one, the additional biological shield plug at the top zone between the poloidal field (PF) coil No.5 and the maintenance shield plug, were calculated as well.

Much efforts have been focused on analyses of obtained results. These analyses aimed to obtain necessary recommendations on improving the ITER CDA design.

Keywords : ITER, Neutronics, Neutron Transport Calculations, Biological Shield, Neutron Flux, Exposure Dose Rate, Nuclear Heating, Blanket, Concrete Cryostat, Tritium Breeding Ratio, Induced Activity.

ITERの2次元全体モデルによるニュートロニクス計算

日本原子力研究所那珂研究所ITER開発室
Sergei ZIMIN[*1]・高津　英幸・森　清治[*2]・真木　紘一[*3]
関　泰[+]・佐藤　聡[+]・多田　栄介[+]

（1993年6月10日受理）

国際熱核融合炉（ITER）の概念設計活動（CDA）により設定された炉構造に対してニュートロニクス解析を実施した。炉全体の2次元モデルをDOT3.5用入力データ自動作成パソコンプログラムDOG－Ⅱを用いて作成した。中性子およびガンマ線フラックス分布，トリチウム増殖比，核発熱を2次元S_N輸送計算コードDOT3.5と核群定数ライブラリーFUSION－40を用いて計算した。また炉停止後の炉周辺の生体線量率分布を求めるための誘導放射能計算をCINACコードにより実施した。

ITER CDA終了後，原研において，Li_2O／Beペブル層状ブランケット，薄肉2重壁真空容器，コンクリート製クライオスタット，上部メインテナンスポート遮蔽プラグ等の設計改良作業が続けられた。今回の計算にはこれらの設計が考慮されている。また代表設計以外にいくつかの代替案，例えばトリチウム増殖ブランケットに替えての遮蔽ブランケットの採用，No.5ポロイダルコイルと上部遮蔽プラグ間に追加遮蔽プラグの設置等についての解析も実施した。

計算結果を慎重に検討することにより，設計をさらに改良するための知見を得ることができた。

那珂研究所：〒311－01 茨城県那珂郡那珂町大字向山801－1
＋　核融合工学部
＊1 リサーチフェロー
＊2 出向職員（川崎重工業株式会社）
＊3 株式会社日立製作所

Contents

目　　次

1. Introduction.

The ITER "Conceptual Design Activities" (CDA) [1] began in the spring of 1988 and ended in December 1990. The objectives of these activities were to develop the design of ITER, to perform a safety and environmental analysis, to define the future research and development needs, and to estimate cost, manpower, and schedule for detailed engineering design, construction and operation. Because of the success of the CDA, the Parties are now considering continuation of ITER into the next phase, called the "Engineering Design Activities" (EDA) [2] ; this phase would include the expanded engineering and R&D efforts needed to prepare for initiation of the construction of ITER by the late 1990's.

Therefore, there is a demand on the progress in technology as on advances in plasma physics. Thus, much efforts have been focused during the past years on a number of areas of technology. Among the technology areas regarded as of great importance for realization of ITER are the development of large superconducting magnets, a shield and blanket, a vacuum vessel, a first wall etc.

Numerous works were done to support the neutronics design of ITER blanket and shield during ITER CDA. Among them numerous 1-D, 2-D and 3-D neutron transport calculations listed in Ref. 3 were carried out for different zones of ITER machine, namely inboard, top/bottom, outboard, recess, NBI duct etc. However the neutron transport calculations of ITER over-all configurations are necessary to give a designer the information on both total heating in the ITER first wall, blanket shield and vacuum vessel and fast neutron flux and dose during operation and after shutdown at every zone of ITER over-all configuration.

Such an analysis was done in Ref. 4 for a swimming pool-type tokamak reactor and in Ref. 5 for the FER [6]. However, because of geometrical and compositional differences, this information could not be used directly for ITER neutronics analyses. Therefore we decided to run a number of neutron transport calculations for the ITER CDA over-all configuration to provide some useful information for the ITER EDA.

2. Calculational conditions.

The general three-dimensional view of ITER CDA is shown in Fig. 2.1. The main parts of ITER CDA are shown in Fig. 2.1 as well.

According to the reference ITER CDA [3] concept there is only 151 cm of total outboard bulk shield thickness in the mid-plane and the double wall steel cryostat with the effective steel thickness of 7 cm, thus 158 cm in the total shield thickness. However, a need of a biological shield outside the cryostat has been stressed by some results of ITER CDA biological shield analyses presented during [5, 7-9] and after [10] ITER CDA Phase of work.

Possible approaches to a biological shield concept have been discussed in Ref. 10. The main feature of Japanese approach to the ITER CDA biological shield is the idea to joint functions of a cryostat and biological shield. In this case, the relatively thick concrete cryostat with continuous metallic inner liner was chosen [10] as the Japanese proposal for the ITER EDA, namely 180 cm thick concrete cryostat. (The same approach was chosen for NET : "The outer boundary to the NET basic machine is formed by an ~ 1.6-m-thick concrete biological shield" [11]). The design description of cryostat employed in this study is shown in Ref. 12. This cryostat was included in the calculational models employed in this study.

Figure 2.2 shows the two poloidal cross sections at different toroidal locations, namely across toroidal field (TF) coil /cut Nº 1/ and between TF coils /cut Nº 2/.

Both cuts were shifted by some degrees (as shown in Fig. 2.2) from the symmetry axes of a TF coil and cavity 2, respectively. Thus, the first cut was not done across the reinforce rib shown in Fig. 2.2. The second cut was done across the cavities number 1 and 2 (see Fig. 2.2). It is expected to give the upper bound biological dose at the location of cryostat and the most pessimistic from the view point of a biological shield analysis.

Three main geometrical models were calculated :

1) Upper half with TF coil (cut Nº 1) is shown in Fig. 2.3 ;

2) Upper half with inboard leg of TF coil (without outboard leg), with top port and without horizontal port (cut Nº 2) is shown in Fig. 2.4 ;
3) The same as (2), but

a) the SS/H_2O-shielding blanket was employed instead of the reference layered pebble bed beryllium/Li_2O one;

b) the additional steel-bearing shield was incorporated between the poloidal field (PF) coil Nº5 (PU5) and top shield plug, namely zone 43 in Fig. 2.5.

Nuclear densities of component materials employed for the transport calculations are shown in Table 2.1.

The two-dimensional cylindrical model was employed for calculations. This two-dimensional cylindrical geometry is a rather realistically description of the ITER CDA whose plasma elongation is almost 2 [1], e.g. the concrete cryostat walls, cryostat lids and central solenoid are actually cylinders. However, some simplifications were devised for the calculational models in Figs. 2.3-2.5. The main among them is the absence of the horizontal port.

There are two reasons why the horizontal port (NBI duct) was not included in the above-mentioned calculational models Nº 1-3.
1) The employed cylindrical geometrical model and the NBI duct are not coaxial cylinders. There is 90° angle between the above-mentioned axes. Thus, it is extremely difficult to include the NBI duct in the calculational models Nº 1-3.
2) The biological shield around NBI duct was studied in Ref. 13. Correspondingly, the contour map of gamma-ray dose rate in a week after reactor shutdown was obtained and presented during ITER CDA [13].

Other simplifications could be summarized as follows :
1) Most zones in employed models were homogenized, namely the blanket, semi-permanent shield, vacuum vessel, divertor, PF coils etc.
2) The volumes of zone Nº 3 in Fig. 2.3 and Nº 20 in Figs. 2.4, 2.5 (divertor) were intentionally increased. However, this increase was properly compensated by corespondent homogenization of material

of this zone and a void fraction. The same procedure was done for the zone N° 33 in Fig. 2.3 (steel wall of 10 cm thickness). Above measures had to be done to avoid some difficulties during input data preparations.

Other features of the above-mentioned calculational models are :

1) The layered pebble bed beryllium/Li_2O blanket type developed in Japan after CDA [14] (The inboard and outboard blankets consist of one and three lithium layers, respectively.) ;
2) The additional ring biological shield placed under the top cryostat lid (discussed below, in the paragraph 3.2) ;
3) The water-rich (80% H_2O + 20% SS) shielding blanket was employed for some calculations to compare its shielding effectiveness with the reference layered pebble bed beryllium/Li_2O composition [14].
4) Some other design features developed in Japan after ITER CDA [12, 15, 16] were employed in the above calculational models as well, e.g. the bellows in the top zone of ITER maintenance port etc.
5) The design of ITER CDA was not sufficiently specified for over-all neutron transport calculations of exposure dose rate around the ITER CDA fusion device. The design proposal of important zone 2 in Fig. 2.4, for example, varied in Ref. 18 from "void" (the EC proposal) to "about 30 v/o of steel" (Japanese proposal). Corresponding designs are shown in Ref. 17. The most conservative "void" option was employed in this study to get most pessimistic results.

In principle, a precise analysis of neutron/gamma fluxes attenuation in the ITER configuration can be done by Monte Carlo method in a three-dimensional geometry. However, a calculational model for such an analysis would be extremely difficult to set up and very expensive, if possible, to run. Therefore, the S_N method is preferable for these calculations. This method has been proved effective for the geometrically simple but very thick shield regions with many orders of neutron flux attenuation. It provides solutions of a given accuracy in all the ranges of structural variations under

discussion, even for cases of deep penetration with a strong anisotropy in scattering. Thus the most important advantage of the method is the possibility to get the responses in all mesh intervals [18].

Therefore the DOT3.5 code [19] with the FUSION-40 (42 neutron and 21 gamma-ray energy groups) nuclear data library [20] was used in this study. The P_3-S_8 approximation and 159 x 159 spatial mesh points are employed in the calculation of neutron and gamma ray fluxes. However, it is very complicated job to set up the above-mentioned calculational model. Therefore, the newly developed DOG-II code [21] was used to generate input data for DOT3.5 code.

The main feature of the DOG-II code is the necessity to generate input data for "grid" that is more simple than for "mesh", directly in the DOT3.5 code. The "grid" input data are used in the DOG-II code for generating automatically "mesh" input data for the DOT3.5 code. The "grid" employed for calculations in this study, for example, consists of 32 x 36 spatial grid points only, in comparison with above-mentioned 159 x 159 spatial mesh points of final DOT3.5 input data. Thus, the DOG-II code being used in this study is very helpful to set up a large geometrical model for the DOT3.5 code and can save much time to be spent on an input data generation. The APPLE-3 code [22] is used to plot the calculational model and contour maps of dose rate and flux distributions.

The induced activity calculation code system THIDA [23] developed in Japan Atomic Energy Research Institute (JAERI) was employed for the calculation of exposure dose rate around the ITER CDA device. This code consists of radiation transport codes, an induced activity calculation code and data libraries for transmutation and decay chains, transmutation cross-sections and delayed gamma-ray emission spectra. (The decay heat in a first wall/blanket/shield which necessitates an adequate removal measure in case of an accident like a loss of coolant or during maintenance operation at shutdown can be calculated with the THIDA system as well.)

However, the standard induced activity calculational code ACT4 included in THIDA system demands rather large calculational time.

On the other hand, a new method and accompanying computer code CINAC-V4 [24] have been developed for the calculation of neutron-induced transmutation, radioactivity and afterheat. The new code CINAC-V4 is 50 time faster than the code ACT4. Thus, the CINAC-V4 code was used in this study instead of the ACT4 code.

Therefore, the procedure of shutdown dose calculations can be described as follows :

1) The neutron flux /obtained in over-all neutron transport calculations by DOT3.5/ is used as an input for the code CINAC-V4. This code calculates the induced activity, the approximate decay heat* and the delayed gamma-ray source after reactor shutdown ;

2) The delayed gamma-ray source serves as the input for the transport calculation /DOT3.5 code/ of the delayed gamma-ray flux after shutdown.

3) Finally, the obtained gamma-ray flux is converted to shutdown dose rate by the APPLE-3 code.

All neutron transport calculations in this study were carried out for the upper half of ITER CDA. The neutron source was normalized to 1 GW thermonuclear power of ITER CDA. Thus, the 0.5 GW thermonuclear power was used for normalization in our calculations of the upper half of ITER CDA. The distribution of neutron source generated by fusion reactions was calculated by a special code [25] developed for this purposes at JAERI.

It should be underlined that about 70 hours of computing time (FACOM M-780) were spent for the neutron and gamma-ray transport calculations presented in this report. The neutron fluxes for the calculational models Nº 2 and 3 have been the most difficult to converge and, correspondingly, time-consuming cases. It is explained by large gradients of neutron fluxes in the models because of numerous void inhomogeneities incorporated in the above-mentioned models.

---

* This decay heat is approximate because delayed gamma-ray is assumed to deposit its energy at the location where it is generated.

Table 2.1 Atomic number densities of component materials.

($10^{24}cm^{-3}$)

No.	Material		Element		Number Density
1	Plasma	241 ~ 246	$^{2}H_2$	7 ~ 12	1.000×10^{-10}
2	316S S	247 ~ 252	C	55 ~ 60	0.0×10^{0}
			Mn	145 ~ 150	1.662×10^{-3}
			Cr	139 ~ 144	1.575×10^{-2}
			Ni	163 ~ 168	9.848×10^{-3}
			Fe	151 ~ 156	5.869×10^{-2}
3	H_2O	253 ~ 258	H	1 ~ 6	6.686×10^{-2}
			O	67 ~ 72	3.343×10^{-2}
4	Air	259 ~ 264	N	61 ~ 66	4.220×10^{-5}
			O	67 ~ 72	1.170×10^{-5}
5	Natural Li_2O	265 ~ 270	^{6}Li	25 ~ 30	5.118×10^{-3}
			^{7}Li	31 ~ 36	6.385×10^{-2}
			O	67 ~ 72	3.4484×10^{-2}
6	Be	277 ~ 282	^{9}Be	37 ~ 42	1.236×10^{-1}
7	Cu	295 ~ 300	Cu	169 ~ 174	8.464×10^{-2}
8	Vacuum	301 ~ 306	Air	259 ~ 264	1.000×10^{-8}
9	EPOXY ($C_{16}H_{20}O_3$)	307 ~ 312	C	55 ~ 60	4.478×10^{-2}
			H	1 ~ 6	4.976×10^{-2}
			O	67 ~ 72	7.464×10^{-3}
10	C	319 ~ 324	C	55 ~ 60	8.023×10^{-2}
11	He (gas)	325 ~ 330	^{4}He	19 ~ 24	2.6888×10^{-5}
12	He (liquid)	331 ~ 336	^{4}He	19 ~ 24	1.8963×10^{-2}
13	Concrete (σ = 2.22g/cm^3)	343 ~ 348	Na	79 ~ 84	6.935×10^{-4}
			Fe	151 ~ 156	6.6872×10^{-4}
			O	67 ~ 72	4.123×10^{-2}
			C	55 ~ 60	3.004×10^{-4}
			H	1 ~ 6	6.364×10^{-3}
			Si	97 ~ 102	1.680×10^{-2}
			K	115 ~ 120	2.734×10^{-4}
			Ca	121 ~ 126	3.301×10^{-3}

THE ITER DEVICE

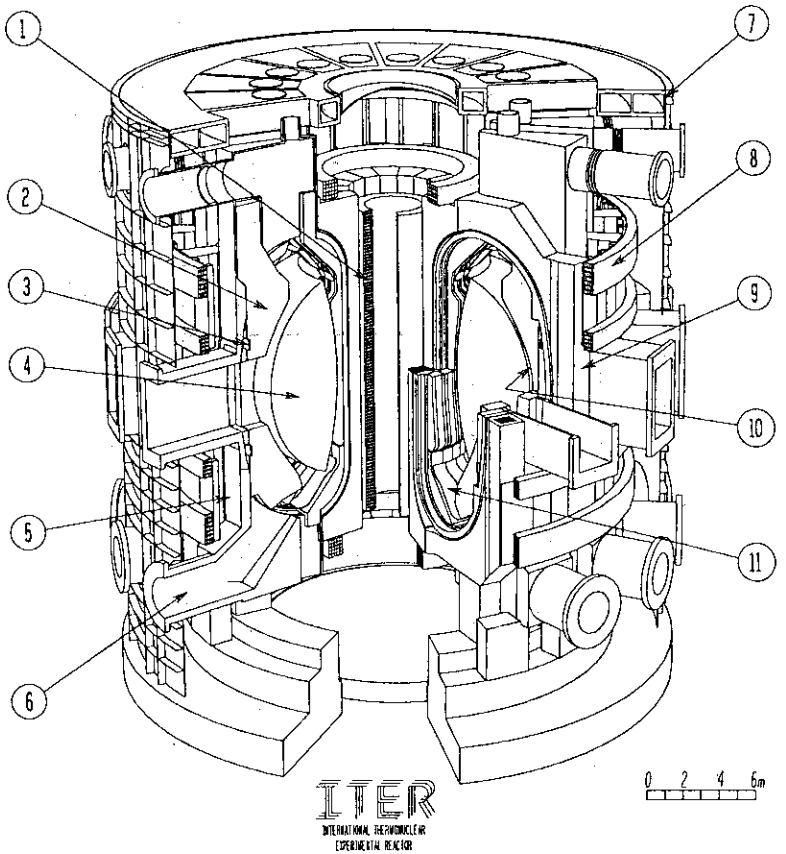

1- CENTRAL SOLENOID
2- SHIELD/BLANKET
3- ACTIVE COIL
4- PLASMA
5- VACUUM VESSEL-SHIELD
6- PLASMA EXHAUST
7- CRYOSTAT
8- POLOIDAL FIELD COILS
9- TOROIDAL FIELD COILS
10- FIRST WALL
11- DIVERTOR PLATES

Fig. 2.1 Overall view of ITER basic machine

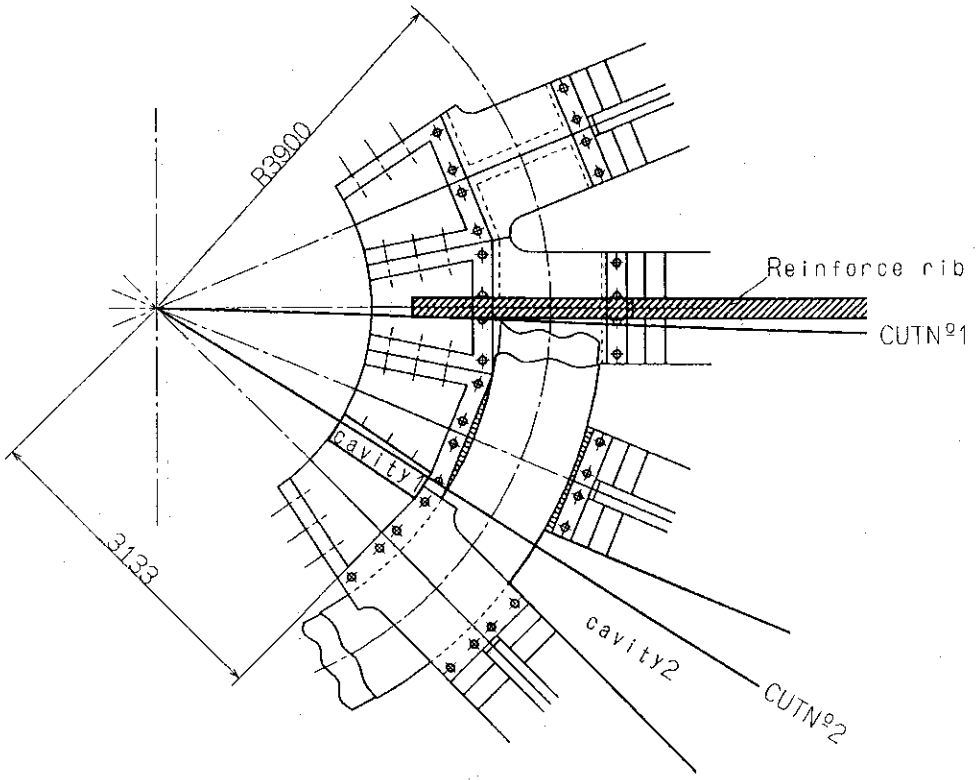

Fig. 2.2 Top view of ITER device.

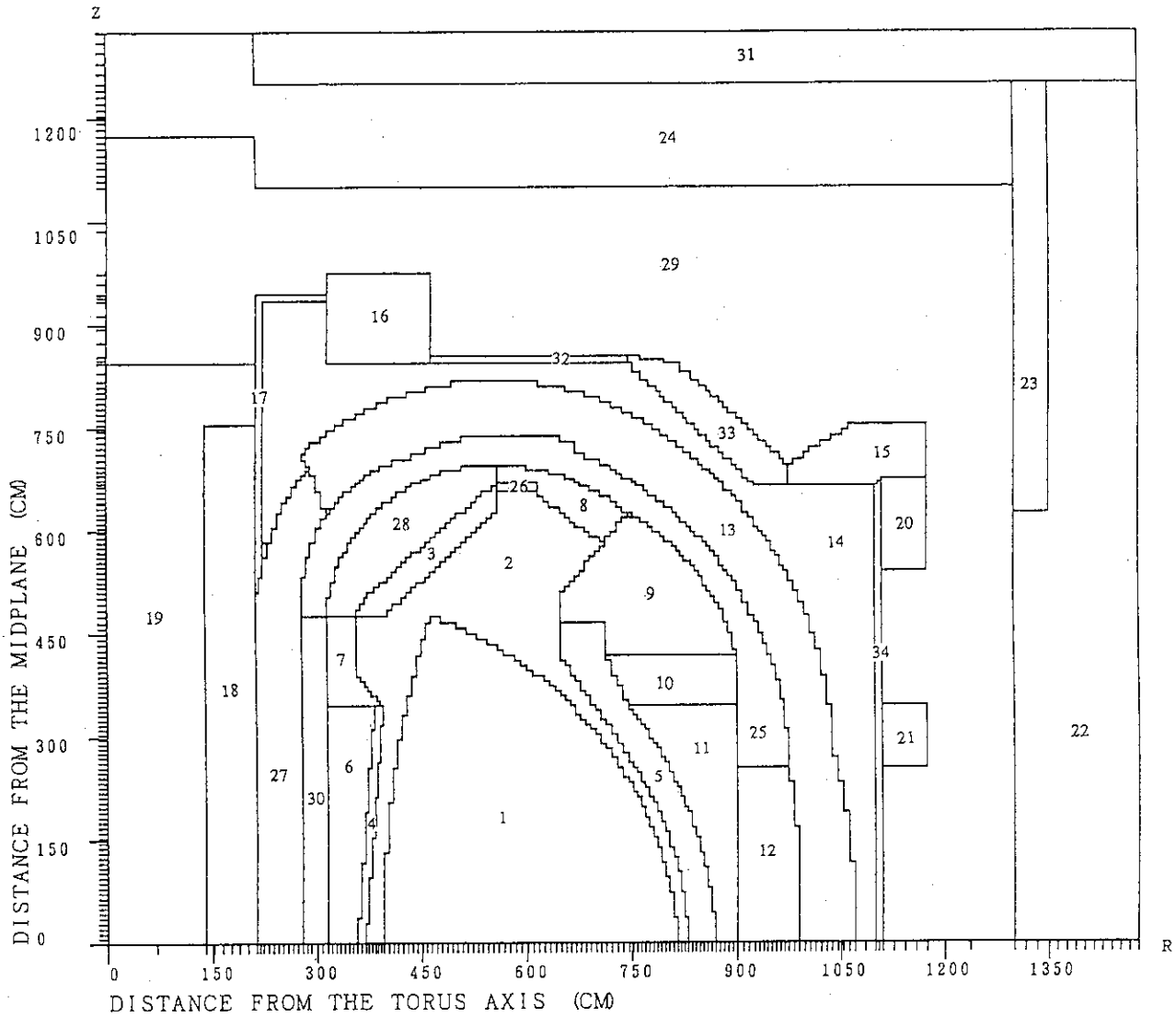

Fig. 2.3 R-Z calculational model (No.1) of ITER CDA.
1-Plasma (14-MeV neutron source); 2,14,29,31-Void; 3-Divertor (21% SS, 6% H_2O, 6% C); 4-Inboard blanket (15% SS, 6% H_2O, 60% Be, 19% Li_2O); 5-Outboard blanket (18% SS, 9% H_2O, 60% Be, 13% Li_2O); 6,7,8-Shielding (80% SS, 20% H_2O); 9-Shielding (20% SS, 80% H_2O); 10,11-Shielding (50% SS, 50% H_2O); 12-Vacuum vessel (61% SS, 26% H_2O); 13-TF coil (72% SS, 14% Cu, 8% He, 4.8% $C_{12}H_{20}O_3$*, 1.2% Nb); 15-Out-vessel zone (100% SS); 16-PF coil (66% SS, 17% Cu, 10% He, 5.8% $C_{12}H_{20}O_3$, 1.2% Nb); 17,23,32, 34-Walls (100% SS); 18,20,21-PF coils (26% SS, 30% Cu, 17% He, 10% $C_{12}H_{20}O_3$, 2.6% Nb); 19-Central solenoid (8% SS); 22-Cryostat (4.43% SS, 95.57% Concrete*); 24-Cryostat lid (20% SS, 80% H_2O); 25-Shielding (45.5% SS, 19.5% H_2O); 26-Divertor (14% SS, 70% H_2O, 16% C); 27-TF coil (66% SS, 17% Cu, 10% He, 5.8% $C_{12}H_{20}O_3$, 1.2% Nb); 28-Shielding (20% SS, 80% H_2O); 30-Vacuum vessel (52.5% SS, 22.5% H_2O); 33-Wall (20% SS).

* Nuclear densities of epoxy ($C_{12}H_{20}O_3$) and concrete see in Table 2.1.

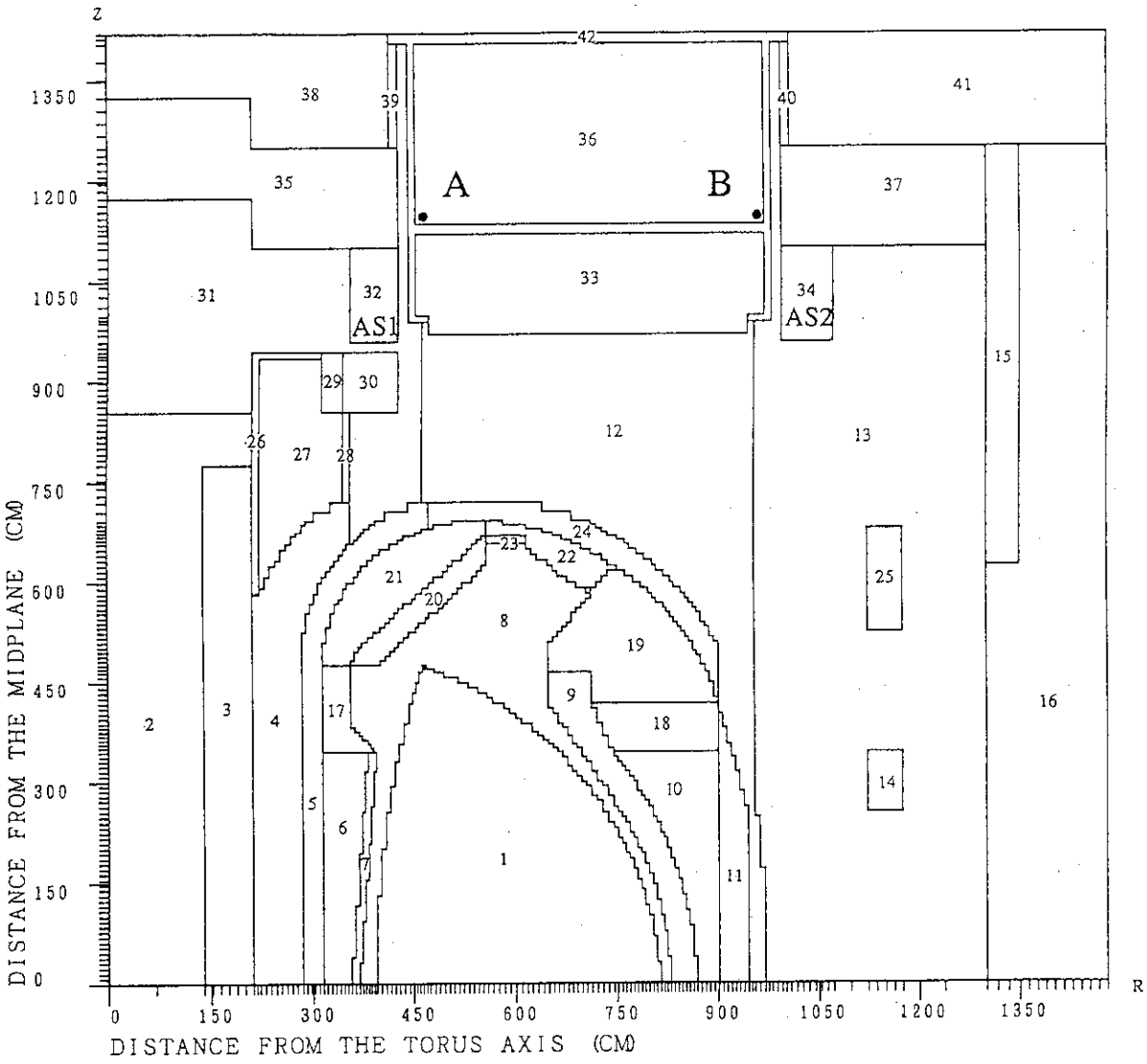

Fig. 2.4 R-Z calculational model (No.2) of ITER CDA.
1-Plasma (14-MeV neutron source); 2-Central solenoid (8% SS); 3,14,25, 30-PF coils (26% SS, 30% Cu, 17% He, 10% $C_{12}H_{20}O_3$*, 2.6% Nb); 4,5,11-Vacuum vessel (61% SS, 26% H_2O); 10,18-Shielding (50% SS, 50% H_2O); 7-Inboard blanket (15% SS, 6% H_2O, 60% Be, 19% Li_2O); 8,13,24,27,31, 33,36,38,41-Void; 9-Outboard blanket (18% SS, 9% H_2O, 60% Be, 13% Li_2O); 12,19-Shielding (20% SS, 80% H_2O); 15,26,28,42-Walls (100% SS); 16-Cryostat (4.43% SS, 95.57% Concrete*); 6,17,21,22-Shielding (80% SS, 20% H_2O); 20-Divertor (21% SS, 6% H_2O, 6% C); 23-Divertor (14% SS, 70% H_2O, 16% C); 29-Out-vessel zone (40% SS); 32,34-Shielding (100% SS); 35,37-Cryostat lid (20% SS, 80% H_2O); 39,40-Bellows (20% SS).

* Nuclear densities of epoxy ($C_{12}H_{20}O_3$) and concrete see in Table 2.1.

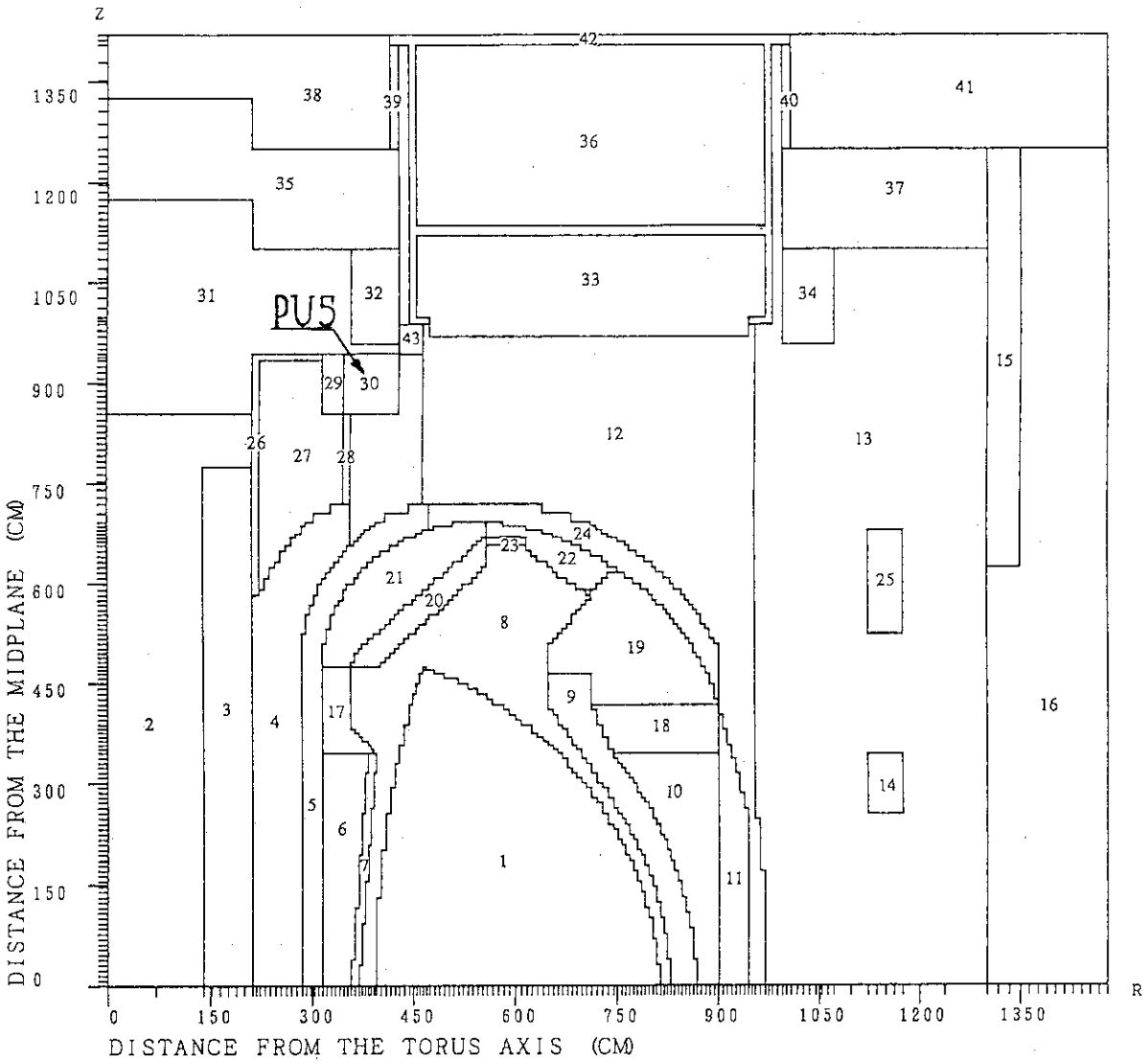

Fig. 2.5 R-Z calculational model (No.3) of ITER CDA.
1-Plasma (14-MeV neutron source); 2-Central solenoid (8% SS); 3,14,25, 30-PF coils (26% SS, 30% Cu, 17% He, 10% $C_{12}H_{20}O_3$*, 2.6% Nb); 4,5,11-Vacuum vessel (61% SS, 26% H_2O); 6,10,18-Shielding (50% SS, 50% H_2O); 7-Inboard shielding blanket (80% SS, 20% H_2O); 8,13,24,27,31,33,36,38, 41-Void; 9-Outboard shielding blanket (80% SS, 20% H_2O); 12,19-Shielding (20% SS, 80% H_2O); 15,26,28,42-Walls (100% SS); 16-Cryostat (4.43% SS, 95.57% Concrete*); 17,21,22-Shielding (80% SS, 20% H_2O); 20-Divertor (21% SS, 6% H_2O, 6% C); 23-Divertor (14% SS, 70% H_2O, 16% C); 29-Out-vessel zone (40% SS); 32,34-Shielding (100% SS); 35,37-Cryostat lid (20% SS, 80% H_2O); 39,40-Bellows (20% SS); 43-Shielding (100% SS).**

* Nuclear densities of epoxy ($C_{12}H_{20}O_3$) and concrete see in Table 2.1.

** Additional shield plug was employed to decrease the neutron/photon streaming between zones 30 and 12.

3. Discussion on the criterion of biological shield dose rate.

One of the main goals of this study is to obtain contour maps of biological dose rate after reactor shutdown. The biological shield system of ITER device has to ensure that both the personnel and the public are adequately protected according to the national regulations. It has also to allow personnel access to designated areas inside the reactor hall 24 hours after shutdown.

The 2.5 mrem/h biological dose limit 24 hours after shutdown was adopted as the reference criterion in the earlier phase of ITER CDA and Japanese fusion experimental reactor (FER) design. This value was based on the dose limitation of 50 mSv/y which was recommended by the International Commission on Radiological Protection (ICRP) in 1977 and adopted by Japanese regulations. However, during the ITER CDA more severe criterion, namely 0.5 mrem/h was adopted [1].

The revision was done in the new recommendations of the ICRP. According to these recommendations published in 1991 [26] the occupational dose limit was revised from the previous recommendations (50 mSv/y) to 20 mSv per year, averaged over defined period of 5 years with the further provision that the effective dose should not exceed 50 mSv in any single year.

The detailed discussion on the actual design criterion of the biological dose rate was not done so far. It must include zoning in a reactor hall considering the spatial dose rate and the working hours, and the designation of the controlled area and the supervised area, etc. The example of the dose rate design criteria and zoning in a reactor hall which were temporary adopted for FER are shown in Table 3.1 and Fig. 3.1, respectively.

Table 3.1 Dose Rate Design Criteria for FER zoning.

Zoning	Dose rate standard
A (No restriction)	< 0.00625 mSv/h
B (Working time < 40 h/week)	< 0.025 mSv/h
C (Working time < 10 h/week)	< 0.1 mSv/h
D (Very limited working time)	< 1 mSv/h
E (Usually no entry)	> 1 mSv/h

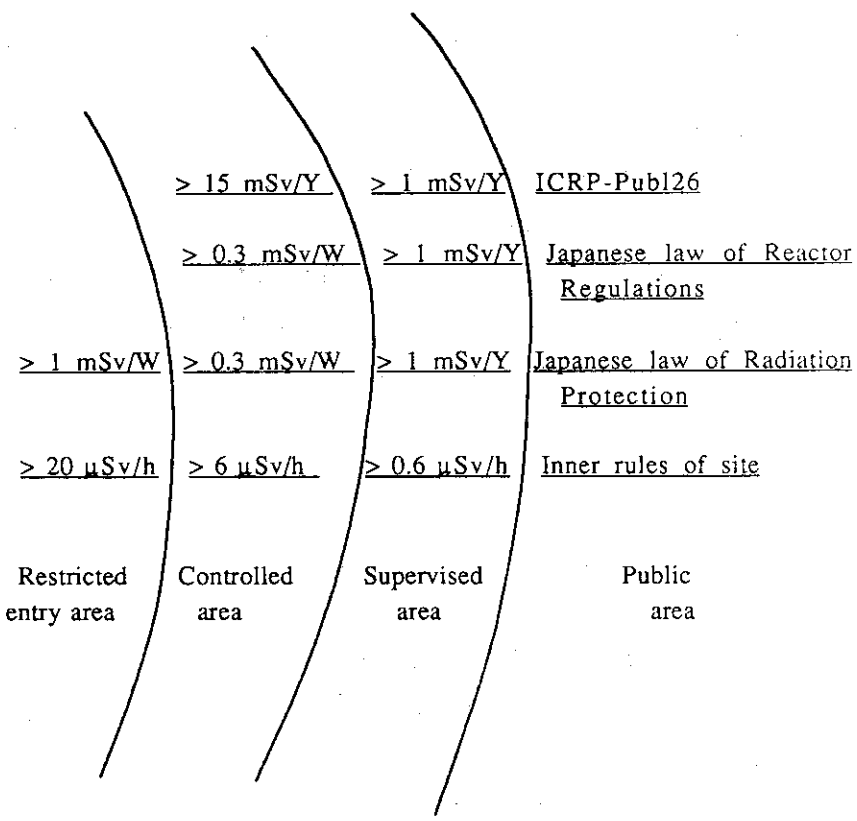

Fig. 3.1 The dose rate zoning of FER reactor.

4. Analysis of 14-MeV neutron flux contour maps during the reactor operation.

The 14-MeV flux contour maps were obtained for different calculational models with the aim to predict the biological dose rate distribution 24 hours after shutdown (Ref. 5 shows that the biological dose rate is to be proportional to the fast neutron flux). These neutron transport calculations being ran with only one energy group (15.00-13.72 MeV) are both "cheap" and "fast". Such an analysis being used to check number of design options is very effective and useful as a starting point for the next step detailed shutdown dose analysis.

4.1 Calculational model Nº 1.

Fig. 4.1 shows the results of 14-MeV neutron flux calculation. The 14-MeV flux at the first wall is the largest and is in the order of 10^{14} n·cm^2/s. The 14-MeV neutron flux on the inside and outside surfaces of cryostat is decreased in comparison with the flux at the first wall by 10^{10}-10^{14} and 10^{15}-10^{19} times, respectively. Thus, the radiation shielding in this case is expected to be rather effective in all zones of this calculational model. Therefore, only the fast flux (E>0.1 MeV) and total flux will be calculated for this model. The obtained results and discussion are shown in the chapter 5.

4.2 Calculational models Nº 2 and Nº 3.

The geometrical model Nº 2 is shown in Fig. 2.4. The results of 14-MeV neutron transport calculations for this calculational model (Figs. 2.4) are shown in Fig. 4.2. The neutron streaming from the plasma core through the zone Nº 31 is expected to be responsible for the increase of fast neutron flux and, correspondingly, shutdown

dose in the zone N°36. This neutron streaming is undesirable effect because, as it was mentioned above, personnel access 24 hours after shutdown is to be possible in the zone N° 36 for bellows maintenance.

The 14-MeV neutron flux behind the concrete cryostat at the toroidal midplane is smallest and is in the order of 10^1 n·cm^2/s. The 14-MeV neutron flux at the outside surface of the top cryostat lid is in the order of 10^3-10^0 n·cm^2/s depending on the distance from the shield plug. Thus, according to Ref. 5, the shutdown biological rate can be roughly estimated to be 10^{-1}-10^{-4} mrem/h, respectively.

The calculational results behind the maintenance shield plug (zone 12 in Figs. 2.4 and 2.5) are rather pessimistic. There is a large gradient of fast neutron flux at the top zone (zone N° 36 in Fig. 2.4 and 2.5) behind the maintenance shield plug. The 14-MeV neutron flux in the point A (see Fig. 2.4) of zone 36 ($\sim 10^5$ n·cm^2/s) is larger than the one in the point B ($\sim 10^3$ n·cm^2/s) by about 10^2 times. Thus, the biological dose in the point A can be in the order of 10 mrem/h without a safety factor. It means that initially proposed additional shields, marked in Fig. 2.4 as AS1 and AS2, are not effective enough and an additional shield is to be designed, such as the zone 43 in Fig. 2.5.

Number of neutron transport calculations of 14-MeV neutron flux distributions were carried out with different designs of an additional shield in zone 43 in Fig. 2.5. These calculations aimed to find a design of an additional shield which would decrease the neutron streaming in zone 31 in Fig. 2.4 and, correspondingly, decrease the 14-MeV neutron flux in the point A in Fig. 4.2 by 10^2-10^3 times.

Fig. 4.3 shows the calculational model N°2 with the additional shield AS3 of 70 cm thickness. The results of 14-MeV neutron transport calculations for above calculational model are shown in Fig. 4.4. The difference in 14-MeV neutron flux in the points A and B (Fig. 2.4) is decreased to 10. However, the absolute values of 14-MeV neutron fluxes are still rather large even with the 70 cm additional shield.

Therefore, the calculational model with both the additional shield AS1 and the additional shield AS3 was calculated. This model is shown in Fig. 4.5. The calculational results are shown in Fig. 4.6. The level of 14-MeV neutron flux in both the point A and point B is almost the same and less by 10^3 times than in Fig. 4.2.

However, it is rather complicated to design the additional shield AS3 between the PF coil PU5 (see Fig. 2.5) and the maintenance shield plug (zone 12 in Fig. 2.5). Thus, other model shown in Fig. 4.7 was calculated to check the possibility to place an additional shield AS3 between the additional shield AS1 and the maintenance shield plug. The results of neutron transport calculations are shown in Fig. 4.8. This case can not decrease the 14-MeV neutron flux in the zone 36 lower than the level in Fig. 4.6. However, the additional shields in Fig. 4.7 are both rather effective in comparison with the model Nº 2 shown in Fig. 2.4 and realistic from the design point of view. Thus this very model (Fig. 4.7) was taken as an alternative to reference ITER CDA model Nº 2 shown in Fig. 2.4. This alternative model has been named Nº 3 and shown in Fig. 2.5. The model Nº 3 will be discussed in the chapter 5.

Therefore, two calculational models were selected for calculations of neutron and gamma fluxes in all energy region, namely calculational models in Fig. 2.4 (model Nº2) and in Fig. 2.5 (model Nº 3). However, the above analysis for a 14-MeV neutron flux shows that the additional shield AS2 is not effective for both the model Nº2 and model Nº3. Therefore, all neutron transport calculations in full energy range in this study were carried out without the additional shield AS2 (zone 34 in both Fig. 2.4 and Fig. 2.5 was determined as a void).

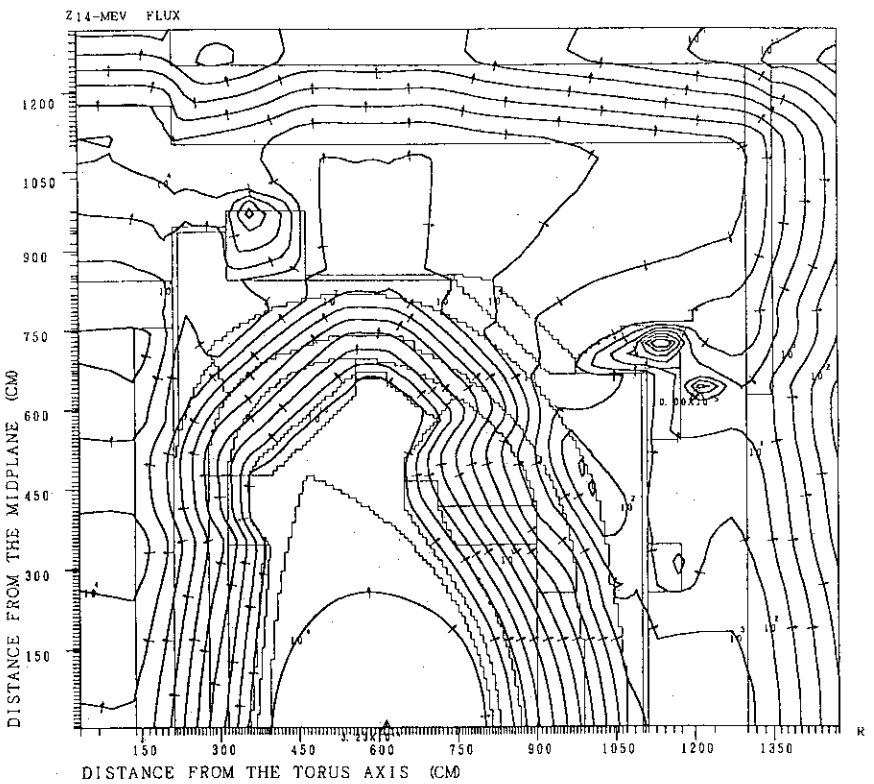

Fig. 4.1 14-MeV neutron flux distribution (model No.1) during the reactor operation (the contour lines represent values corresponding to 1×10^{n} $n/cm^{2} \cdot s$. The arrows show the direction of the downward gradient of the 14-MeV neutron flux).

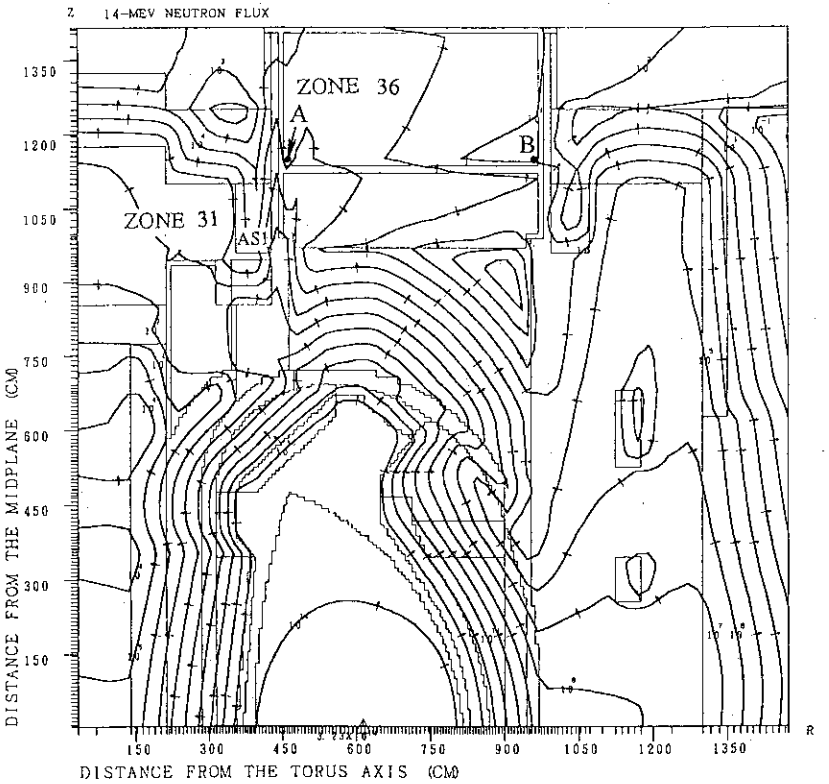

Fig. 4.2 14-MeV neutron flux distribution (model No.2 is shown in Fig.2.4) during the reactor operation (the contour lines represent values corresponding to 1×10^{n} $n/cm^{2} \cdot s$. The arrows show the direction of the downward gradient of the 14-MeV neutron flux).

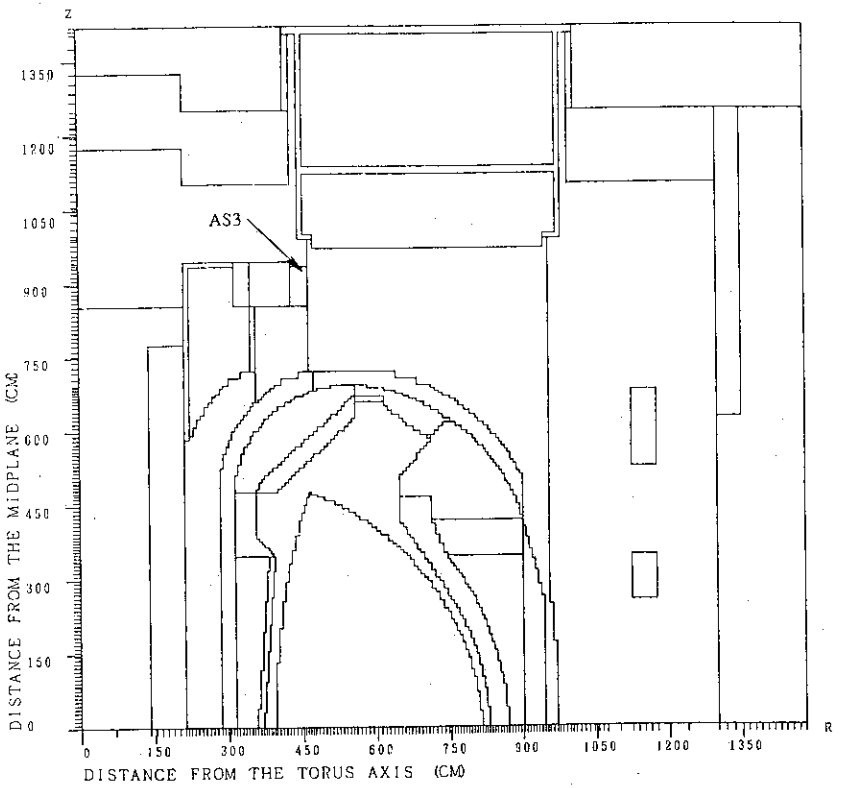

Fig. 4.3 R-Z calculational model (No.2) of ITER CDA with the additional shield AS3 of 70 cm thickness.

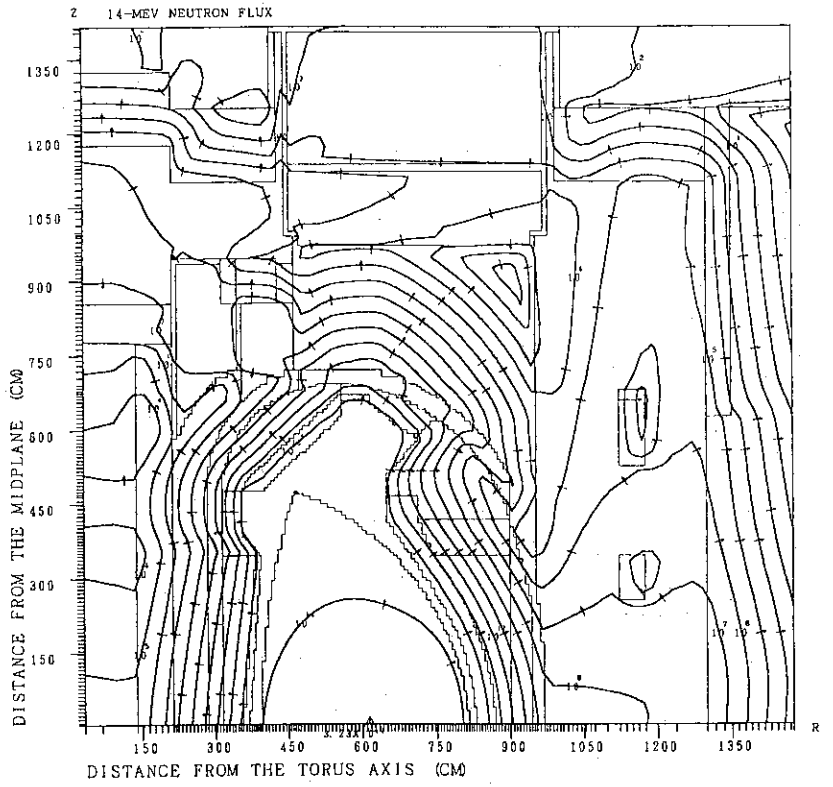

Fig. 4.4 14-MeV neutron flux distribution (modified model No.2 is shown in Fig.4.3 during the reactor operation (the contour lines represent values corresponding to 1×10^{n} n/cm^{2}·s. The arrows show the direction of the downward gradient of the 14-MeV neutron flux).

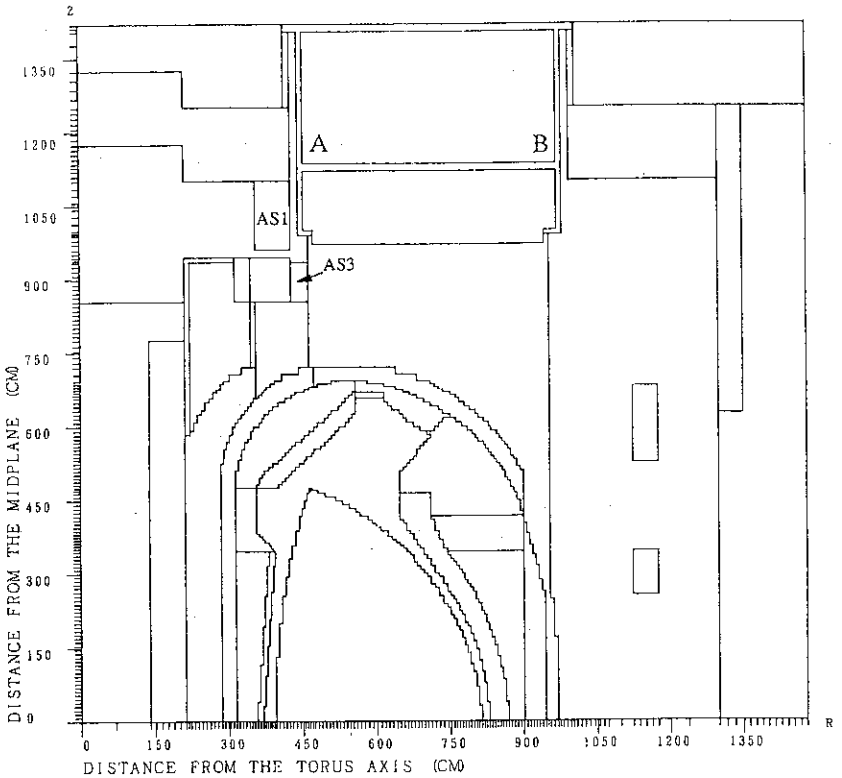

Fig. 4.5 R-Z calculational model (No.2) of ITER CDA with both the additional shield AS1 and AS3.

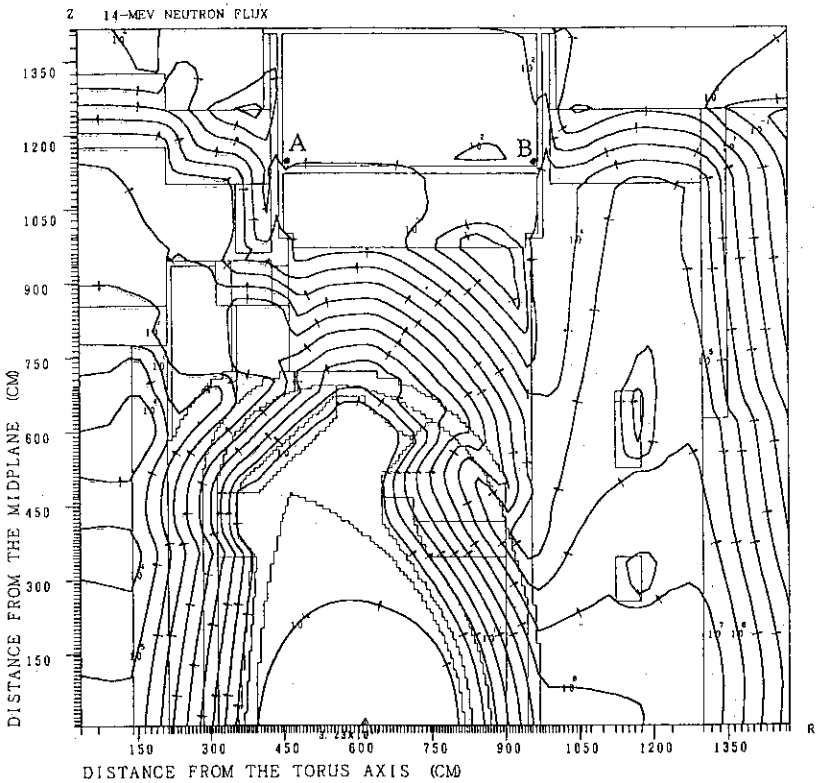

Fig. 4.6 14-MeV neutron flux distribution (modified model No.2 is shown in Fig.4.5) during the reactor operation (the contour lines represent values corresponding to 1×10^{n} $n/cm^{2}\cdot s$. The arrows show the direction of the downward gradient of the 14-MeV neutron flux).

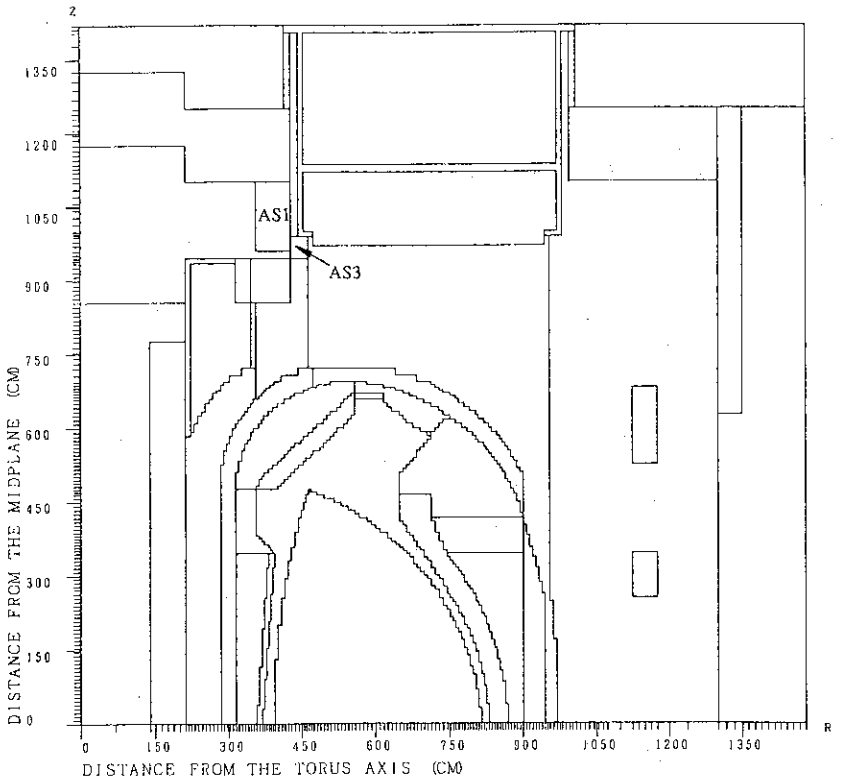

Fig. 4.7 R-Z calculational model (No.2) of ITER CDA with both the additional shield AS1 and AS3.

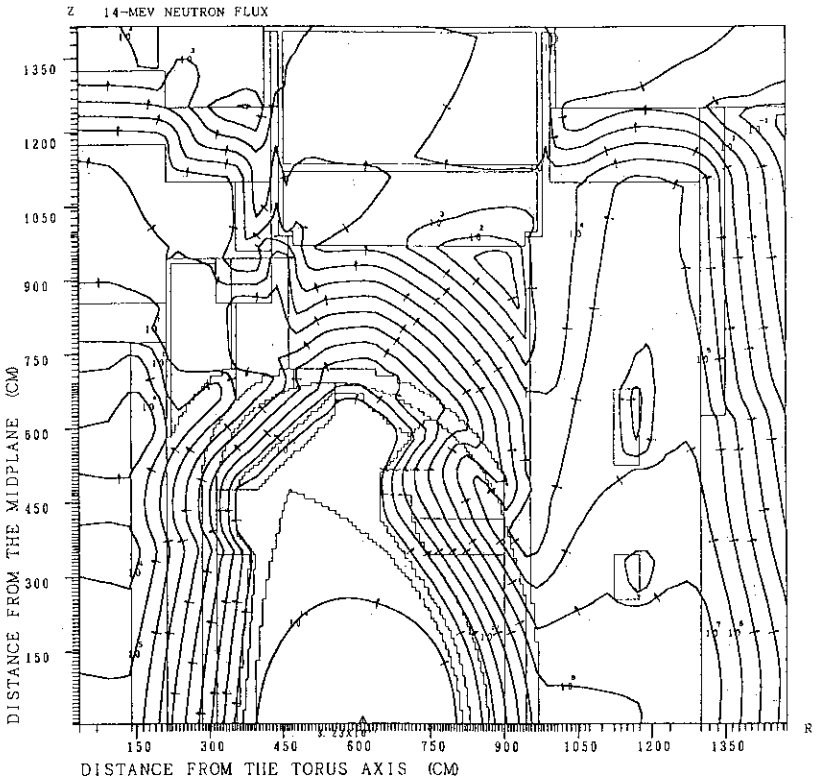

Fig. 4.8 14-MeV neutron flux distribution (modified model No.2 is shown in Fig.4.7) during the reactor operation (the contour lines represent values corresponding to 1×10^{n} $n/cm^{2}\cdot s$. The arrows show the direction of the downward gradient of the 14-MeV neutron flux).

5. Analysis of fast, total neutron flux and gamma-ray flux contour maps during the reactor operation.

5.1 Calculational model Nº 1.

The results of fast neutron flux (E>0.1 MeV), total neutron flux and total gamma-ray flux calculations for calculational model Nº 1 are shown in Figs. 5.1-5.3, respectively. Neutron fluxes at the toroidal midplane of calculational model Nº 1 at some important for shielding analyses positions are shown in Table 5.1.

The one-dimensional distributions of fast neutron flux, total neutron flux and total gamma-ray flux for the four most important cuts shown in Fig. 5.4 were obtained as well. These results are shown in Figs. 5.5-5.8. One-dimensional distributions of 14-MeV neutron flux are shown in above figures as well.

The fast neutron flux behind the outside surface of vacuum vessel is less than the flux at the first wall by 7-8 orders of magnitude. The smallest decrease takes place in the top zone where the bulk shield thickness is less than that for the toroidal midplane.

The fast neutron flux in the reactor core is decreased by 13-16 orders of magnitude behind the concrete cryostat. The smallest decrease takes place in the top cryostat zone where the cryostat thickness is less than that in the toroidal midplane. In the toroidal midplane the fast neutron flux in the reactor core was decreased by 16 orders of magnitude behind the concrete cryostat. The same behavior was found for the total neutron flux and total gamma flux.

Ten orders decrease in the fast neutron flux is supposed to be necessary to decrease the shutdown dose below the limit [5]. However, as it was shown above, the fast neutron flux in the reactor core is decreased by at least 13 orders of magnitude behind the concrete cryostat for the investigated calculational model Nº1. Thus, this calculational model is expected to be overshielded from the biological shield point of view. Therefore, the shutdown dose calculations are not necessary for this calculational model.

5.2 Calculational models Nº 2 and Nº 3 .

The results of 14-MeV neutron flux, fast neutron flux, total neutron flux and total gamma flux calculations for calculational model Nº 2 are shown in Figs. 5.9, 5.10, 5.11 and 5.12, respectively. The dpa number in the stainless steel is shown in Fig. 5.13 as well. Neutron fluxes at the toroidal midplane of calculational model Nº 2 at some important for shielding analyses positions are shown in Table 5.2.

The one-dimensional 14-MeV, fast and total neutron fluxes and total gamma-ray flux for the four most important cuts shown in Fig. 5.14 were obtained for the calculational model Nº 2 as well as in the paragraph 5.1 for the calculational model Nº 1. Obtained results are shown in Figs. 5.15-5.18.

All considered fluxes at the first wall are the largest (as in considered above calculational model Nº 1). The fast neutron flux, for example, at the first wall is in the order of 10^{14} n·cm^2/s.

The fast neutron flux behind the concrete cryostat is changing by about six orders of magnitude depending on the place at the outside cryostat surface where it has been taken. Such a large changing is explained by numerous inhomogeneities in both the reactor bulk shielding and the cryostat. The smallest decrease of fast neutron flux takes place in the top cryostat zone behind the maintenance shield plug. Two void cavities (zone 31 in Fig. 2.4) are responsible for relatively high values of fast neutron flux in above-mentioned zone. On contrary, in the toroidal midplane the fast neutron flux in the reactor core was decreased by about 12 orders of magnitude behind the concrete cryostat.

The 14-MeV neutron flux, fast neutron flux, total neutron flux and gamma-ray fluxes for the calculational model Nº 3 are shown in Figs. 5.19-5.22, respectively.

The fast neutron flux in the top cryostat zone behind the maintenance shield plug is in the order of 10^3 n·cm^2/s, in comparison with the 10^5 n·cm^2/s for the model Nº 2. Therefore, it is expected that the radiation shield of calculational model Nº 3 will be effective enough to decrease the shutdown dose below the limit.

Table 5.1 Neutron and photon fluxes ($1/cm^2 \cdot s$) at the toroidal midplane of calculational model No.1.
(Assumed Fusion Power : 1000 MW)

Neutron flux Place	Radius, cm	14-MeV neutron flux	Fast neutron flux	Total neutron flux	Total photon flux
Inboard first wall	366	4.40+13*	1.78+14	2.53+14	1.1+14
Outboard first wall	833	4.98+13	1.95+14	2.76+14	1.2+14
Behind inboard vacuum vessel	275.5	6.72+9	2.11+11	5.49+11	5.0+11
Behind outboard vacuum vessel	994	1.85+7	9.33+8	2.25+9	1.2+9
Behind inboard blanket	354	1.23+13	9.14+13	1.68+14	4.5+13
Behind outboard blanket	872.2	1.39+12	1.56+13	3.74+13	4.0+13
Before concrete cryostat	1308.3	9.12+2	4.46+5	4.80+6	2.2+6
Behind concrete cryostat	1473.5	5.37-2	7.51+0	8.44+2	3.8+3

* Read as 4.40×10^{13}

Table 5.2 Neutron and photon fluxes ($1/cm^2 \cdot s$) at the toroidal midplane of calculational model No.2.
(Assumed Fusion Power : 1000 MW)

Neutron flux Place	Radius, cm	14-MeV neutron flux	Fast neutron flux	Total neutron flux	Total photon flux
Inboard first wall	366	7.0+13*	2.0+14	2.8+14	1.4+14
Outboard first wall	833	9.0+13	2.4+14	3.8+14	1.6+14
Behind inboard vacuum vessel	275.5	5.2+8	1.3+10	2.2+10	2.8+10
Behind outboard vacuum vessel	994	2.0+6	2.8+7	7.0+7	5.2+8
Behind inboard blanket	354	9.0+12	3.5+13	8.0+13	2.5+13
Behind outboard blanket	872.2	6.2+11	1.15+13	2.4+13	1.1+13
Before concrete cryostat	1308.3	3.0+5	6.5+6	1.9+7	1.1+8
Behind concrete cryostat	1473.5	2.1-2	3.0+1	2.0+2	1.2+3

* Read as 7.0×10^{13}

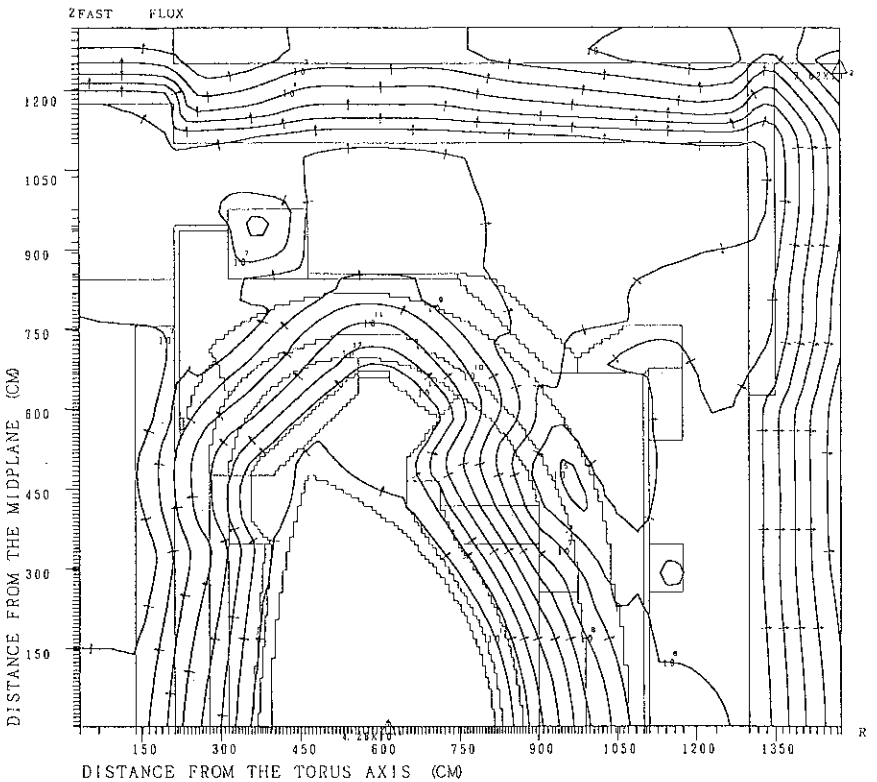

Fig. 5.1 Fast neutron flux distribution (model No.1) during the reactor operation (the contour lines represent values corresponding to $1x10^n$ $n/cm^2 \cdot s$. The arrows show the direction of the downward gradient of the fast neutron flux).

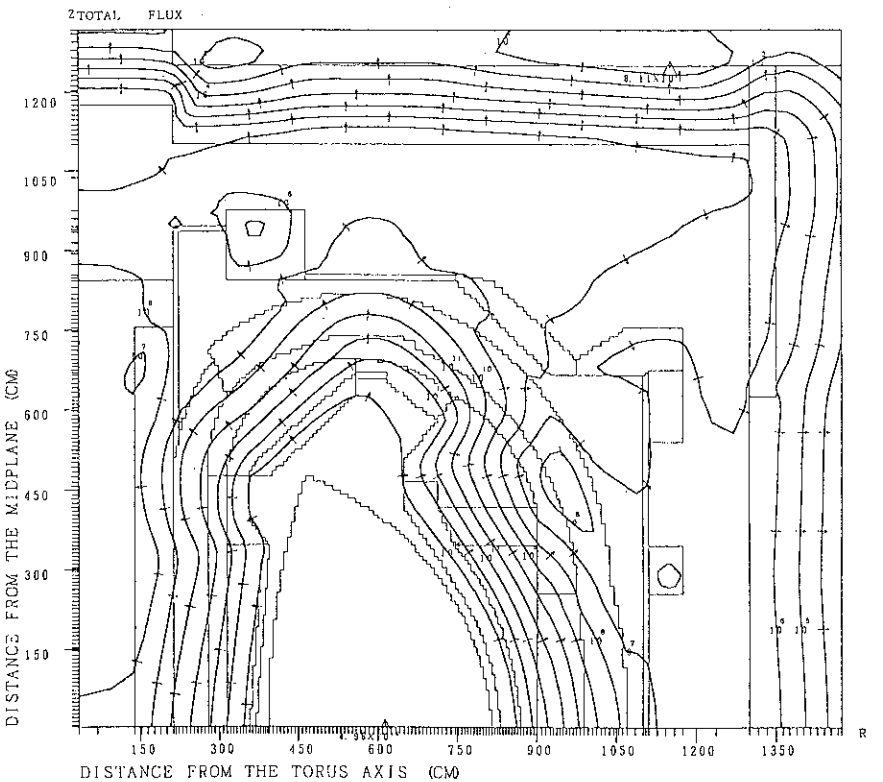

Fig. 5.2 Total neutron flux distribution (model No.1) during the reactor operation (the contour lines represent values corresponding to $1x10^n$ $n/cm^2 \cdot s$. The arrows show the direction of the downward gradient of the total neutron flux).

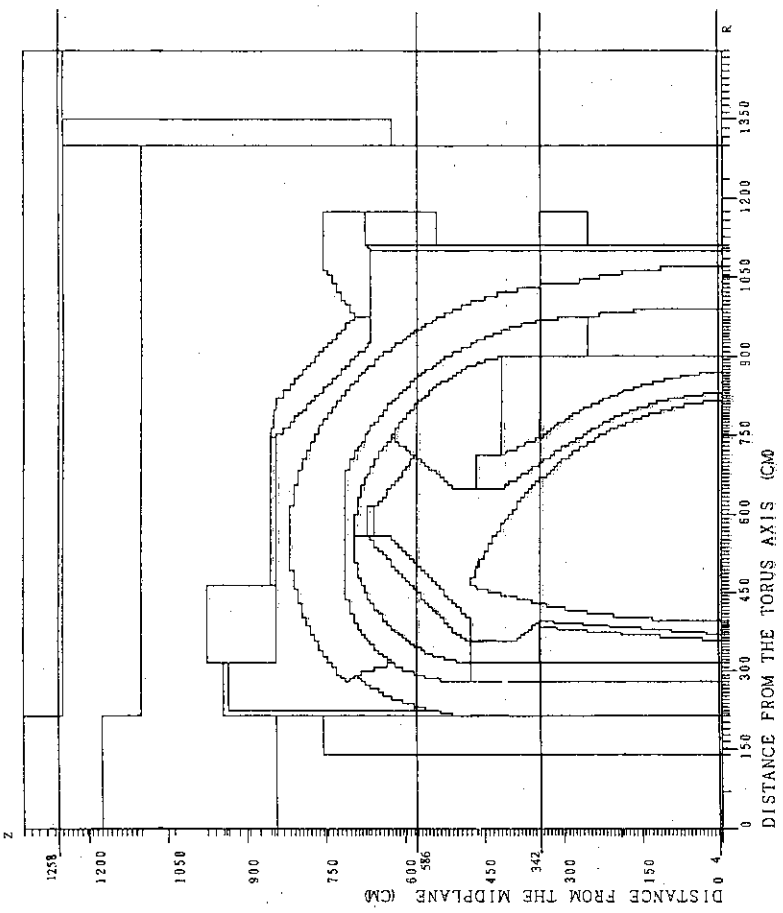

Fig. 5.4 R-Z calculational model (No.1) of ITER CDA with the shown four cuts (Z=4 cm, Z=342 cm, Z=586 cm and Z=1258 cm) in toroidal direction.

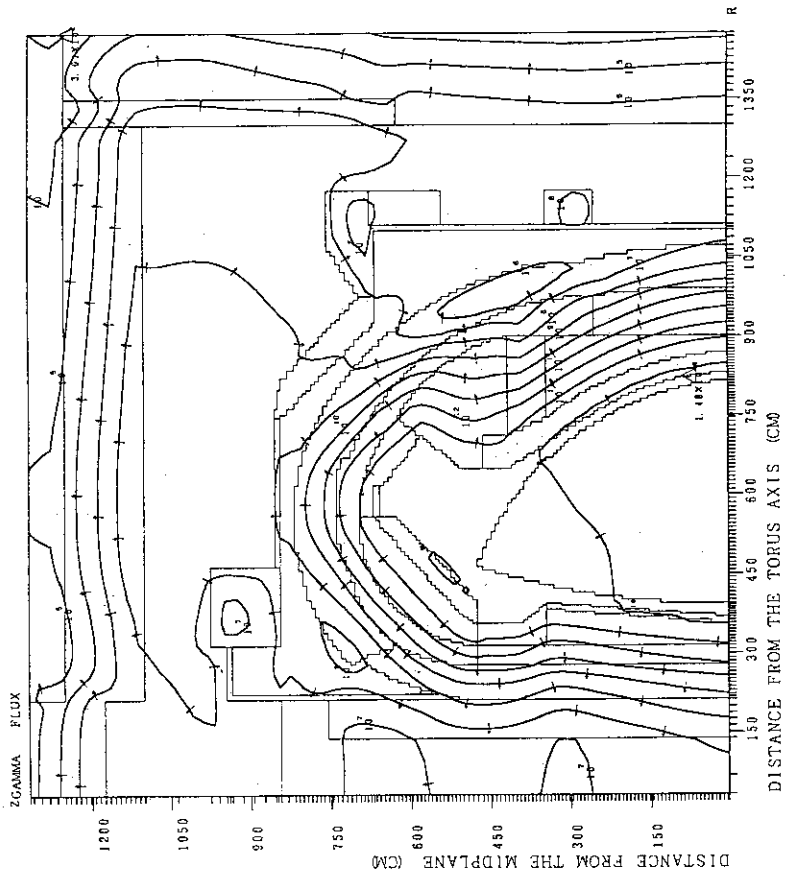

Fig. 5.3 Total gamma-ray flux distribution (model No.1) during the reactor operation (the contour lines represent values corresponding to 1×10^{n} n/cm^{2}·s. The arrows show the direction of the downward gradient of the total gamma-ray flux).

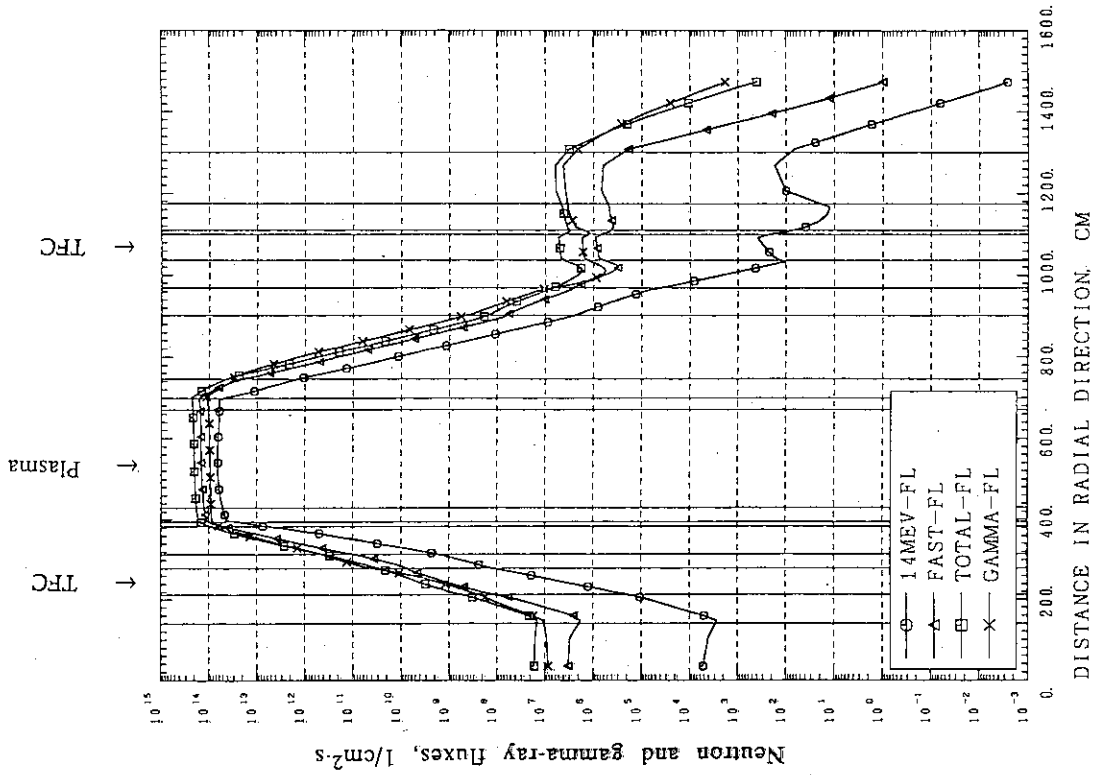

Fig. 5.6 Neutron and gamma-ray fluxes (the cut with coordinate Z=342 cm in Fig.5.4) versus the distance in radial direction.

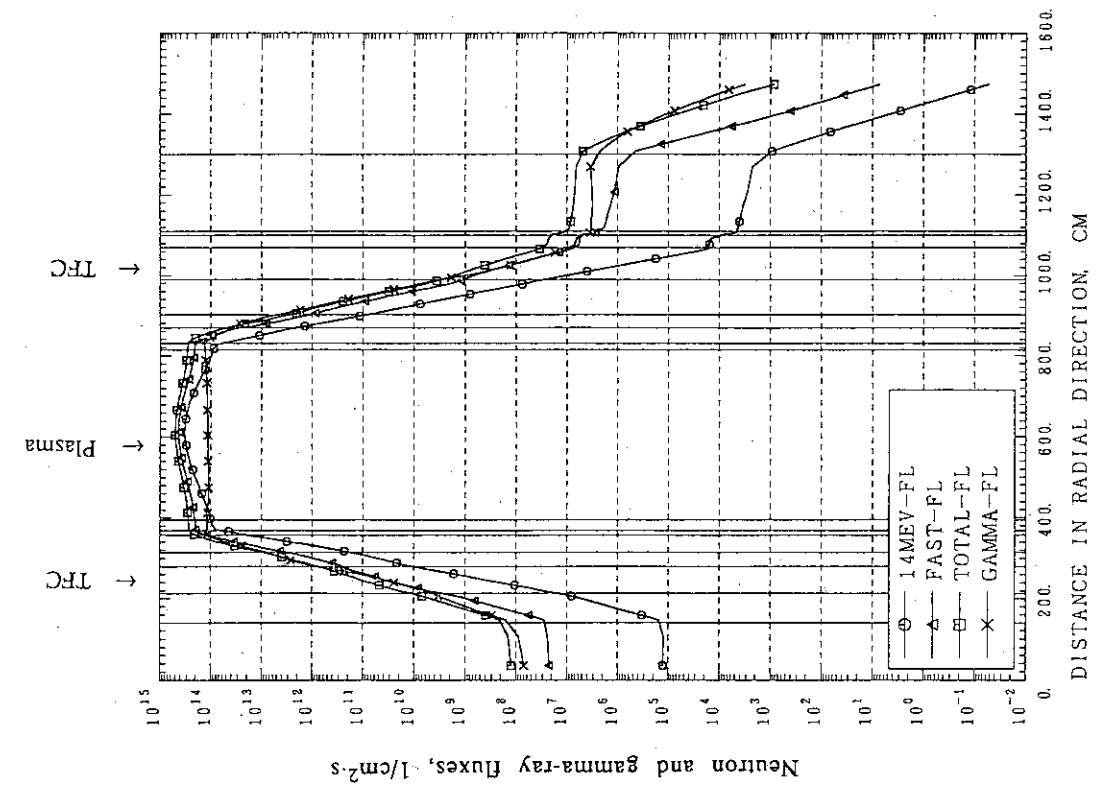

Fig. 5.5 Neutron and gamma-ray fluxes (the cut with coordinate Z=4 cm in Fig.5.4) versus the distance in radial direction.

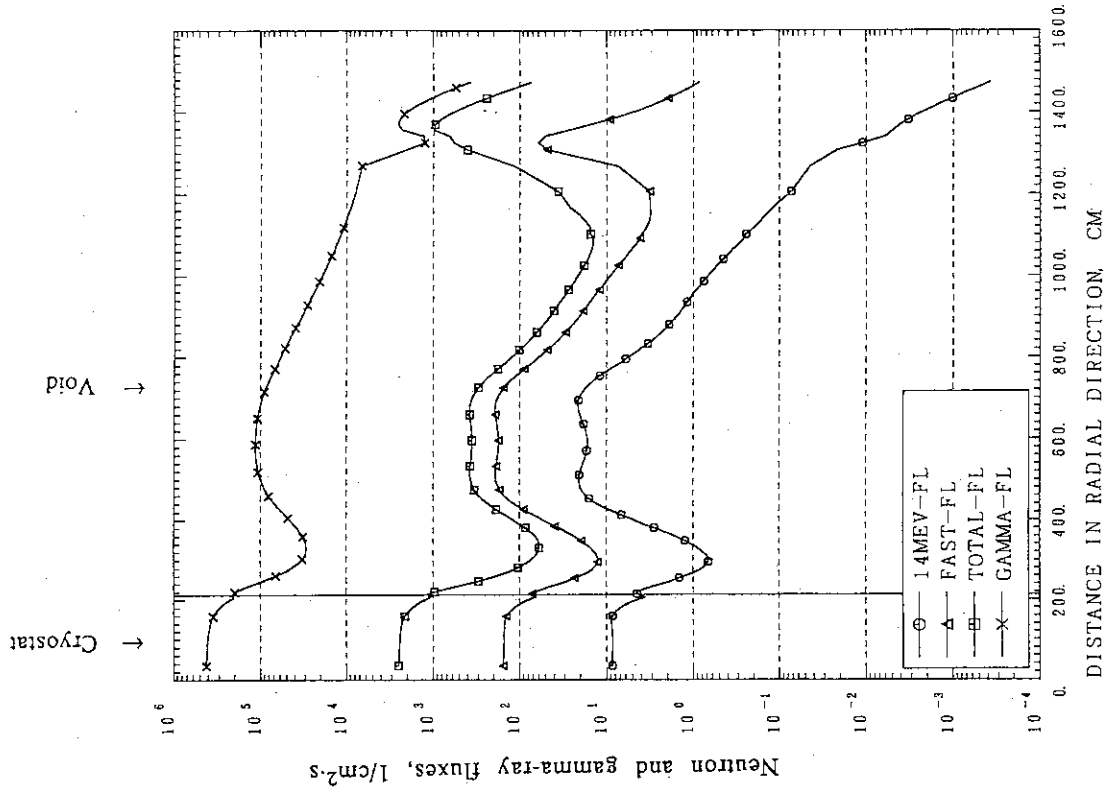

Fig. 5.8 Neutron and gamma-ray fluxes (the cut with coordinate Z=1258 cm in Fig.5.4) versus the distance in radial direction.

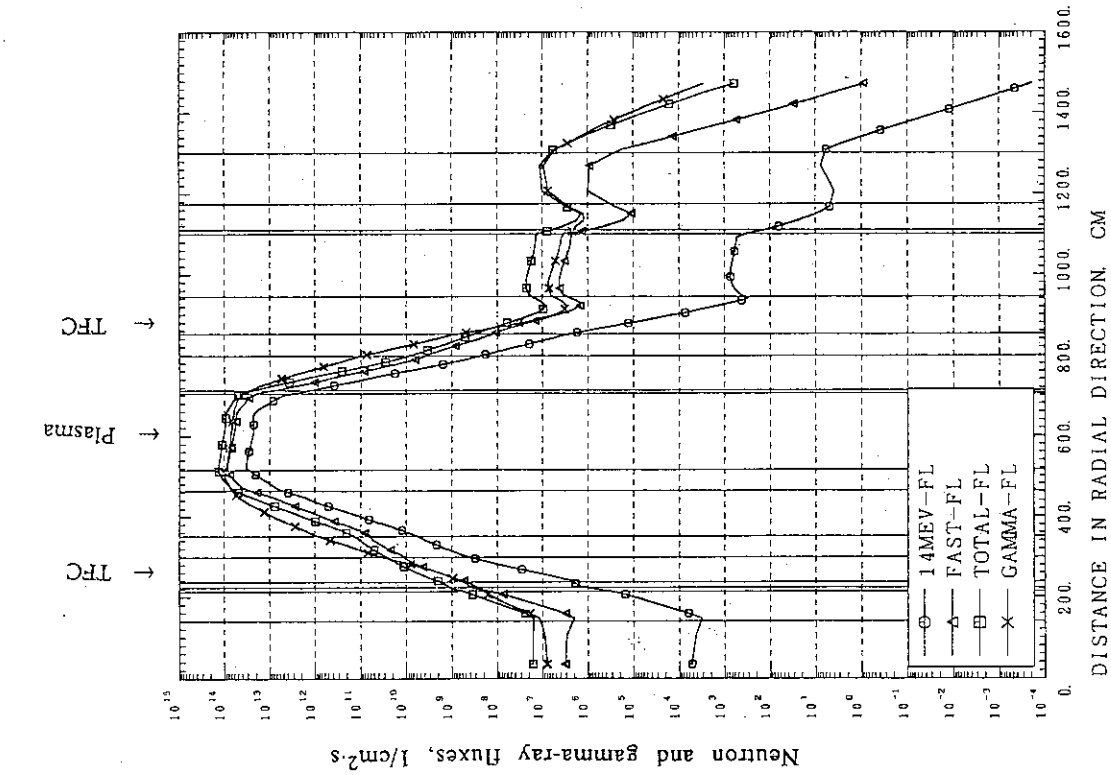

Fig. 5.7 Neutron and gamma-ray fluxes (the cut with coordinate Z=586 cm in Fig.5.4) versus the distance in radial direction.

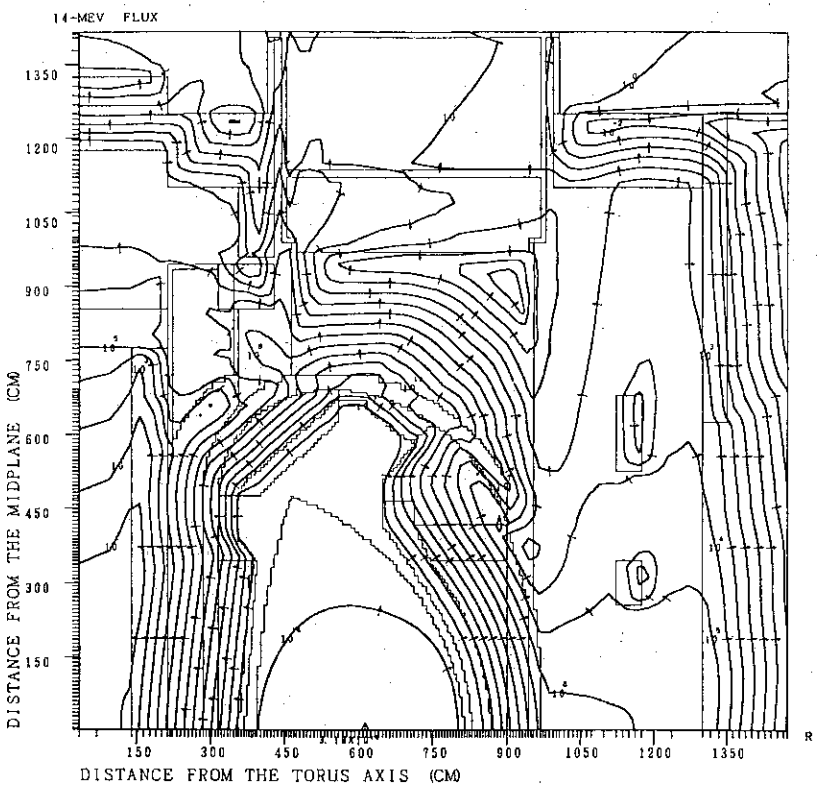

Fig. 5.9 14-MeV neutron flux distribution (model No.2) during the reactor operation (the contour lines represent values corresponding to 1×10^{n} n/cm^{2}·s. The arrows show the direction of the downward gradient of the 14-MeV neutron flux).

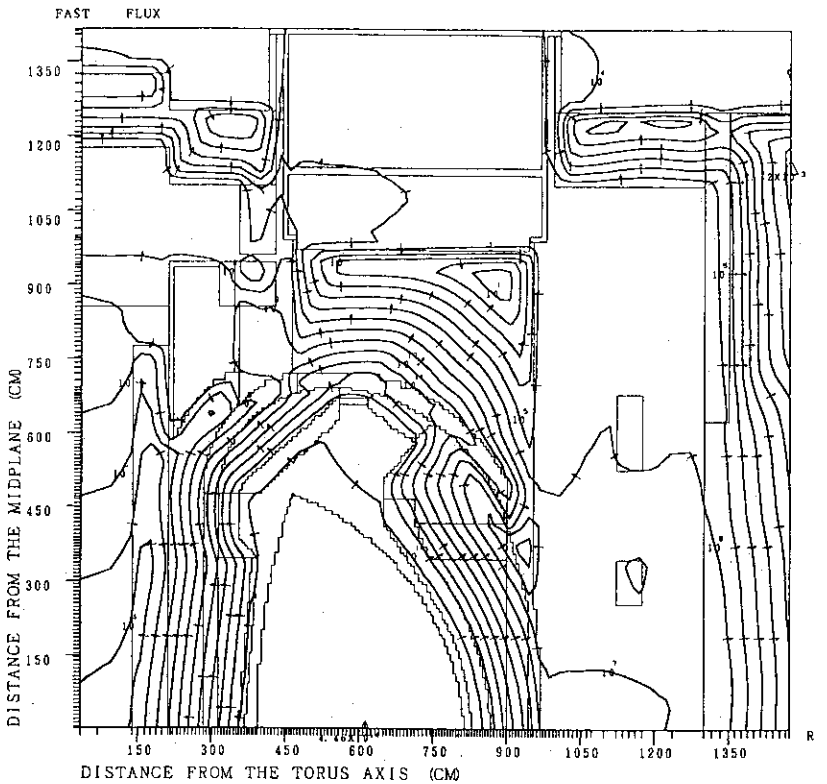

Fig. 5.10 Fast neutron flux distribution (model No.2) during the reactor operation (the contour lines represent values corresponding to 1×10^{n} n/cm^{2}·s. The arrows show the direction of the downward gradient of the fast neutron flux).

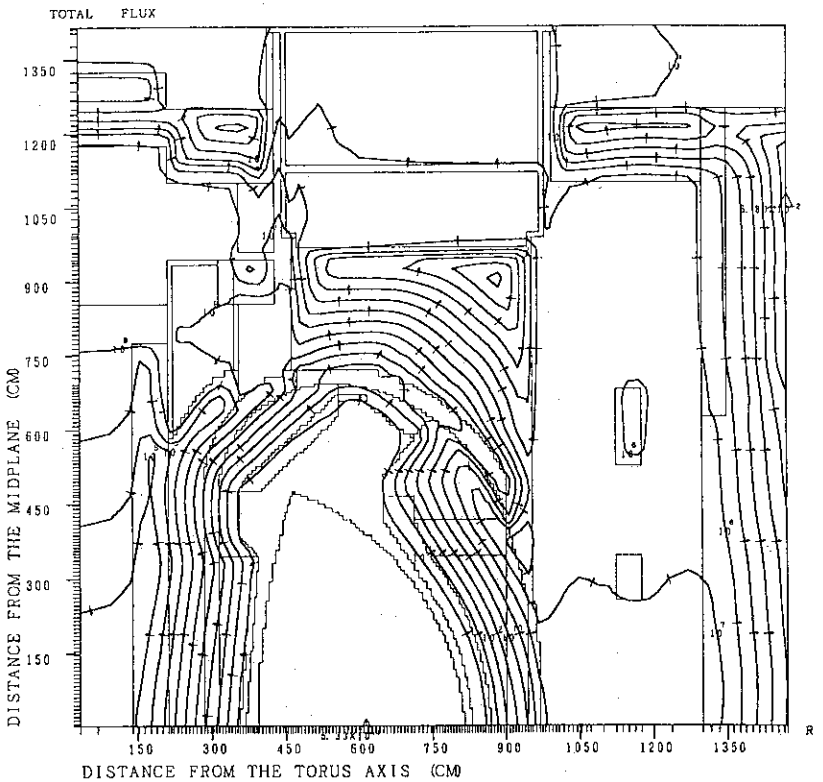

Fig. 5.11 Total neutron flux distribution (model No.2) during the reactor operation (the contour lines represent values corresponding to 1×10^{n} n/cm^{2}·s. The arrows show the direction of the downward gradient of the total neutron flux).

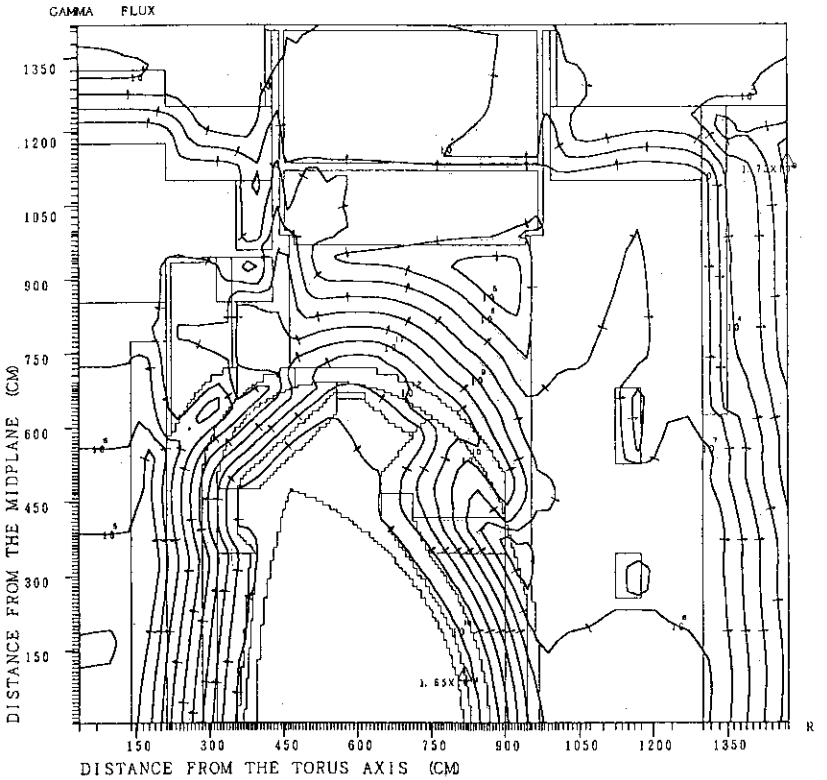

Fig. 5.12 Total gamma-ray flux distribution (model No.2) during the reactor operation (the contour lines represent values corresponding to 1×10^{n} n/cm^{2}·s. The arrows show the direction of the downward gradient of the total gamma-ray flux).

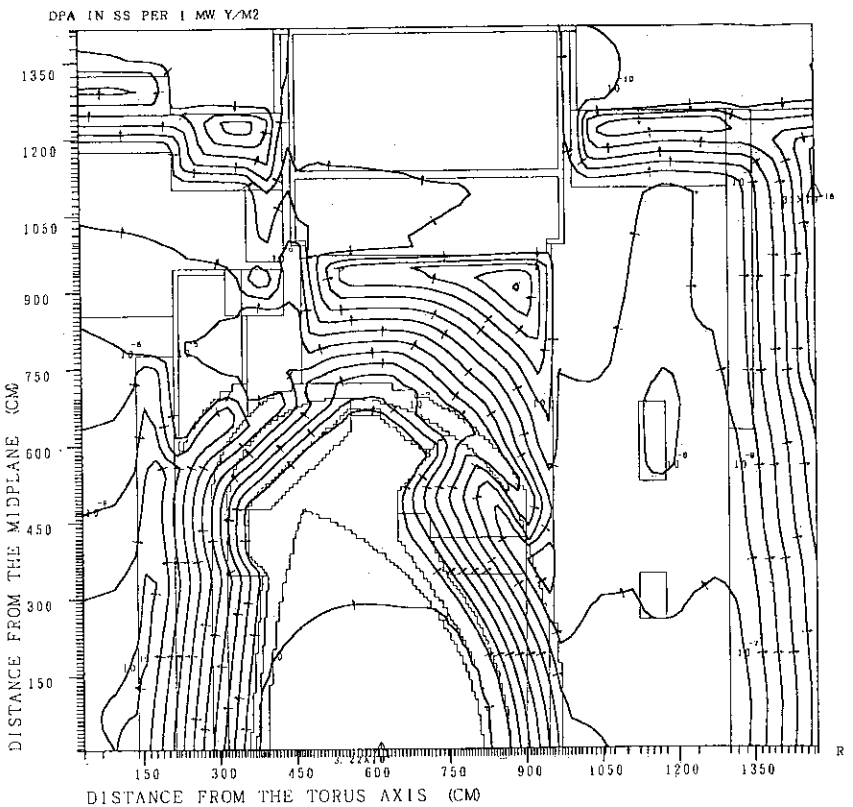

Fig. 5.13 Displacement damage in the stainless steel after 1 MW·y/m^2 reactor operation (the contour lines represent values corresponding to 1x10^n n/cm^2·s. The arrows show the direction of the downward gradient of the dpa number).

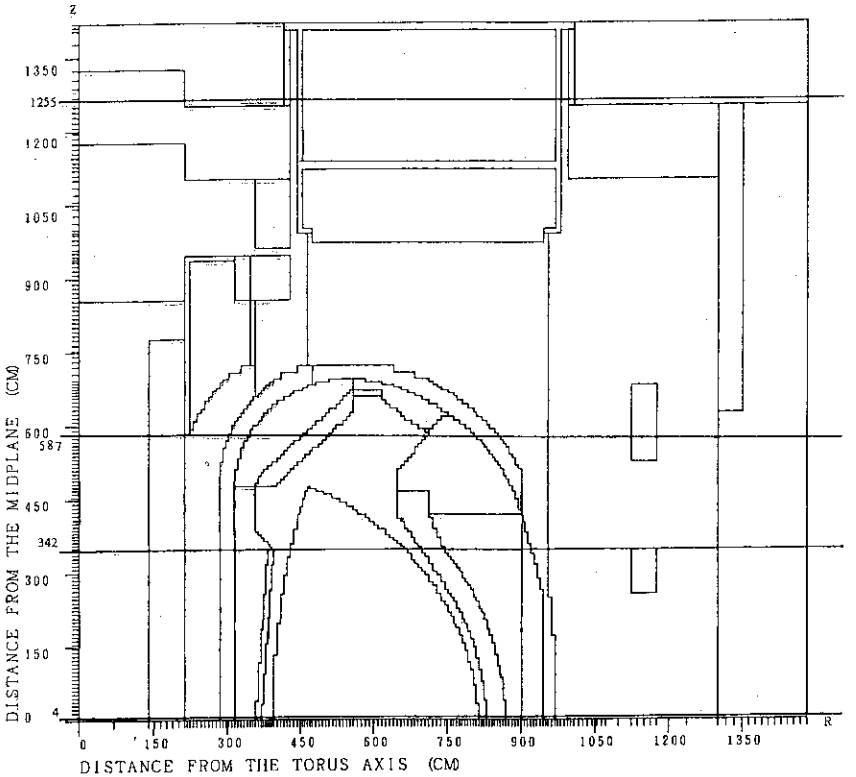

Fig. 5.14 R-Z calculational model (No.2) of ITER CDA with the shown four cuts (Z=4 cm, Z=342 cm, Z=587 cm and Z=1255 cm) in toroidal direction.

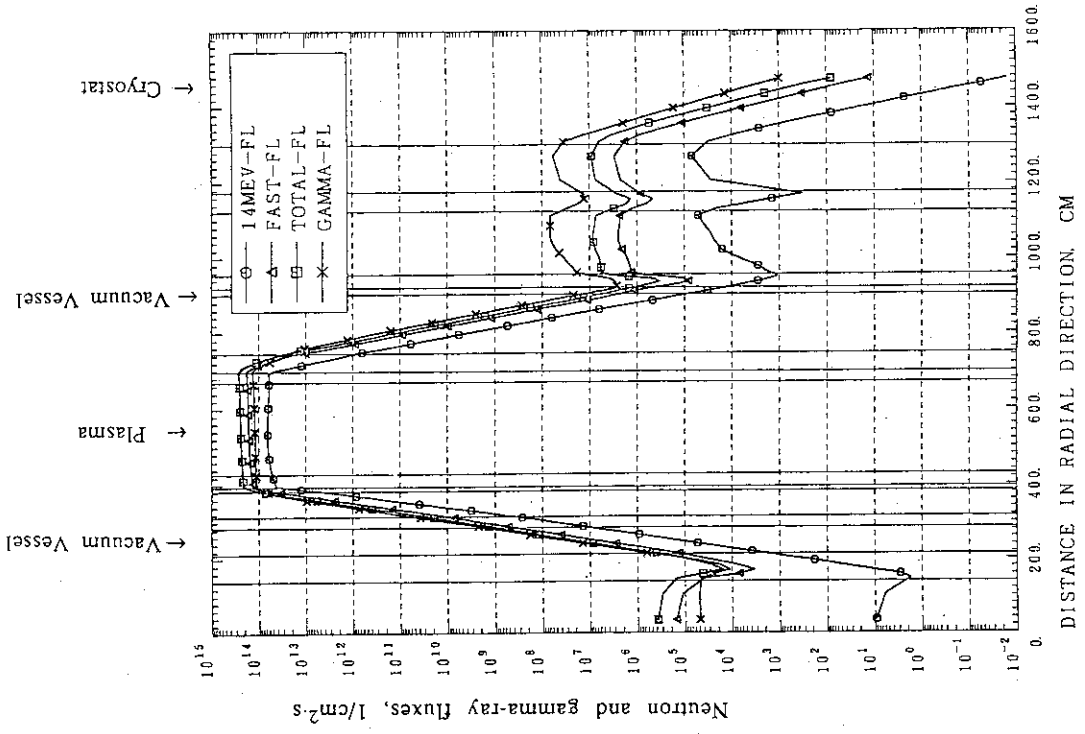

Fig. 5.16 Neutron and gamma-ray fluxes (the cut with coordinate Z=342 cm in Fig.5.14) versus the distance in radial direction.

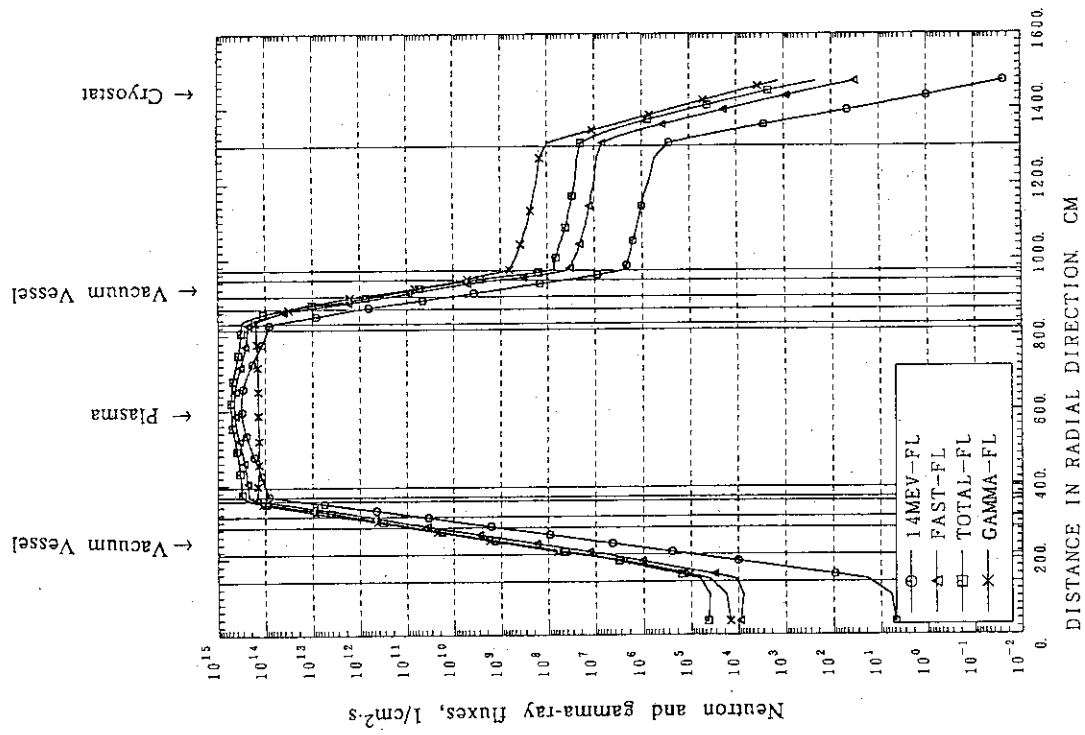

Fig. 5.15 Neutron and gamma-ray fluxes (the cut with coordinate Z=4 cm in Fig.5.14) versus the distance in radial direction.

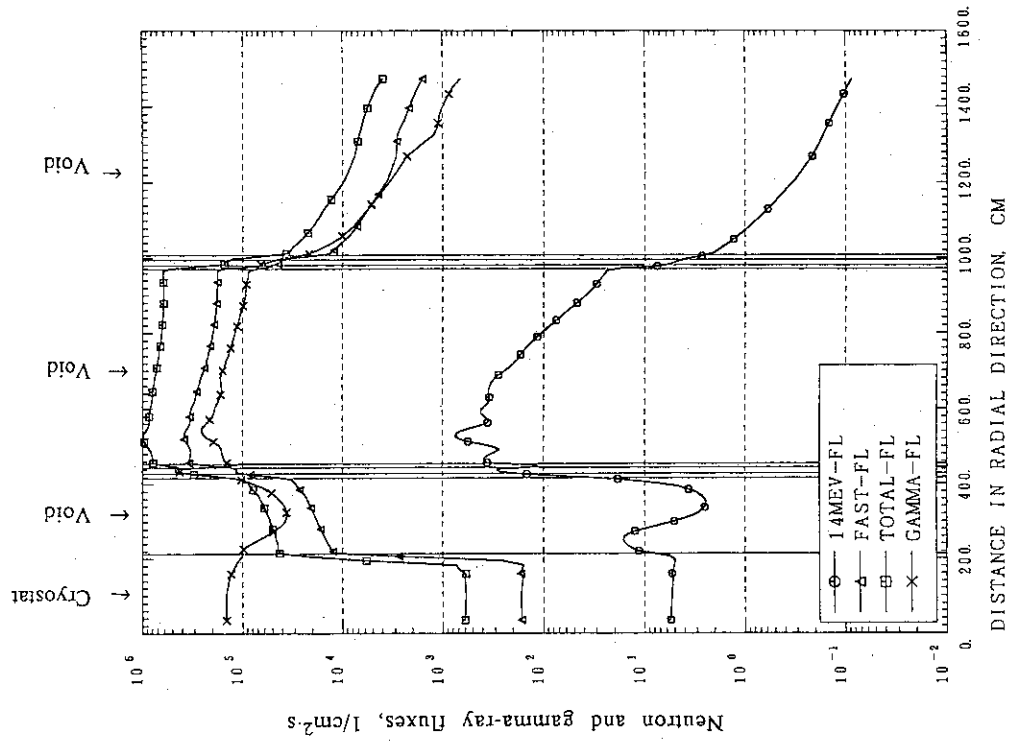

Fig. 5.18 Neutron and gamma-ray fluxes (the cut with coordinate Z=1255 cm in Fig.5.14) versus the distance in radial direction.

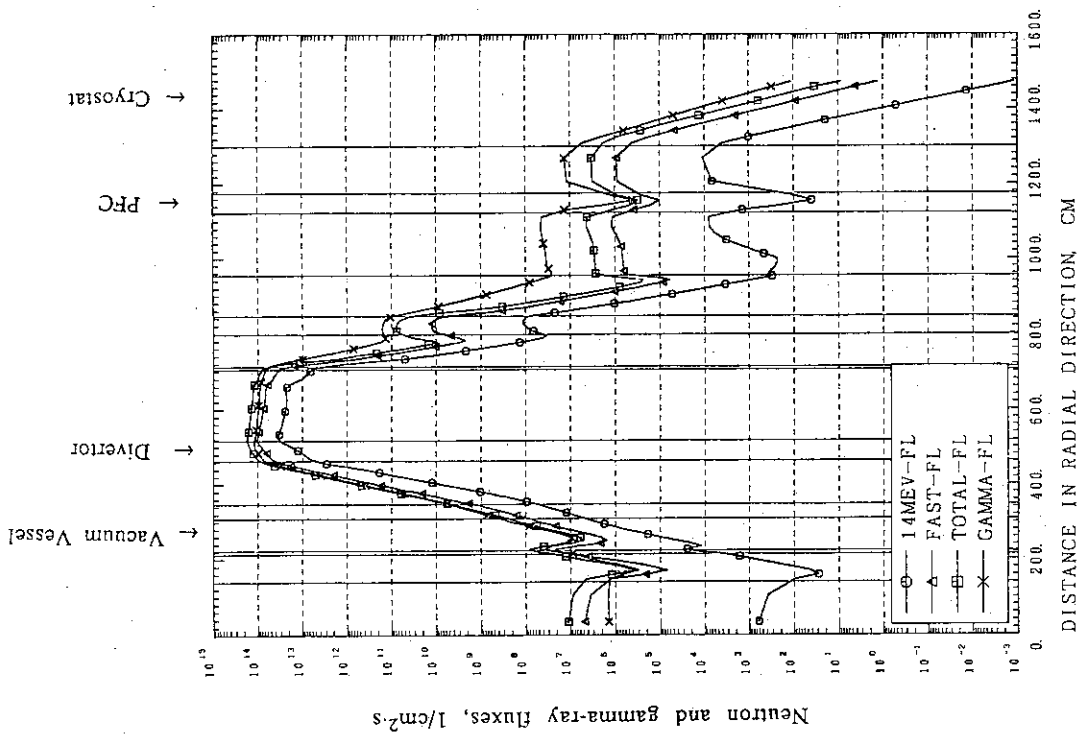

Fig. 5.17 Neutron and gamma-ray fluxes (the cut with coordinate Z=587 cm in Fig.5.14) versus the distance in radial direction.

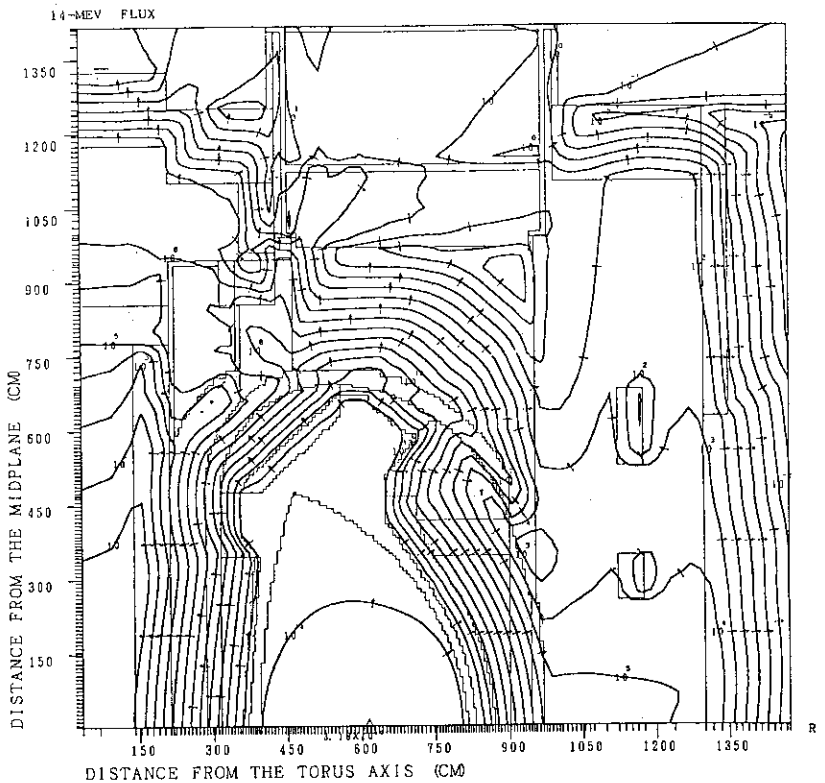

Fig. 5.19 14-MeV neutron flux distribution (model No.3) during the reactor operation (the contour lines represent values corresponding to 1×10^{n} n/cm^{2}·s. The arrows show the direction of the downward gradient of the 14-MeV neutron flux).

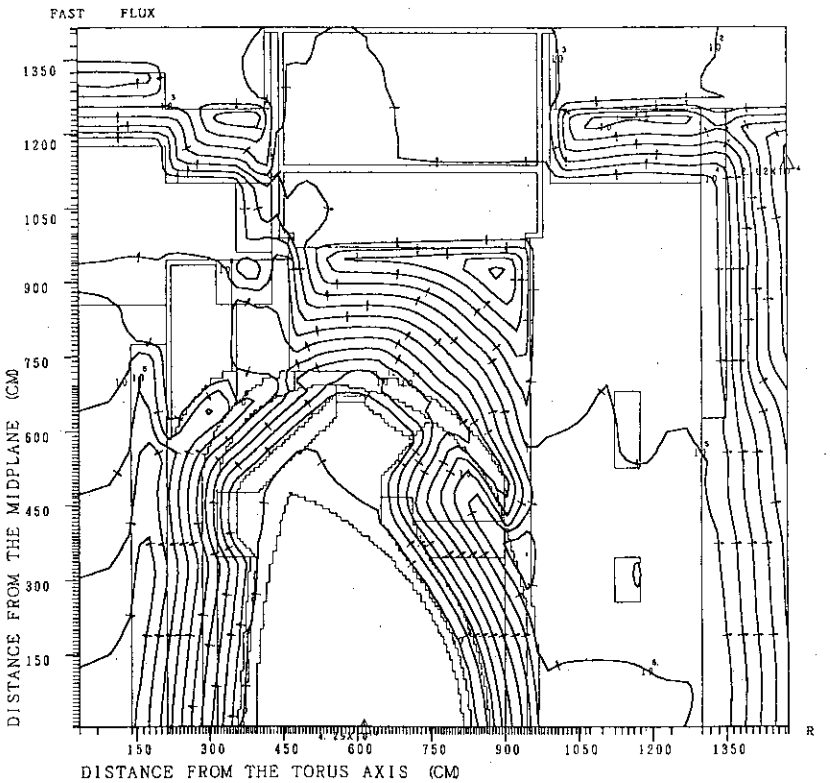

Fig. 5.20 Fast neutron flux distribution (model No.3) during the reactor operation (the contour lines represent values corresponding to 1×10^{n} n/cm^{2}·s. The arrows show the direction of the downward gradient of the fast neutron flux).

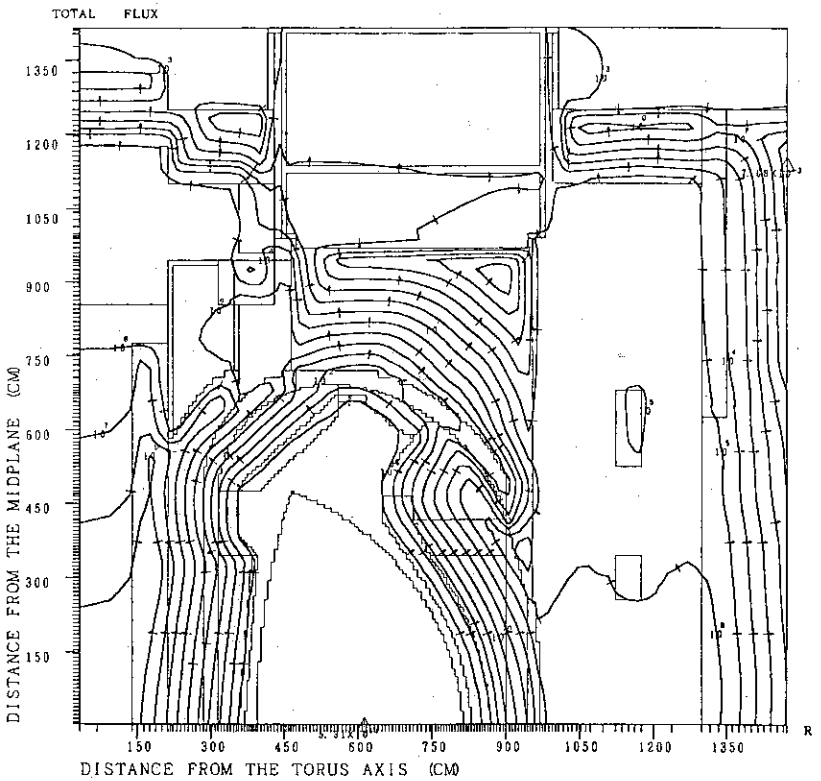

Fig. 5.21 Total neutron flux distribution (model NO.3) during the reactor operation (the contour lines represent values corresponding to 1×10^{n} n/cm^{2}·s. The arrows show the direction of the downward gradient of the total neutron flux).

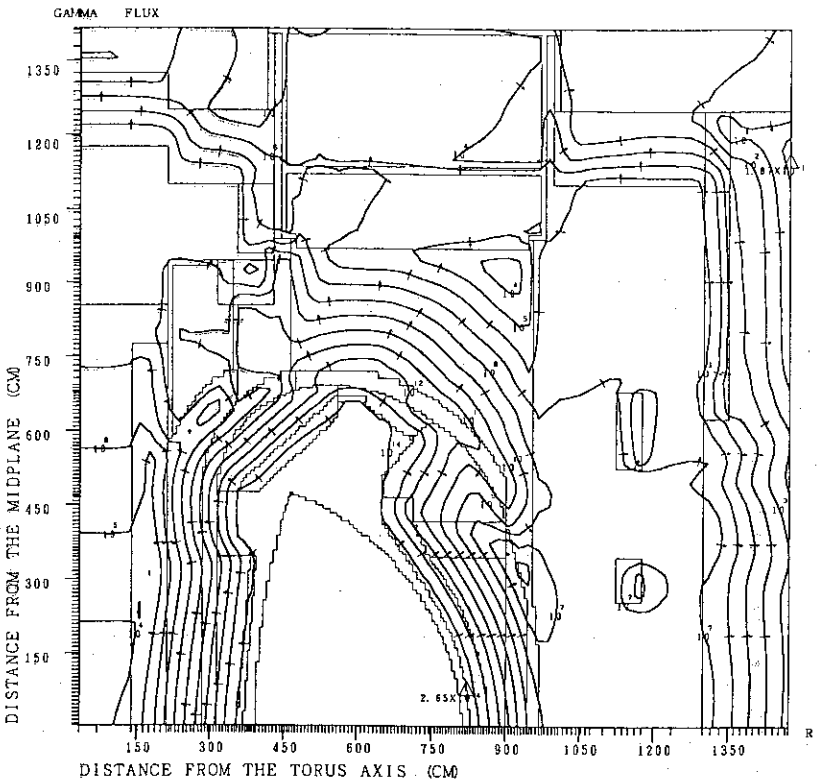

Fig. 5.22 Total gamma-ray flux distribution (model No.3) during the reactor operation (the contour lines represent values corresponding to 1×10^{n} n/cm^{2}·s. The arrows show the direction of the downward gradient of the total gamma-ray flux).

6. Calculations of nuclear heating distribution in in-vessel and out-vessel components of ITER device.

Total nuclear heating distribution was calculated for calculational model N°1. This calculational model was discussed above and shown in Fig. 2.3. The one-dimensional distributions of nuclear heating rate in the stainless steel and water were obtained for the three most important cuts shown in Fig. 5.4, namely Z=4, 342 and 586 cm. Correspondent results are shown in Figs. 6.1-6.6. The one-dimensional distributions of nuclear heating rate in the beryllium and Li_2O were obtained for the two most important cuts shown in Fig. 5.4, namely Z=4 and 342 cm. Correspondent results are shown in Figs. 6.7-6.10. To be consistent with the Refs. 13 and 14 the Li_2O was enriched by 50% of ^6Li.

The results of total nuclear heating calculations for in-vessel and out-vessel zones of ITER device shown in Fig. 2.3 are shown in Table 6.1.

The total nuclear heating in the toroidal field (TF) coils (zones 13 and 27 in Fig. 2.3) seems to be overestimated by about four-five times (about 210 kW without safety factors) in comparison with the 50-70 kW (safety factors are included) obtained during ITER CDA [3]. It could be explained as follows :

1) homogeneous blanket/shield zones are not optimal from the shielding point of view;

2) the B_4C/Pb layer employed behind an inboard semi-permanent shield during ITER CDA [3] was not included in the calculational model in Fig. 2.3;

Other quantities in Table 6.1 are expected to be rather reasonable. This statement was confirmed by a comparison of obtained above results with rough estimations made during ITER CDA [27]. These results are shown in Table 6.2.

The nuclear heating in both inboard and outboard in-vessel components obtained in this study is very close to the results obtained in Ref. 27. However, the nuclear heating in the divertor was calculated to be about 60% larger than that in Ref. 27, namely 77 MW and 48 MW, respectively.

The difference in nuclear heating in divertor can be easily explained by the fact that the rib structure behind the divertor plates was not taken into account in rough estimations of total nuclear heating in the divertor zone in Ref. 27.

Table 6.1 Total nuclear heating distribution in in-vessel and out-vessel components of ITER device (calculational model No.1). (Assumed Fusion Power : 1000 MW)

ITER component	zone number	Total nuclear heating		
		neutron	gamma	total
Inboard blanket	4	60.2 MW	21.3 MW	81.5 MW
Inboard shield	6	29.1 MW	71.6 MW	101 MW
	7	3.34 MW	25.1 MW	28.4 MW
	28	13.9 MW	38.2 MW	52.1 MW
Divertor	3	15.0 MW	52.3 MW	67.3 MW
	26	4.86 MW	5.28 MW	10.1 MW
Outboard blanket	5	412 MW	172 MW	584 MW
Outboard shield	8	9.27 MW	60.5 MW	69.8 MW
	9	9.82 MW	30.1 MW	39.9 MW
	10	1.36 MW	8.68 MW	10.0 MW
	11	14.7 MW	76.4 MW	91.1 MW
Vacuum vessel	12	176 kW	2.27 MW	2.45 MW
	25	462 kW	5.42 MW	5.88 MW
	30	150 kW	2.66 MW	2.81 MW
TF coils	13	5.86 kW	137 kW	142 kW
	27	2.18 kW	70.0 kW	72.2 kW
Cryostat	22	0.47 W	35.3 W	35.8 W
	23	1.29 W	256 W	257 W
	24	32.1 W	1.07 kW	1.10 kW

Table 6.2 Total nuclear heating in in-vessel ITER components.
(Assumed Fusion Power : 1000 MW)

ITER component		Present study	ITER CDA (Ref. 27*)
INBOARD	FW/Blanket (zones@ 4, 6)	183 MW	192 MW
	Shield (zones 7, 28 and 1/3 heat of zone 8)	~ 104 MW	~ 119 MW
	Total	~ 287 MW	~ 311 MW
OUTBOARD	Total (zones 5, 9-11 and 2/3 heat of zone 8)	772 MW	728 MW
DIVERTOR	(zones 3, 26)	77 MW	48 MW
VACUUM VESSEL	(zones 12, 25 and 30)	11 MW	19 MW
TOTAL IN VESSEL		1147 MW	1107 MW

*- Results of this report were renormalized to 1000 MW Fusion Power for comparison.

@- See Fig. 2.3.

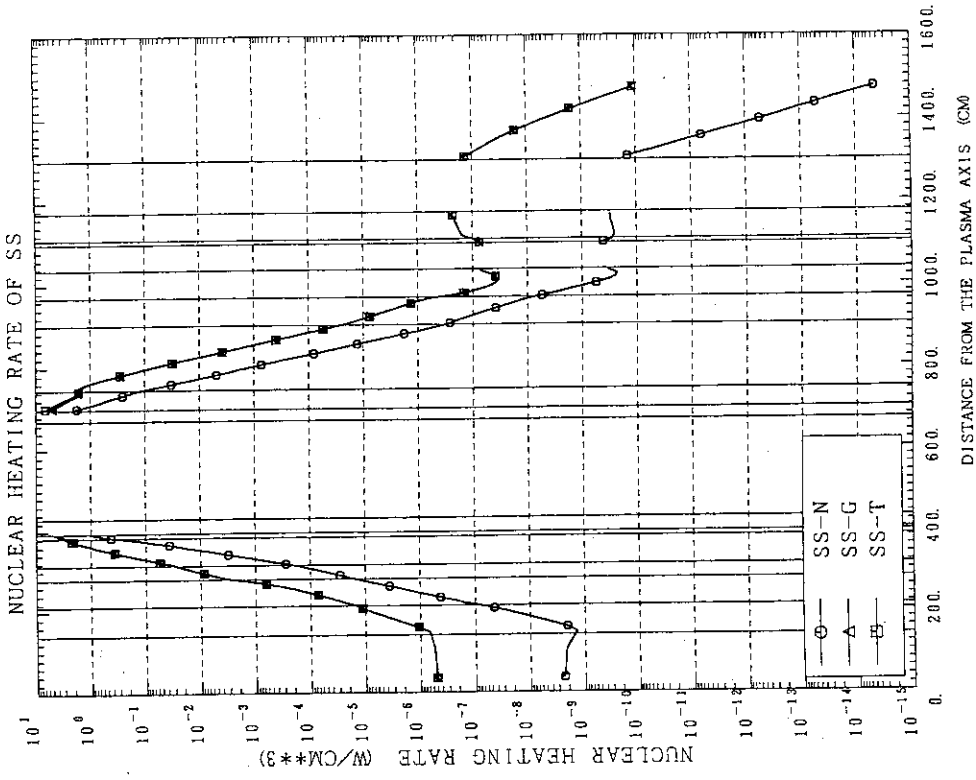

Fig. 6.2 Nuclear heating rate of SS (the cut with coordinate Z=342 cm in Fig.5.4) versus the distance in radial direction.

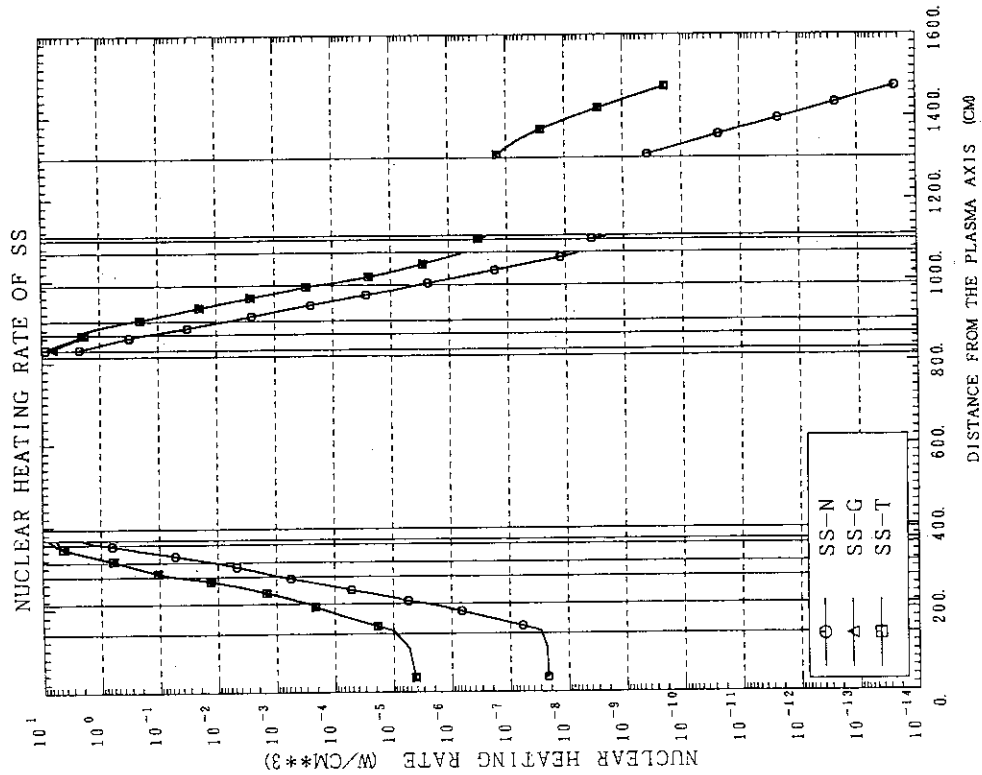

Fig. 6.1 Nuclear heating rate of SS (the cut with coordinate Z=4 cm in Fig.5.4) versus the distance in radial direction.

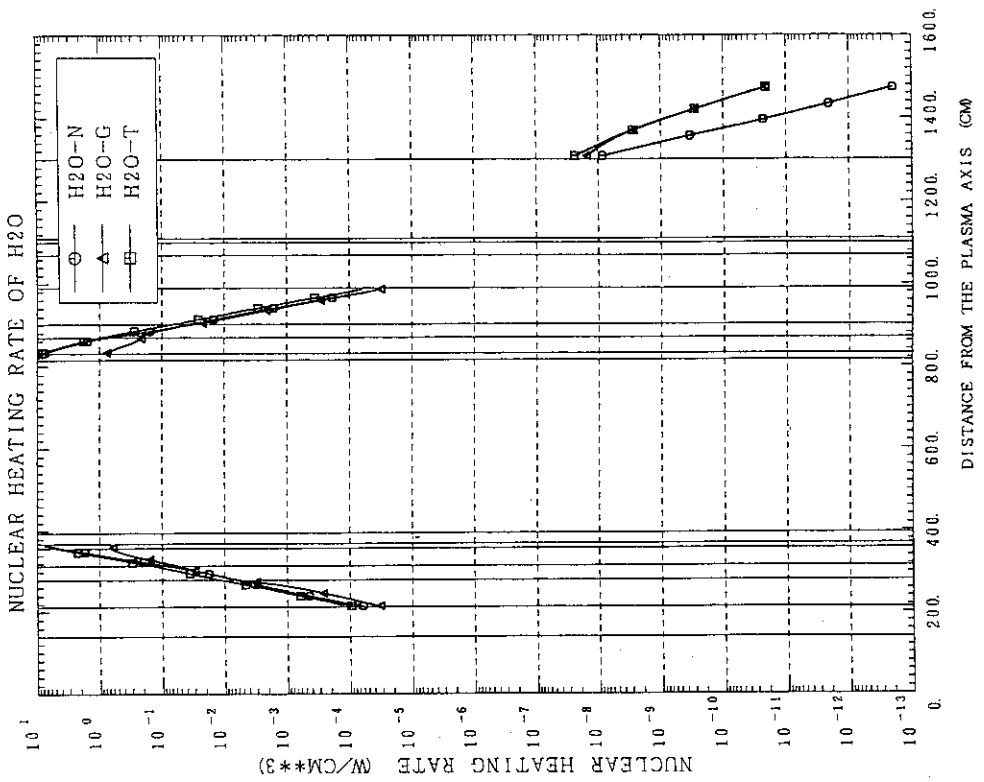

Fig. 6.4 Nuclear heating rate of H_2O (the cut with coordinate Z=4 cm in Fig.5.4) versus the distance in redial direction.

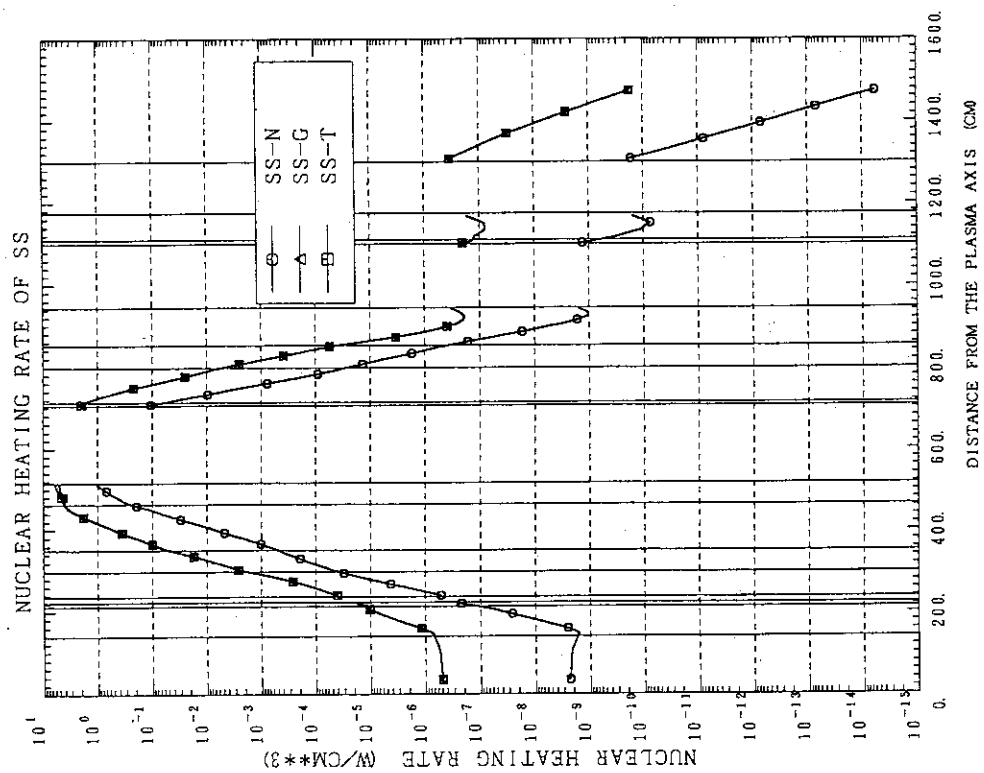

Fig. 6.3 Nuclear heating rate of SS (the cut with coordinate Z=586 cm in Fig.5.4) versus the distance in radial direction.

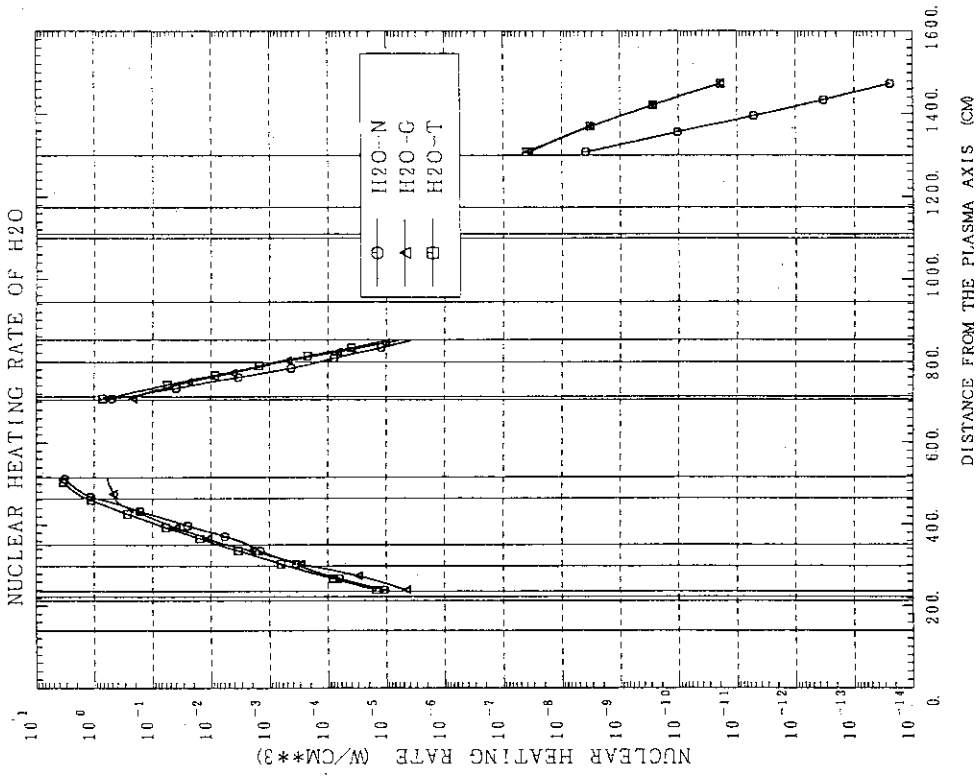

Fig. 6.6 Nuclear heating rate of H_2O (the cut with coordinate Z=586 cm in Fig.5.4) versus the distance in radial direction.

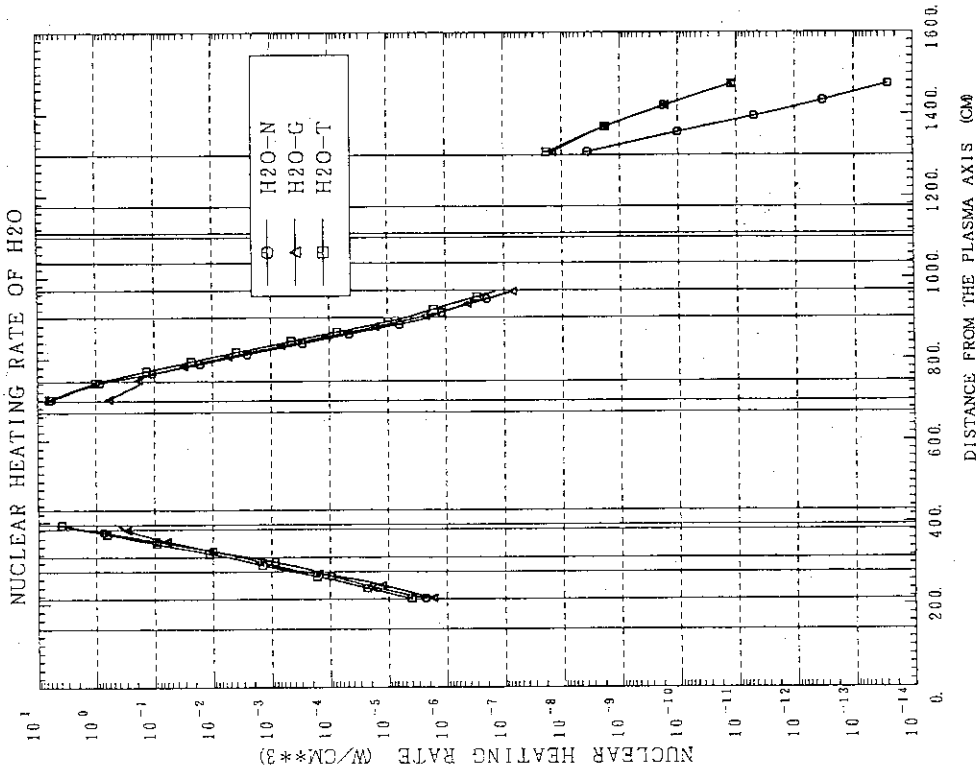

Fig. 6.5 Nuclear heating rate of H_2O (the cut with coordinate Z=342 cm in Fig.5.4) versus the distance in radial direction。

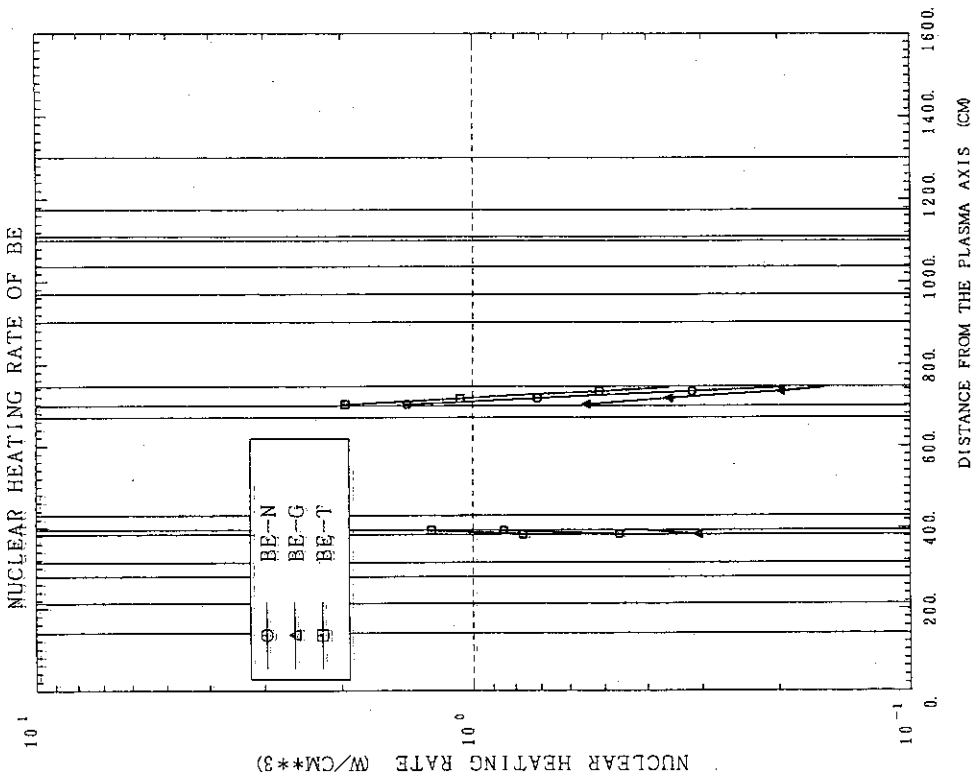

Fig. 6.8 Nuclear heating rate of Be (the cut with coordinate Z=342 cm in Fig.5.4) versus the distance in radial direction.

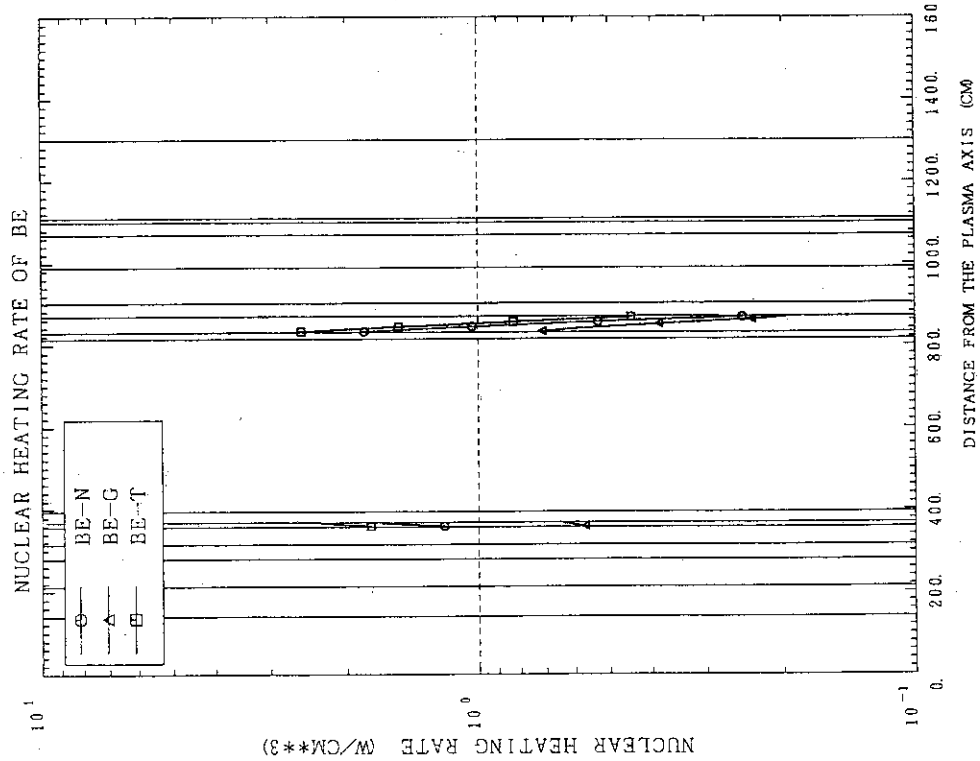

Fig. 6.7 Nuclear heating rate of Be (the cut with coordinate Z=4 cm in Fig.5.4) versus the distance in radial direction.

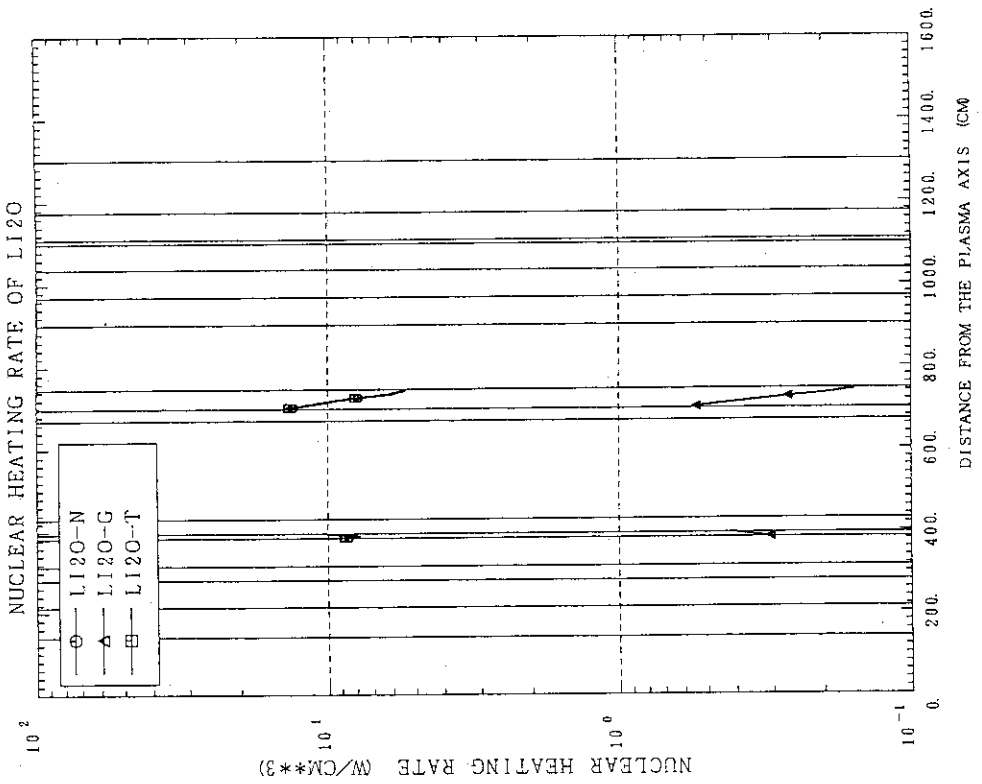

Fig. 6.10 Nuclear heating rate of Li_2O (the cut with coordinate Z=342 cm in Fig.5.4) versus the distance in radial direction.

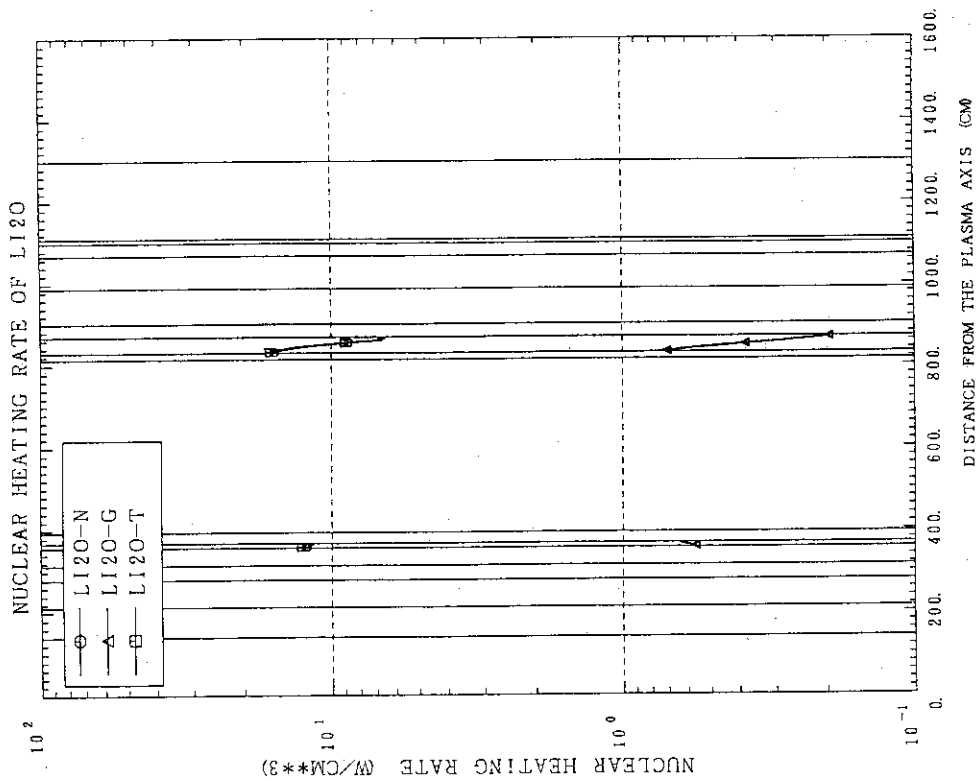

Fig. 6.9 Nuclear heating rate of Li_2O (the cut with coordinate Z=4 cm in Fig.5.4) versus the distance in radial direction.

7. Local and net tritium breeding ratio calculations.

Number of reports on TBR calculations were issued in Japan during and after ITER CDA, e.g. Refs. 13 and 14. However, the net TBR of Japanese blanket proposed for ITER was calculated [13] so far only for six layered pebble bed blanket concept proposed by Japan during ITER CDA. The net TBR of present reference Japanese blanket for ITER (three layered pebble bed concept) [14] was roughly estimated to be about 0.7, 90% of which were generated in the outboard blanket [14]. Above estimation was done by comparing the 1-D results of local TBR calculations for the ITER CDA Japanese reference blanket design (six layers of Li_2O) and present Japanese reference blanket design (three layers of Li_2O) developed after ITER CDA. Above comparison was done only for the outboard blankets at the toroidal midplane of ITER device [28].

The results of total TBR calculations obtained by over-all two-dimensional neutron transport calculations in this study are shown in Table 7.1. The tritium production rates for inboard and outboard toroidal midplane are shown in Figs. 7.1 and 7.2, respectively.

As it was discussed above, the homogeneous models of both inboard and outboard layered pebble bed blankets (present Japanese reference concept) were incorporated in the ITER over-all calculational models. Therefore, it has to be taken into account during comparison of present calculational results shown in Table 7.1 and those estimated in Ref. 14.

Generally it is believed that blanket homogenization leads to an increase of net TBR [29]. The one-dimensional calculations of local TBR in the outboard toroidal midplane were carried out to check the above statement. The homogeneous and heterogeneous one-dimensional cylindrical models of outboard ITER build-up in the toroidal midplane are shown in Figs. 7.3 and 7.4, respectively. The ANISN code [30] and above described FUSION-40 nuclear data library were employed for these calculations.

The 1.63 and 1.13 local TBR were obtained for homogeneous and heterogeneous calculational models, respectively. Thus, the TBR of outboard blanket in Table 7.1 is expected to be less than 0.6 by

factor 1.63/1.13. This estimation will give us the total TBR of about 0.5.

Additional calculations are to be done to get more accurate value of total TBR. Those calculations are to be done for 2-D or 3-D heterogeneous models with more detail calculational mesh, say less that 1 cm x 1 cm.

Table 7.1 The results of TBR calculations for homogeneous models of layered pebble bed blanket incorporated in the ITER over-all calculational model No.1.

Zone	TBR		
	in ^{6}Li	in ^{7}Li	Total
Inboard	0.111	0.003	0.11
Inboard with side wall effect /0.87/	0.097	0.003	0.096
Outboard	0.775	0.014	0.79
Outboard with port effect /0.914/ and side wall effect /0.835/	0.59	0.011	0.60
Outboard + inboard	-	-	0.70*

* This value was obtained for homogeneous blanket models. Heterogeneous models might decrease this value to 0.5 (see discussion in the chapter 7 of this study).

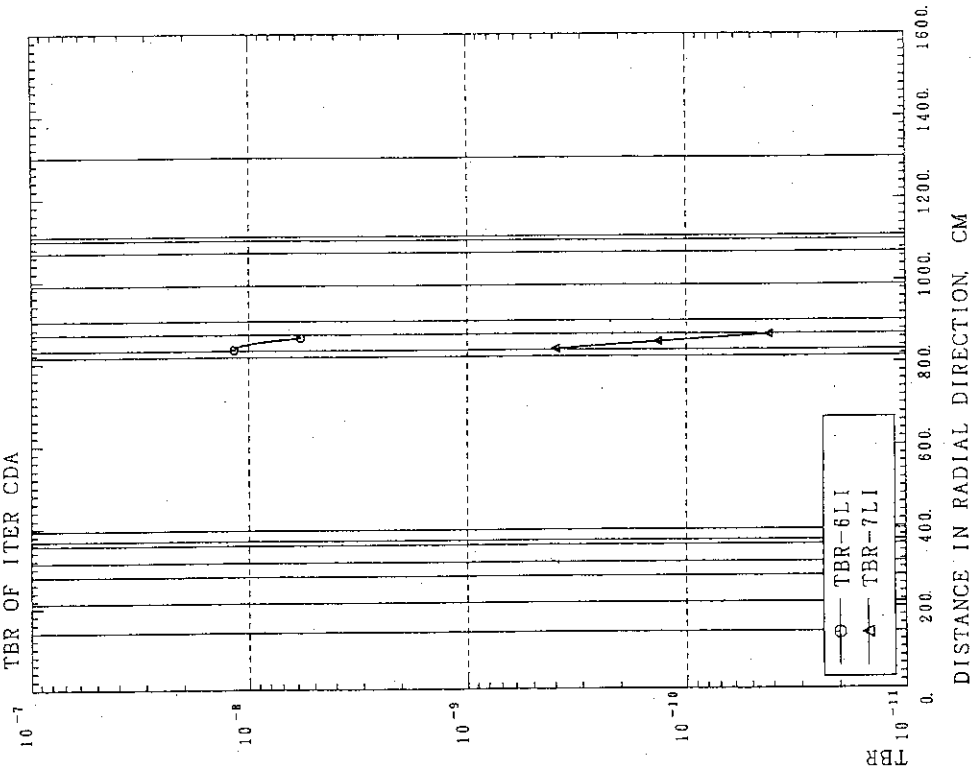

Fig. 7.2 Tritium breading ratio (TBR) of outboard breeder blanket of ITER versus the distance in radial direction (the cut with Coordinate Z=4 cm in Fig.5.4).

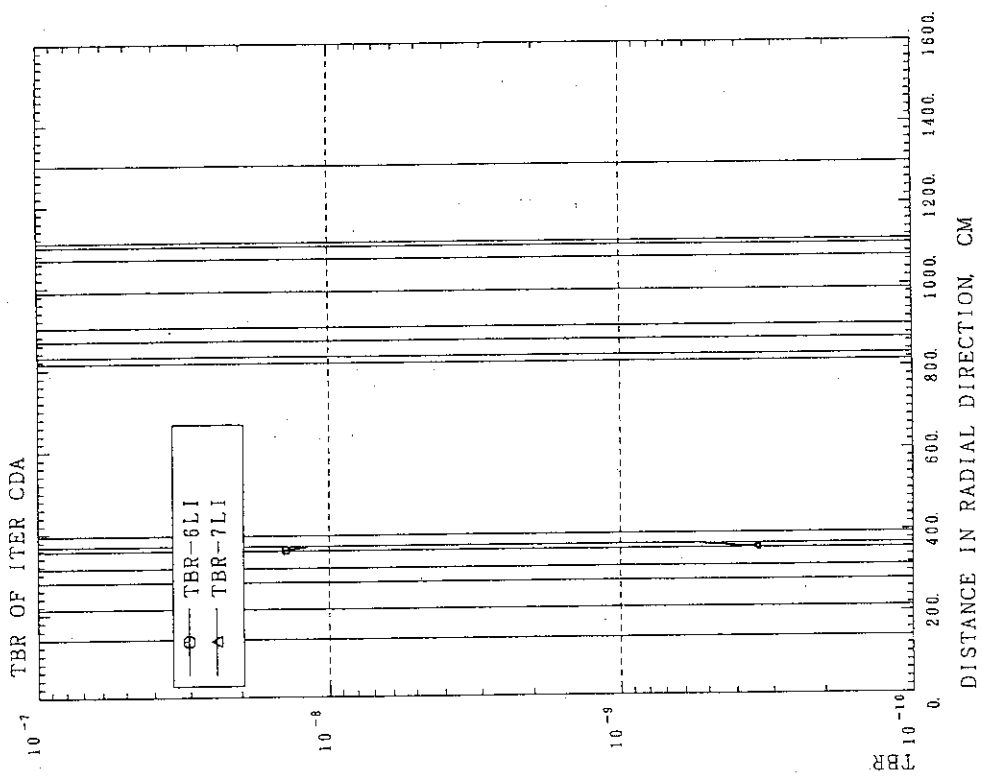

Fig. 7.1 Tritium breading ratio (TBR) of inboard breeder blanket of ITER versus the distance in radial direction (the cut with coordinate Z=4 cm in Fig.5.4).

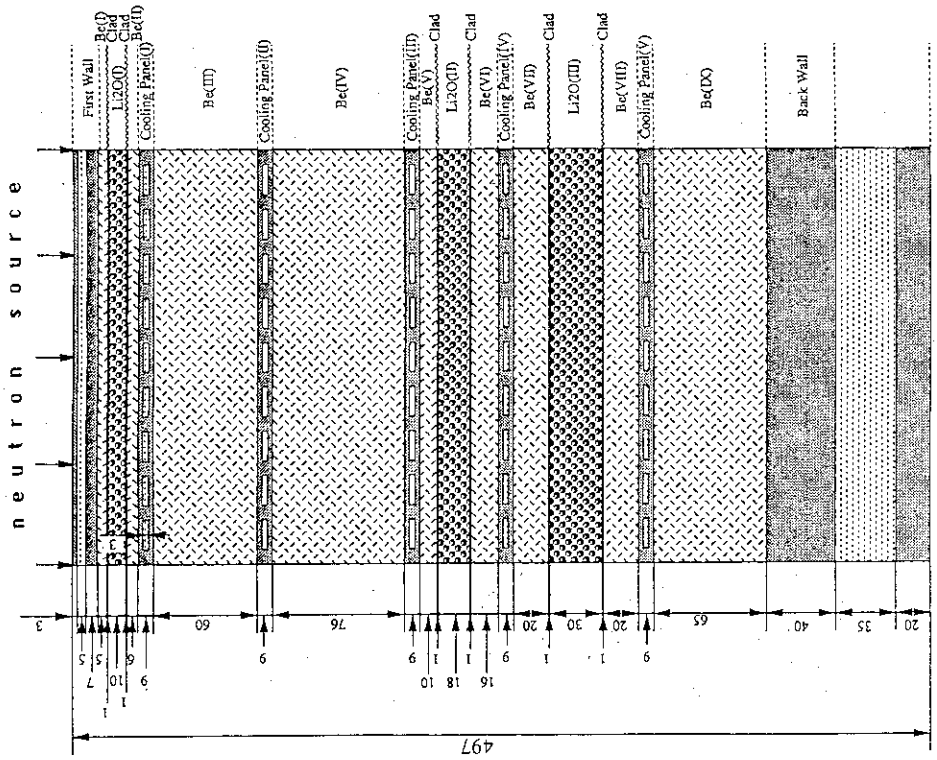

Fig. 7.4 The one-dimentional calculational model of outboard ITER build-up in the toroidal midplane with a heterogeneous breeding blanket described in Ref. 14.

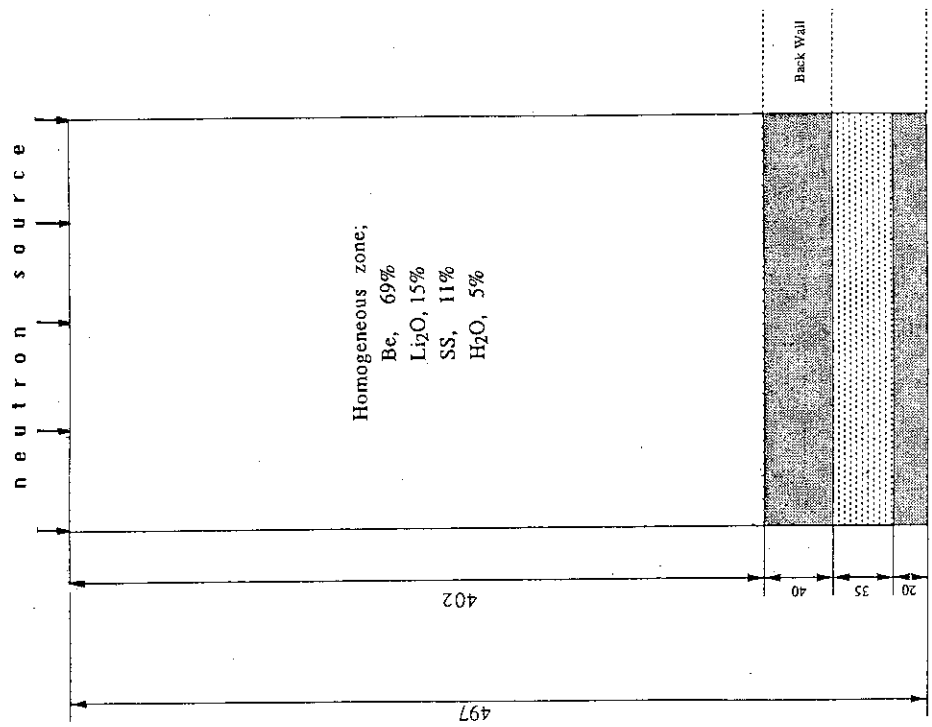

Fig. 7.3 The one-dimentional calculational model of outboard ITER build-up in the toroidal midplane with a homogeneous breeding blanket.

8. Analysis of exposure dose contour maps during the reactor operation and after reactor shutdown and the induced activity and decay heat calculations.

Two main materials /among employed in the calculational models 1-3 shown in Figs. 2.3-2.5, respectively/ which contribute in the shutdown dose are the copper and stainless steel. However, the stainless steel /SS316/ actually consists of number of impurity elements with minor densities which were not included in the neutron transport calculations and, correspondingly, are not shown in Table 2.1, namely C, Si, P, S, Mo, Co, N. Minor densities of above elements are not important for neutron transport calculations. On the contrary, for shutdown dose calculations the above-mentioned isotopes are to be taken into consideration. Therefore, all the above-mentioned isotopes were included in the SS316 for the calculations discussed in this paragraph. The atomic densities of these isotopes are shown in Table 8.1.

The calculational model N°1 in Fig. 2.3 was calculated in full energy region with the aim to provide for ITER EDA investigators both fast and total neutron fluxes and total gamma fluxes around the ITER CDA device. However, as it was shown above, the employed calculational model is expected to be overshielded (from the view point of biological shielding) because of the lack any large penetrations or void cavities (see Fig. 2.3). Thus the exposure dose calculations after reactor shutdown were not carried out for this calculational model. However, the exposure doses during reactor operation were calculated and shown in Figs. 8.1, 8.2 and 8.3 for the cases of total dose, neutron dose and gamma dose, respectively.

The maximum dose rate around the first wall is in the order of 10^{13} mrem/h, most of which is contributed by neutrons. Such high dose preclude human access and severely limits the installment of conventional sensors near the first wall.

The total, neutron and gamma-ray exposure doses during reactor operation for calculational models N° 2 and N° 3 are shown in Figs. 8.4-8.6 and 8.7-8.9, respectively.

According to Figs. 8.1-8.9, the personnel access during operation to the reactor room behind the concrete cryostat is not possible for all three above-mentioned calculational models. Just in the most propitious case of a cut across a TF coil, the total biological dose during operation behind the top cryostat lid is 100 mrem/h. This value is still about two orders of magnitude more than the limit established for personnel access 24 hours after shutdown.

The critical level of exposure shutdown dose is expected to be found for some zones in the cut between TF coils (calculational models in Figs. 2.4 and 2.5). Therefore we decided to calculate an exposure dose around ITER CDA device only for the above-mentioned calculational models, namely Nº2 (Fig. 2.4) and Nº3 (Fig. 2.5).

The dose rate distribution around the reactor one day after shutdown of the reactor following one year of continuous operation is shown in Fig. 8.10 for the most dangerous calculational model Nº2. The one-dimensional distribution of above-mentioned dose for the toroidal midplane (the cut "Z=4 cm" in Fig. 5.14) is shown in Fig. 8.11. According to the Fig. 8.11, the maximum shutdown dose rate appears around the first wall which is in the order of 10^8 mrem/h. Such a high dose rate should limit the selection of materials used in the repair and maintenance machines and should necessitate frequent replacement of radiation sensitive components such as sensors.

In Fig. 8.10, the radiation level ranges from about 10^{-3} mrem/h at the top zone of concrete cryostat to about 10^{-9} mrem/h at the midplane level of concrete cryostat. Above radiation level could permit the personnel access outside the concrete cryostat. However, numerous penetrations in the outboard reactor buildup will increase above value very much, e.g. the NBI duct etc. This problem has been considered in Refs. 5, 13.

The human access to the top zone of reactor room is not permissible when the calculational model Nº 2 is employed because the radiation level in the zone of reactor room behind the top cryostat lid nearly the bellows will become 0.1 mrem/h without a safety factor. Thus, just rather optimistic safety factor of ten recommended for the shutdown biological dose in the reference ITER CDA report [3] will rise the biological dose at above-mentioned zone

to about 1 mrem/h. More detail discussions on the safety factors is carried out in the next chapter.

The dose rate distribution around the reactor one day after shutdown of the reactor following one year of continuous operation is shown in Fig. 8.12 for the /conservative/ calculational model N°3. According to the Fig. 8.12 the radiation level in the zone of reactor room behind the top cryostat lid nearly the bellows will become 10^{-2} - 10^{-3} mrem/h without a safety factor. Thus, just with a conservative safety factor of about 50 the biological dose rate in the zone of reactor room behind the top cryostat lid nearly the bellows 24 hours after shutdown is expected to be less the limit. Therefore, the human access to the top zone of the reactor room is to be possible in this case.

The results of induced activity and decay heat calculations for the inboard vacuum vessel, the inboard first wall, the divertor surface, the outboard first wall, the front surface of outboard vacuum vessel and the back surface of outboard vacuum vessel are shown in Figs. 8.13-8.24, respectively. These results were obtained for the calculational model N°2 shown in Fig. 2.4. The results of induced activity and decay heat calculations integrated by all zones of model N°2 are shown in Figs. 8.25 and 8.26, respectively.

Table 8.1 Atomic number densities of stainless steel elements employed for shutdown dose calculations.

Element	Number density, atom/cm^3 (=10^{24}/cm^3)
C	$2.801 \cdot 10^{-4}$
Si	$7.700 \cdot 10^{-3}$
Mn	$1.662 \cdot 10^{-3}$
P	$4.034 \cdot 10^{-5}$
S	$1.799 \cdot 10^{-5}$
Ni	$1.051 \cdot 10^{-2}$
Cr	$1.538 \cdot 10^{-2}$
Mo	$1.147 \cdot 10^{-3}$
Fe	$5.635 \cdot 10^{-2}$
Co	$2.283 \cdot 10^{-4}$
N	$3.431 \cdot 10^{-5}$

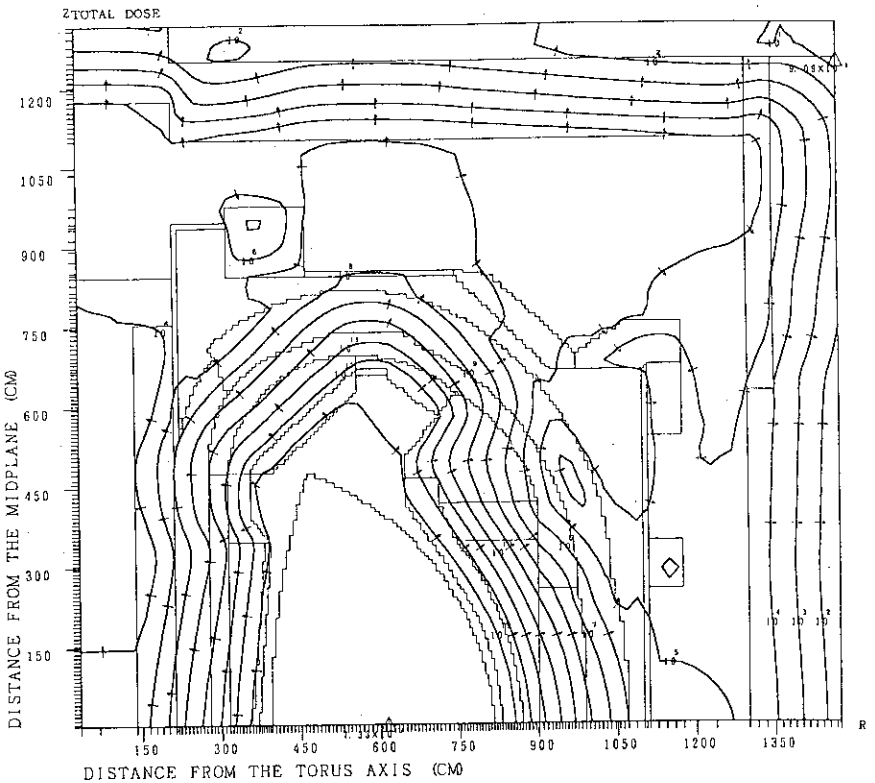

Fig. 8.1 Total exposure dose (model No.1) during the reactor operation (the contour lines represent values corresponding to $1x10^n$ mrem/h. The arrows show the direction of the downward gradient of the exposure dose).

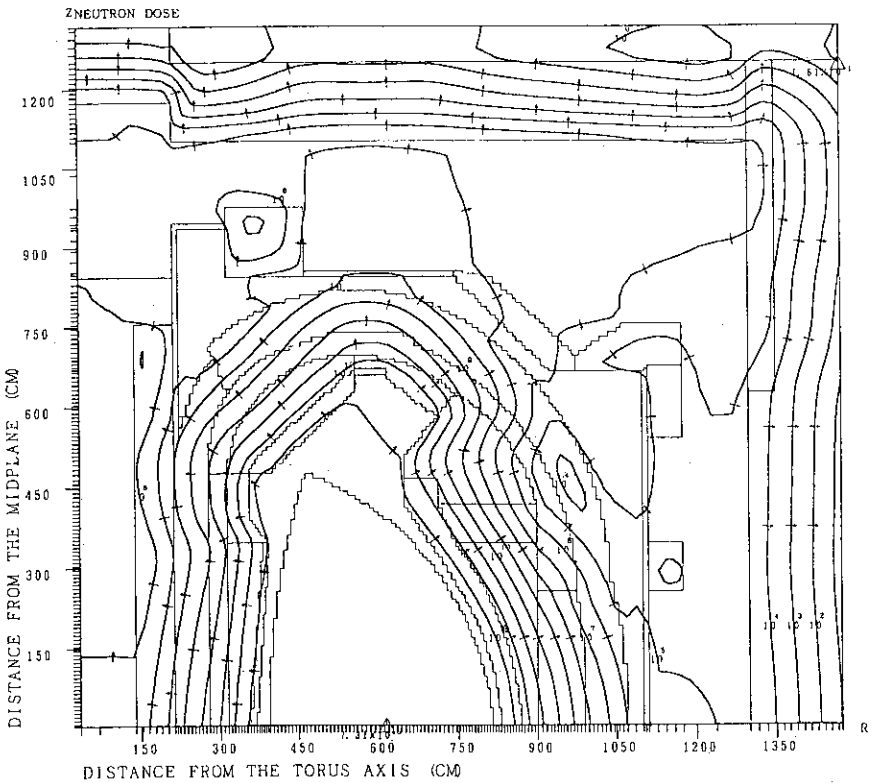

Fig. 8.2 Neutron exposure dose (model No.1) during the reactor operation (the contour lines represent values corresponding to $1x10^n$ mrem/h. The arrows show the direction of the downward gradient of the exposure dose).

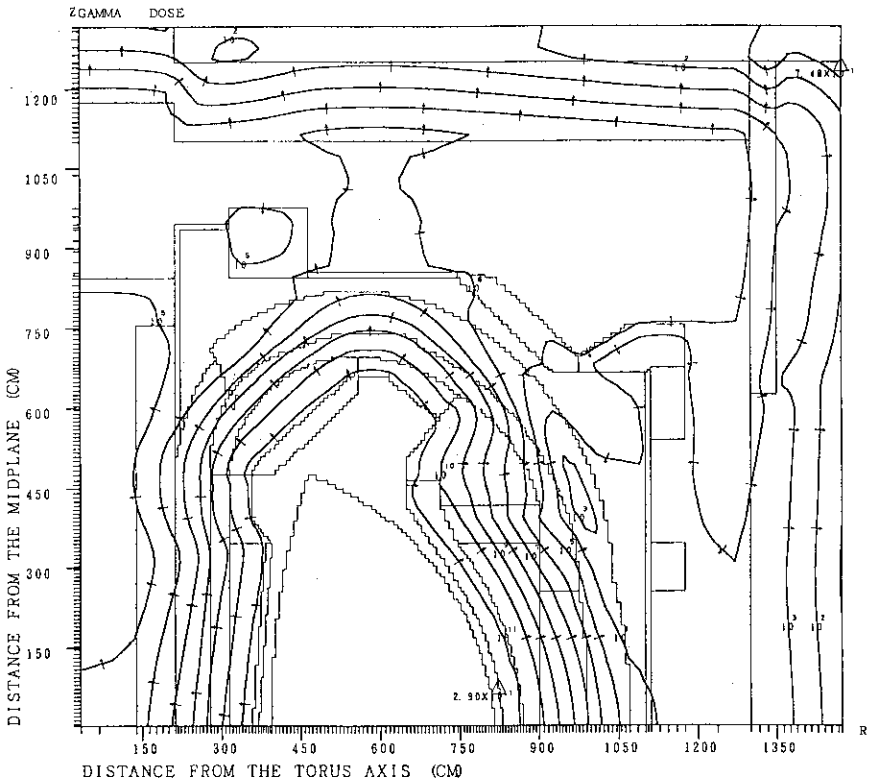

Fig. 8.3 Gamma-ray exposure dose (model No.1) during the reactor operation (the contour lines represent values corresponding to $1x10^n$ mrem/h. The arrows show the direction of the downward gradient of the exposure dose).

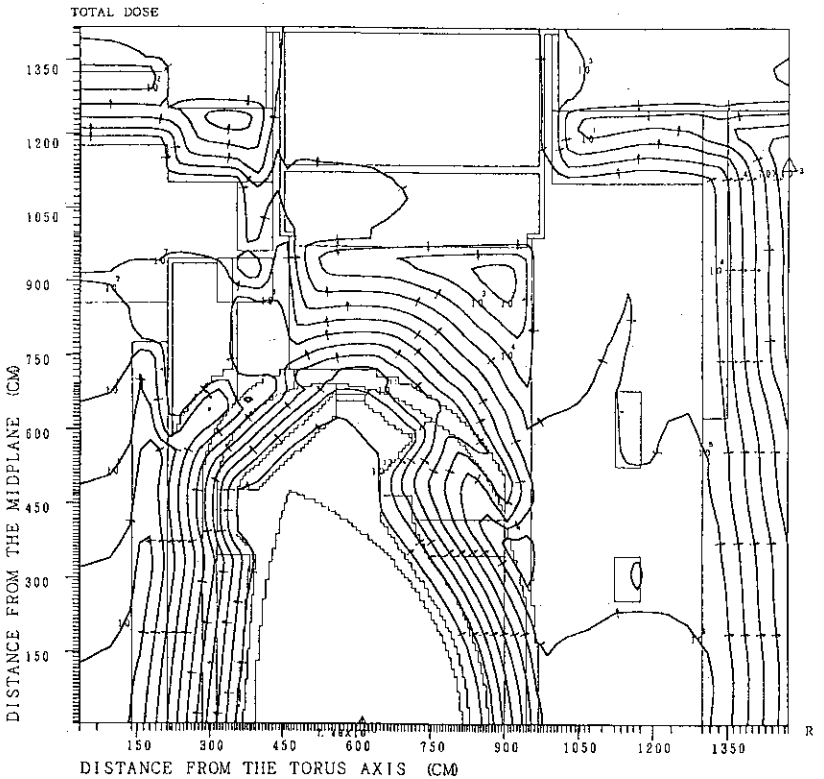

Fig. 8.4 Total exposure dose (model No.2) during the reactor operation (the contour lines represent values corresponding to $1x10^n$ mrem/h. The arrows show the direction of the downward gradient of the exposure dose).

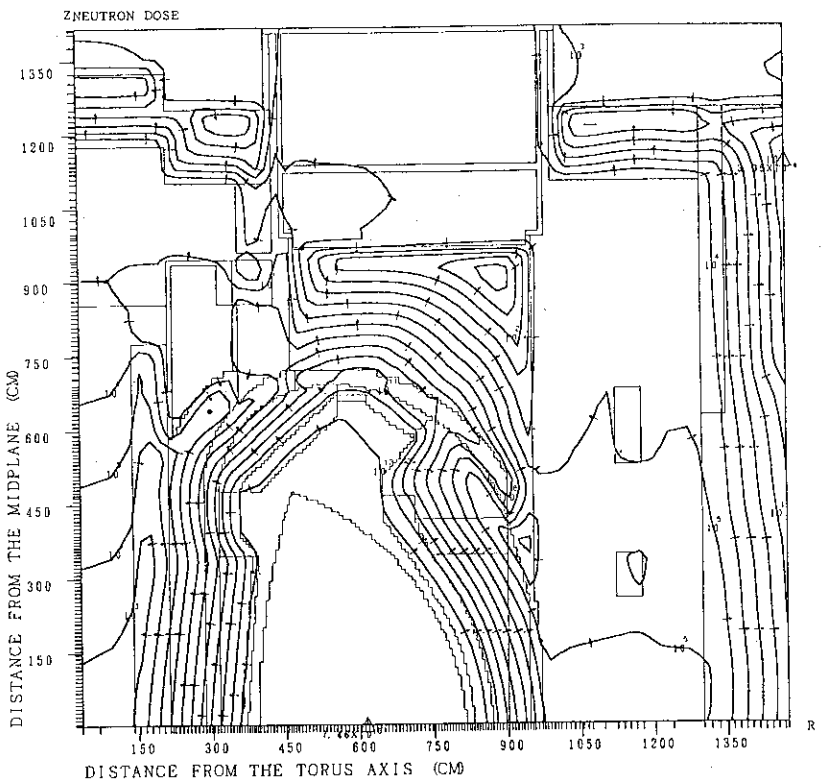

Fig. 8.5 Neutron exposure dose (model No.2) during the reactor operation (the contour lines represent values corresponding to 1×10^n mrem/h. The arrows show the direction of the downward gradient of the exposure dose).

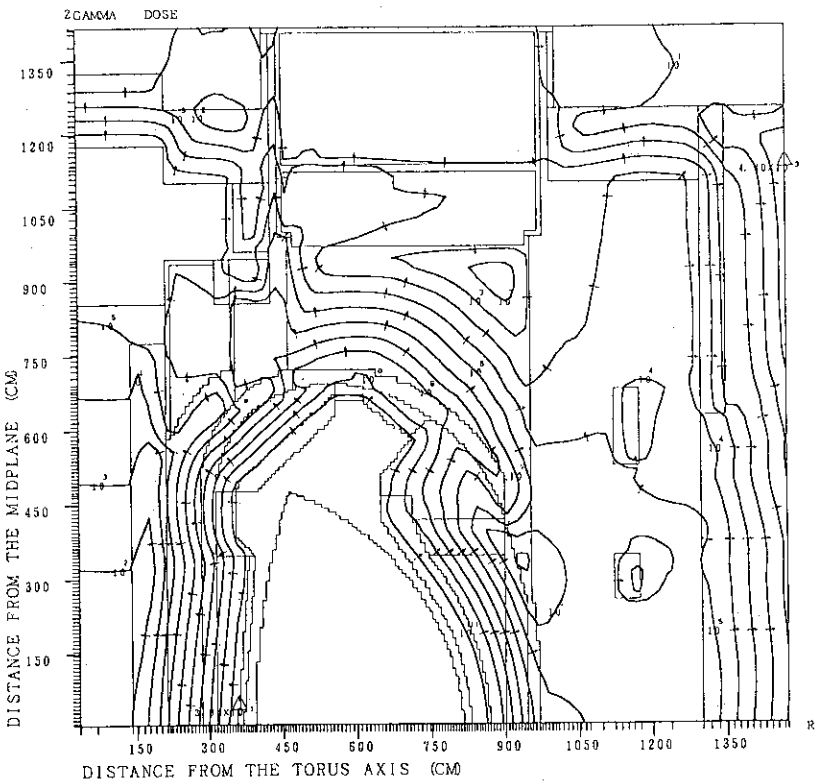

Fig. 8.6 Gamma-ray exposure dose (model No.2) during the reactor operation (the contour lines represent values corresponding to 1×10^n mrem/h. The arrows show the direction of the downward gradient of the exposure dose).

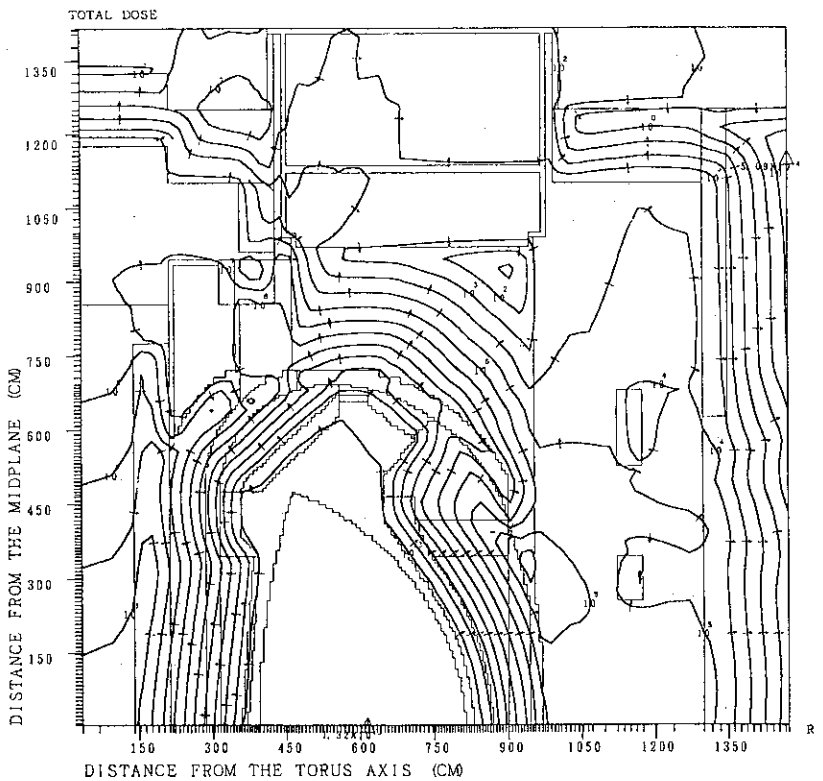

Fig. 8.7 Total exposure dose (model No.3) during the reactor operation (the contour lines represent values corresponding to 1×10^n mrem/h. The arrows show the direction of the downward gradient of the exposure dose).

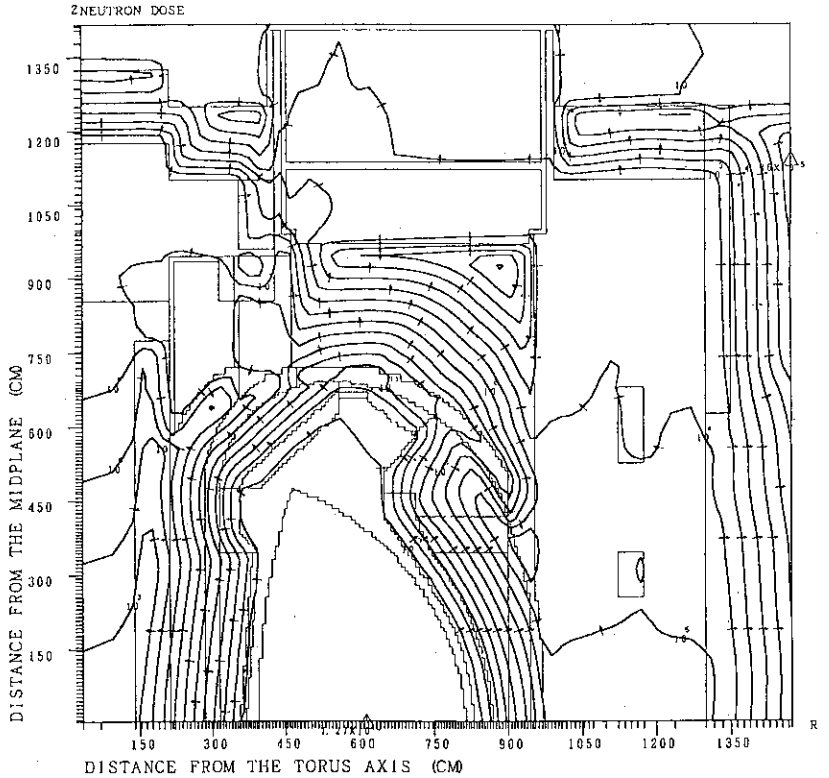

Fig. 8.8 Neutron exposure dose (model No.3) during the reactor operation (the contour lines represent values corresponding to 1×10^n mrem/h. The arrows show the direction of the downward gradient of the exposure dose).

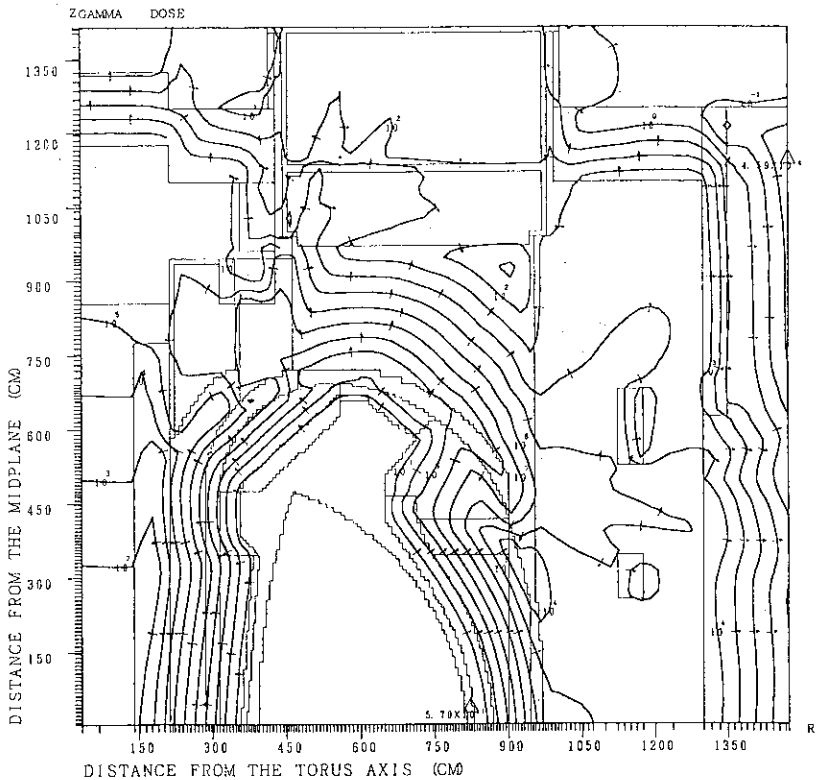

Fig. 8.9 Gamma-ray exposure dose (model No.3) during the reactor operation (the contour lines represent values corresponding to $1x10^n$ mrem/h. The arrows show the direction of the downward gradient of the exposure dose),

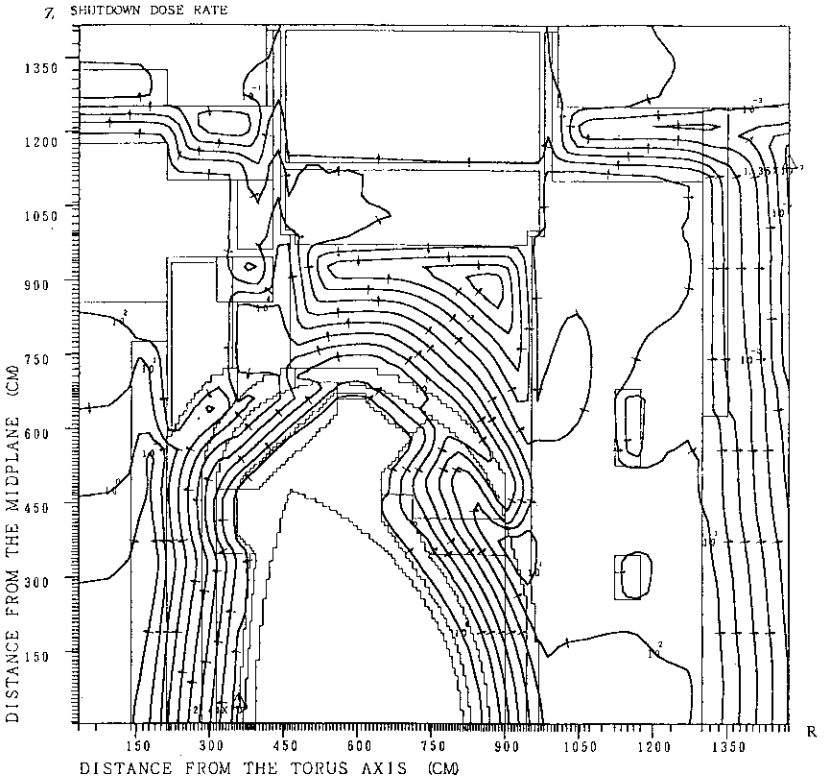

Fig. 8.10 Biological dose 24 hors after shutdown of the ITER following one year of its continuous operation (The contour lines represent values corresponding to $1x10^n$ mrem/h. The arrows show the direction of the downward gradient of the exposure dose).

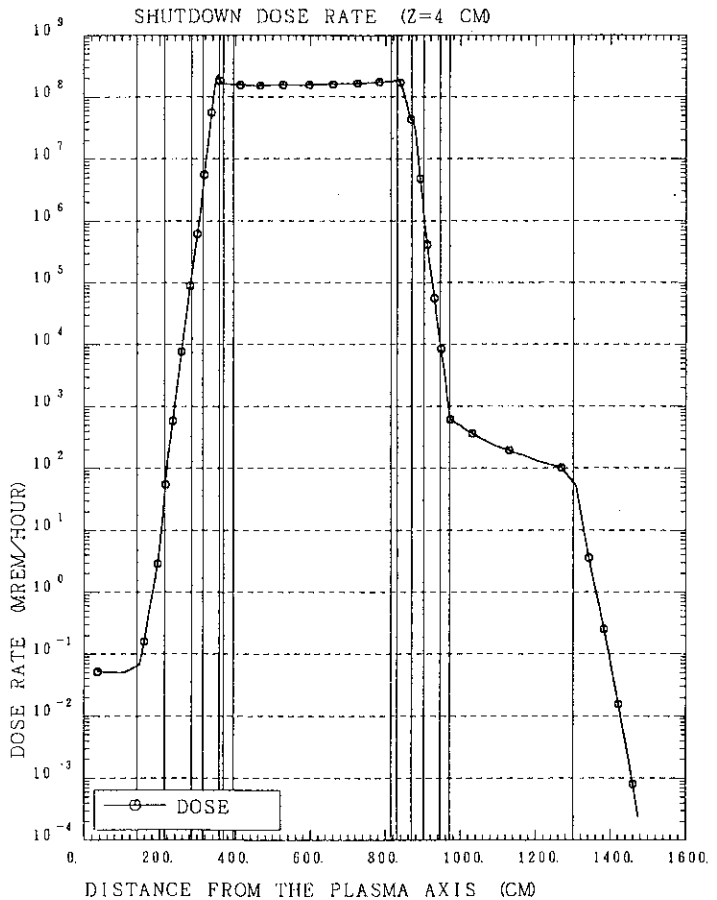

Fig. 8.11 Biological dose 24 hors after shutdown of the ITER following one year of its continuous operation (the cut with Z=4 cm in Fig.5.14) versus the distance in the radial direction.

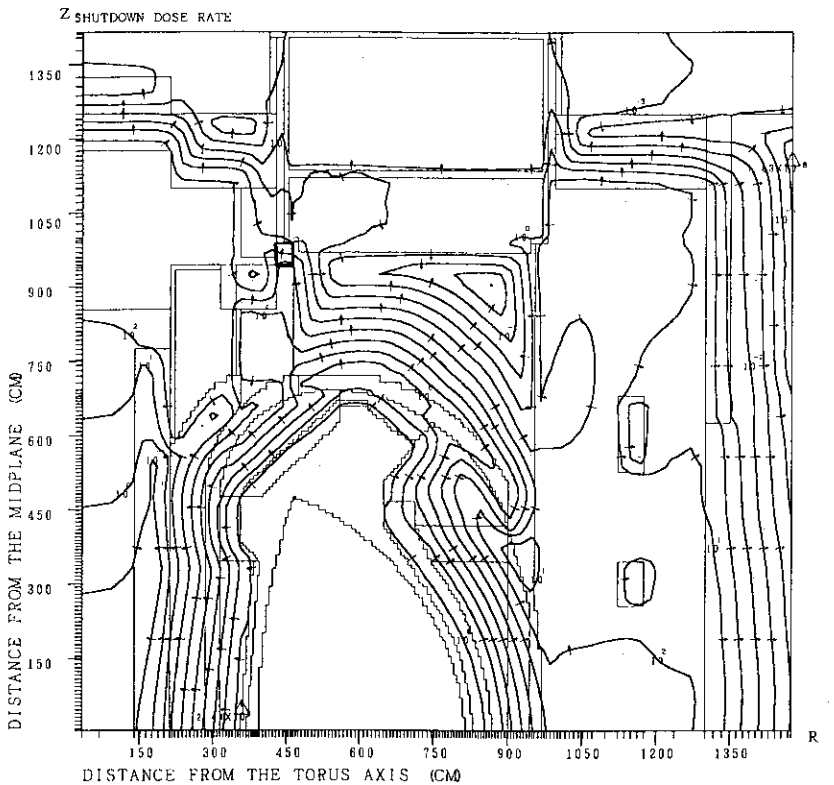

Fig. 8.12 Biological dose 24 hors after shutdown of the ITER following one year of its continuous operation (The contour lines represent values corresponding to $1x10^n$ mrem/h. The arrows show the direction of the downward gradient of the exposure dose).

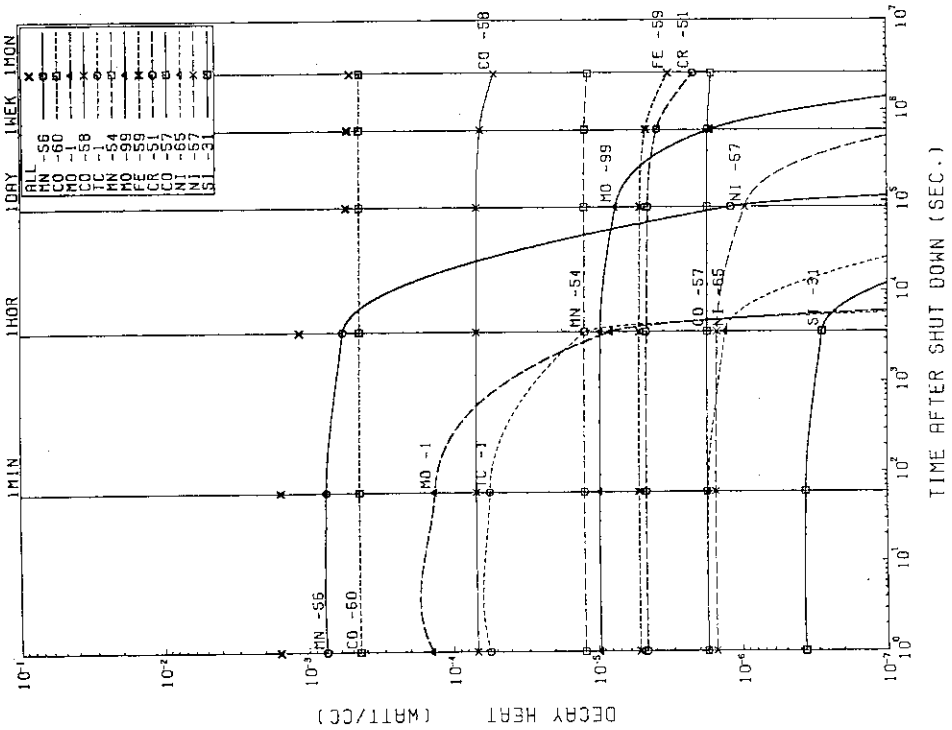

Fig. 8.14 The results of decay heat calculations at the inboard vacuum vessel (Calculation model No.2, R=315 cm, Z=0 cm).

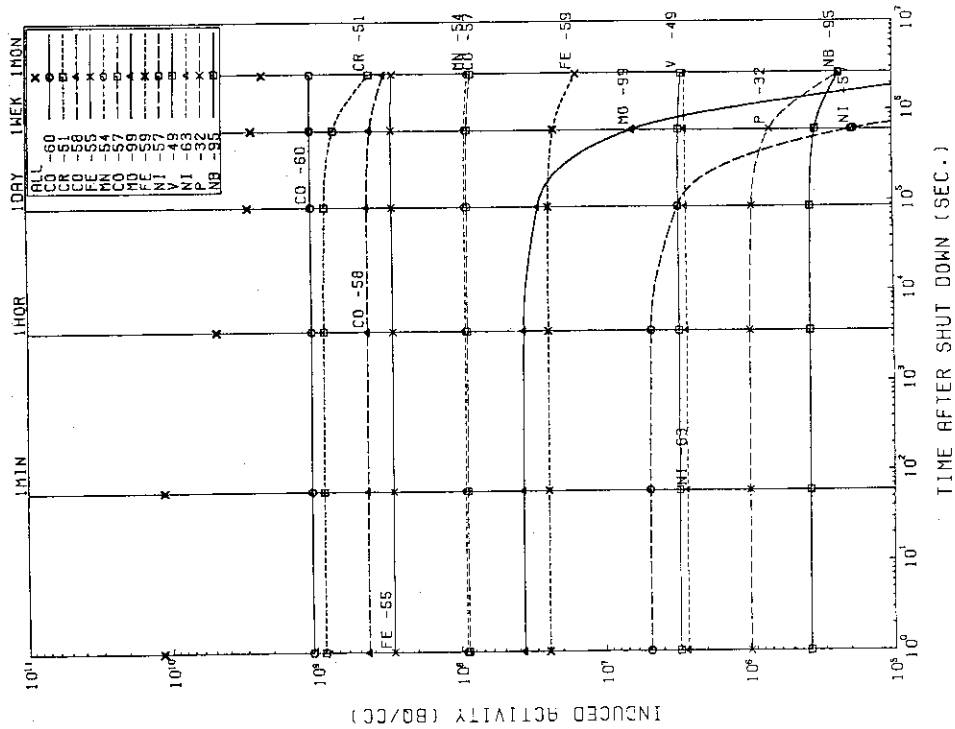

Fig. 8.13 The results of induced activity calculations at the inboard vacuum vessel (Calculation model No.2, R=315 cm, Z=0 cm).

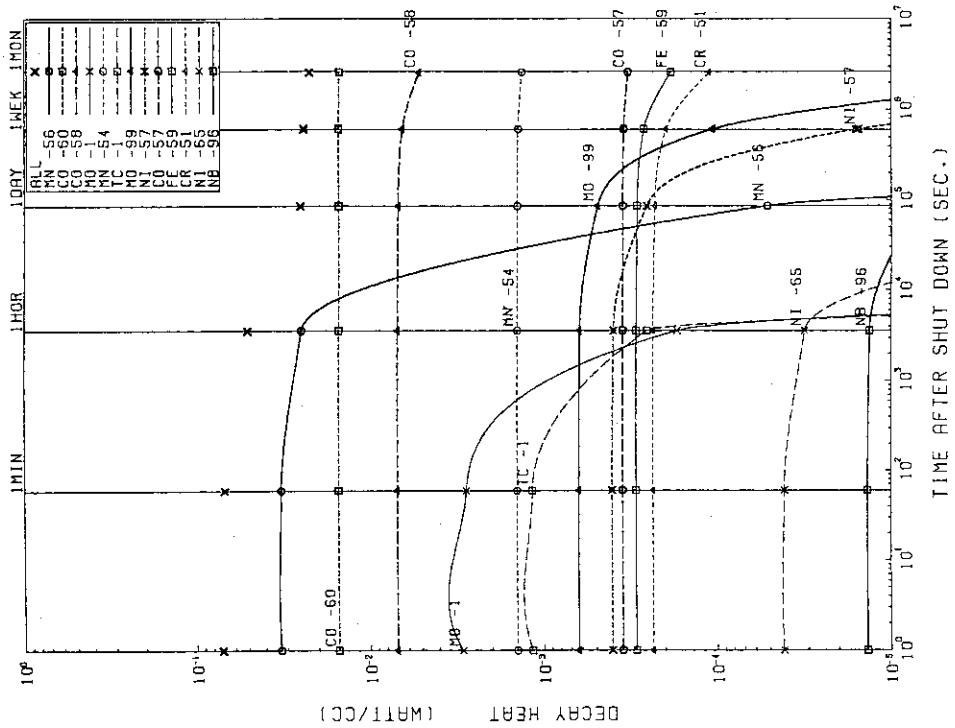

Fig. 8.16 The results of decay heat calculations at the inboard first wall (Calculation model No.2, R=315 cm, Z=0 cm).

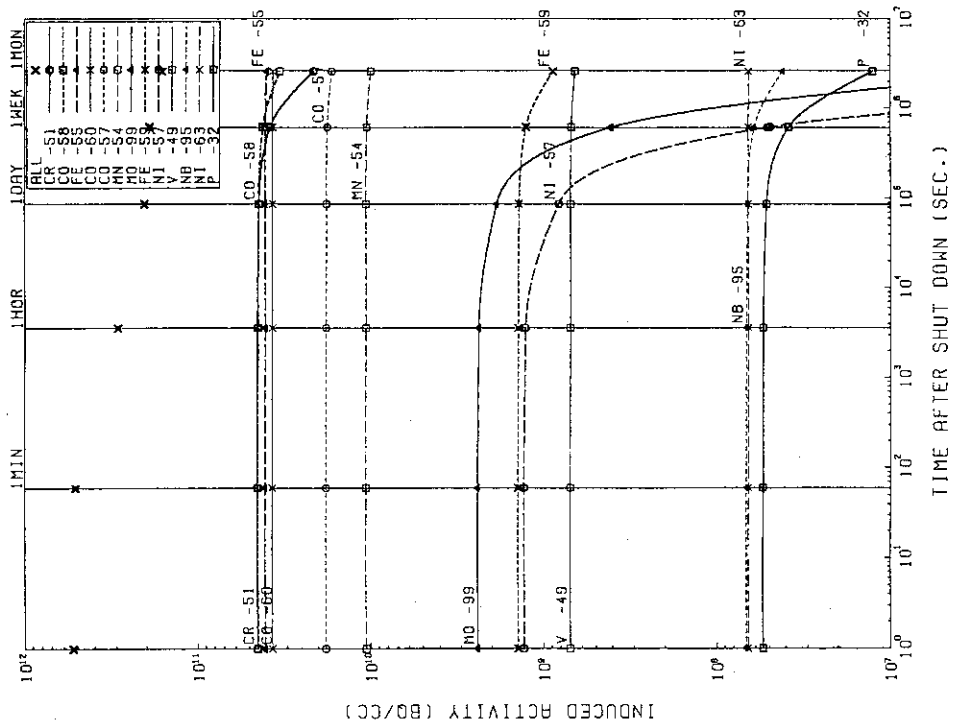

Fig. 8.15 The results of induced activity calculations at the inboard first wall (Calculation model No.2, R=369 cm, Z=0 cm).

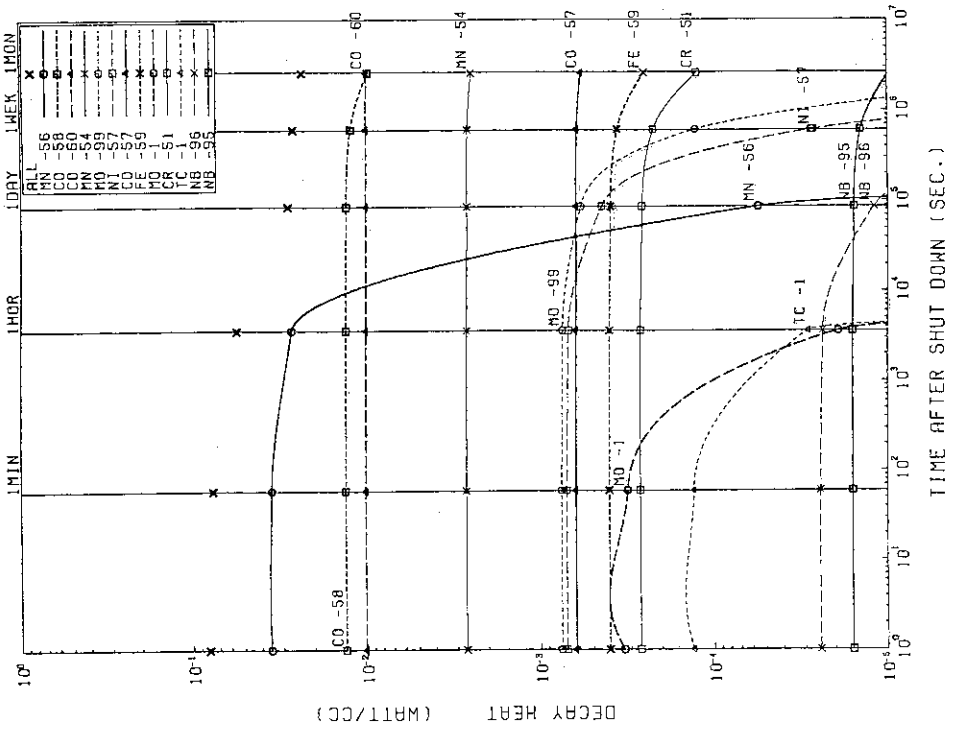

Fig. 8.18 The results of decay heat calculations at the divertor surface (Calculation model No.2, R=450 cm, Z=526 cm).

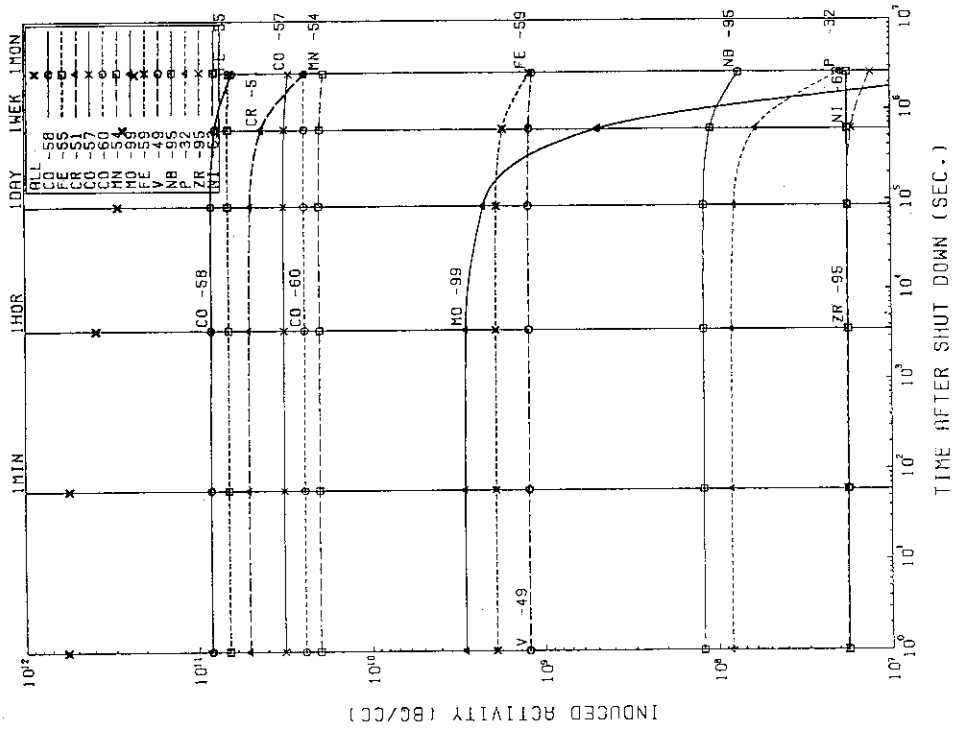

Fig. 8.17 The results of induced activity calculations at the divertor surface (Calculation model No.2, R=450 cm, Z=526 cm).

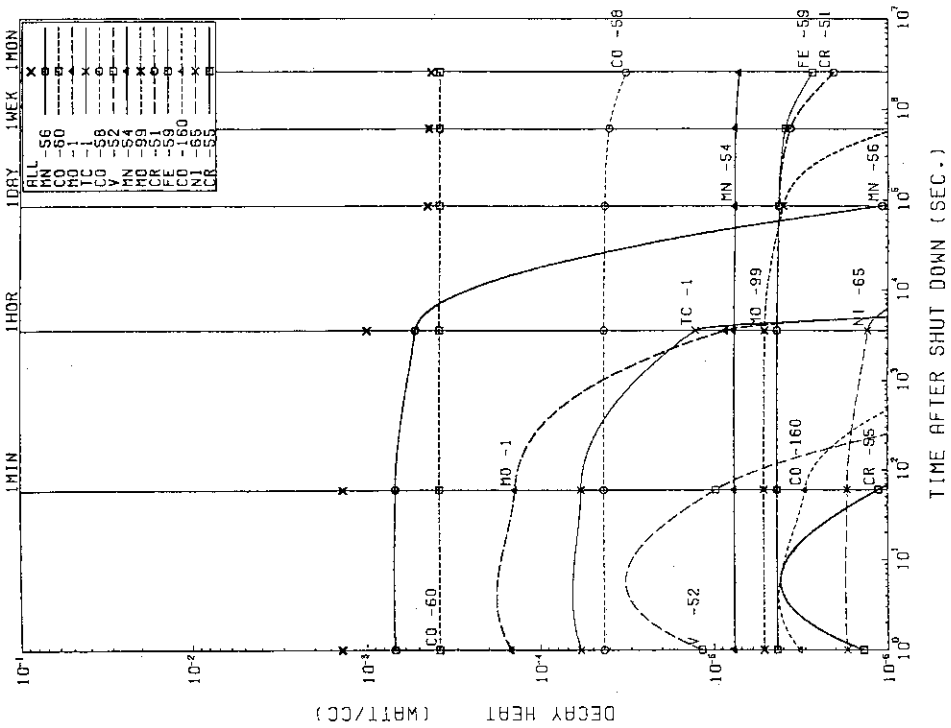

Fig. 8.20 The results of decay heat calculations at the outboard first wall (Calculation model No.2, R=830 cm, Z=0 cm).

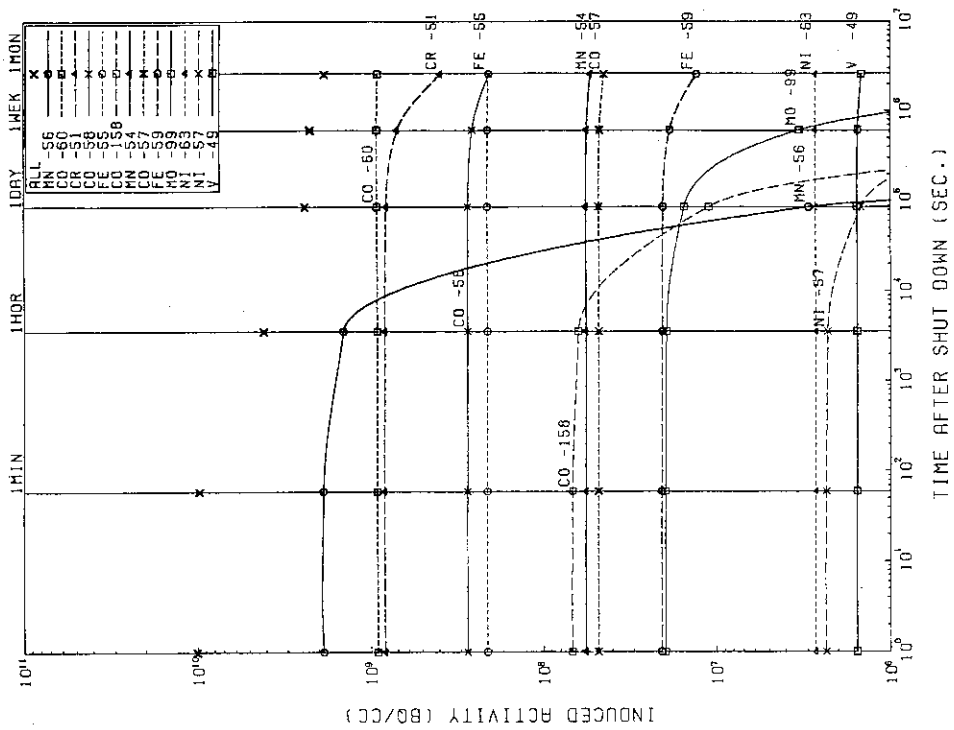

Fig. 8.19 The results of induced activity calculations at the outboard first wall (Calculation model No.2, R=830 cm, Z=0 cm).

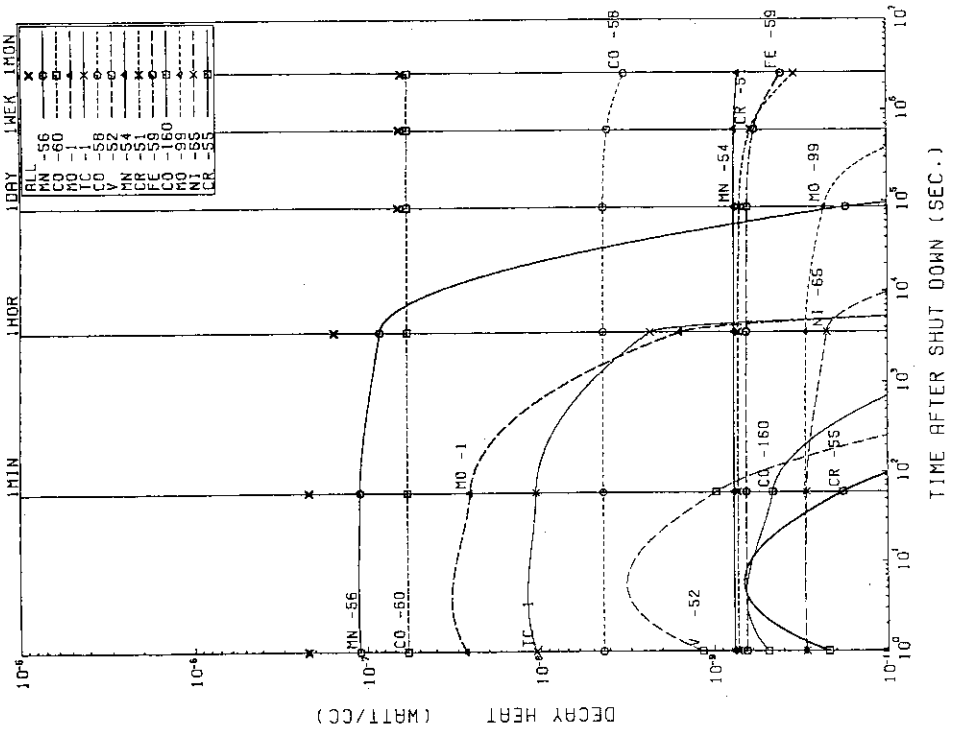

Fig. 8.22 The results of decay heat calculations at the front surface of outboard vacuum vessel (Calculation model No.2, R=901 cm, Z=0 cm).

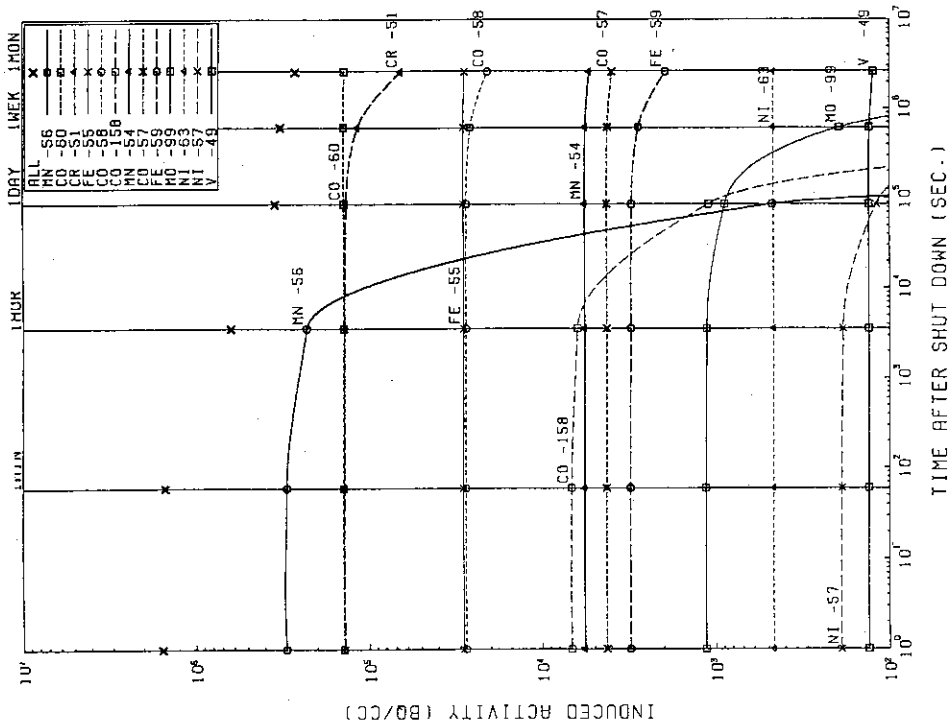

Fig. 8.21 The results of induced activity calculations at the front surface of outboard vacuum vessel (Calculation model No.2, R=901 cm, Z=0 cm).

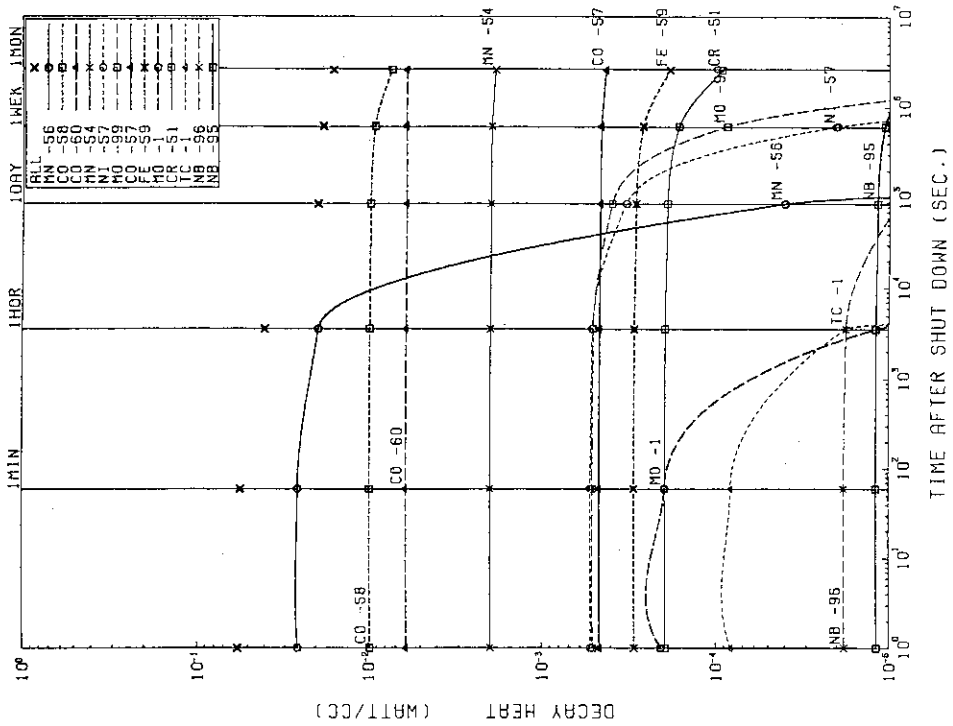

Fig. 8.24 The results of decay heat calculations at the back surface of outboard vacuum vessel (Calculation model No.2, R=901 cm, Z=0 cm).

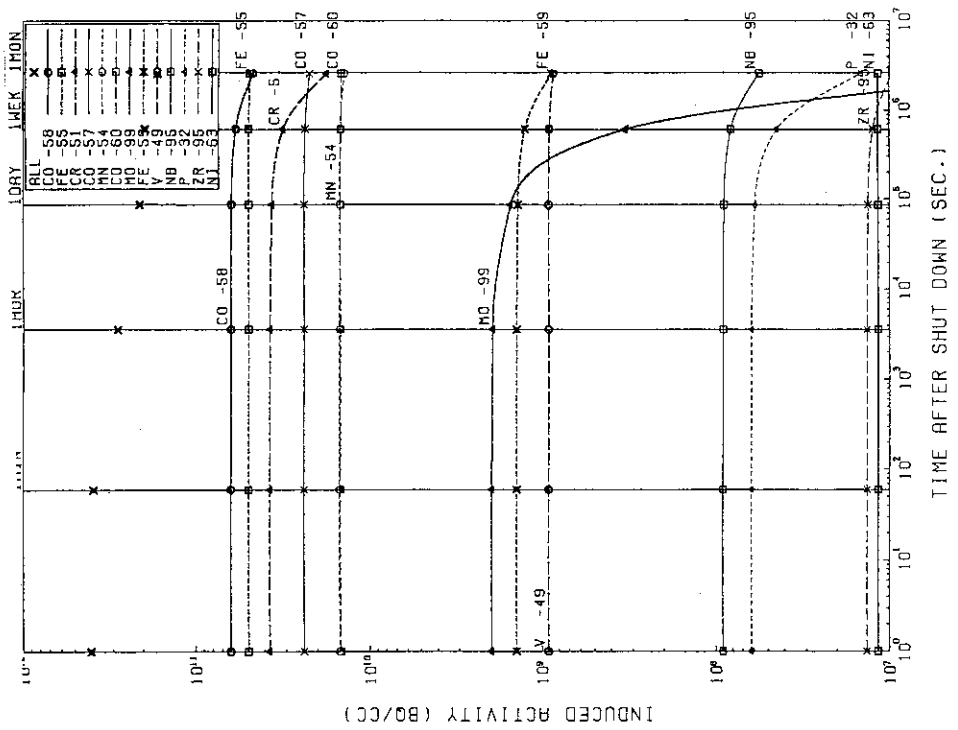

Fig. 8.23 The results of induced activity calculations at the back surface of outboard vacuum vessel (Calculation model No.2, R=901 cm, Z=0 cm).

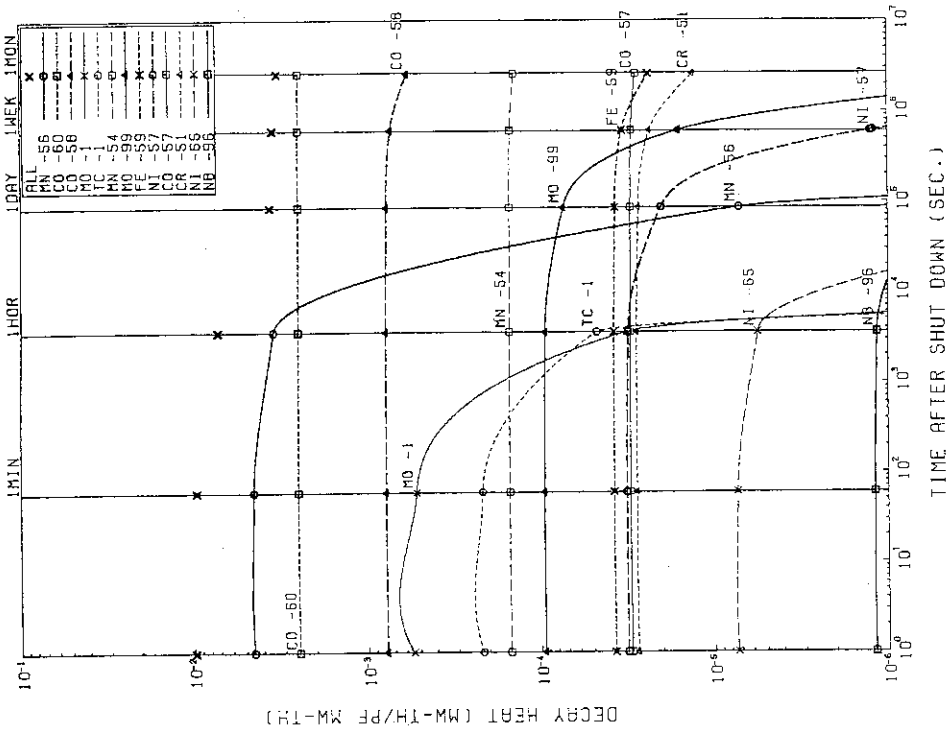

Fig. 8.26 The results of decay heat calculations integrated at all zones of calculation model No.2.

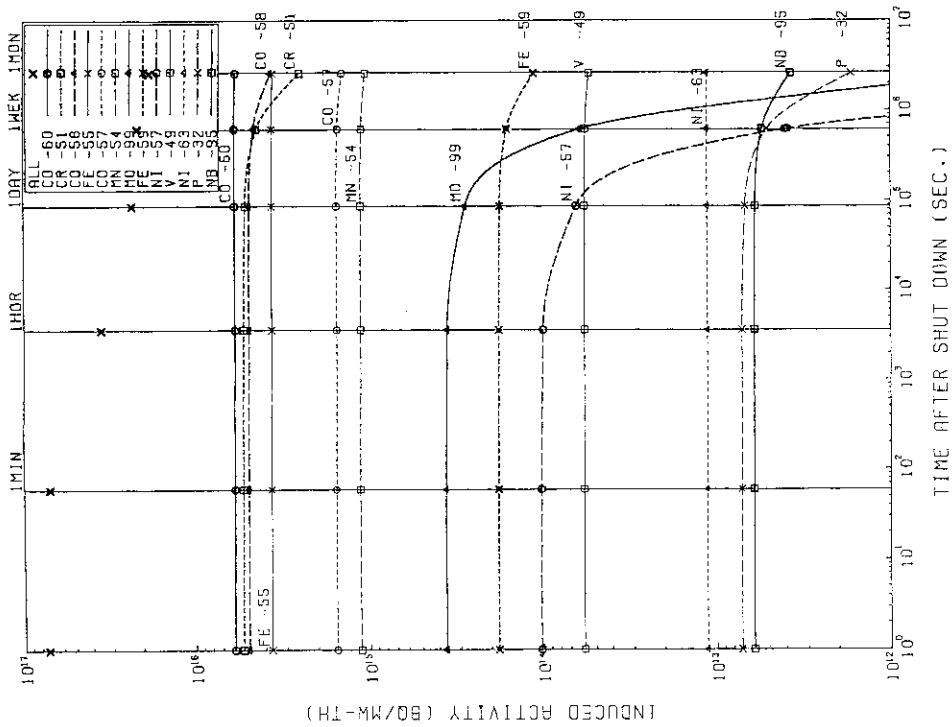

Fig. 8.25 The results of induced activity calculations integrated at all zones of calculation model No.2.

9. Consideration on calculation accuracy.

The uncertainty of the calculational results for the neutron fluxes and the biological dose is caused by restrictions of numerical method and calculational models, namely the mesh width, energy group number, angular quadratures etc. The safety factor of ten was recommended to be used for the biological dose rate analyses after shutdown during ITER CDA [3].

However, the above mentioned safety factor was employed for the bulk shield analyses. An additional source of uncertainty in this study is the difficulty of modelling the real ITER geometry. This is especially important for the zone 31 in Fig. 2.4. This zone was modelled in the two-dimensional cylindrical geometry as void rings. However, in the real ITER geometry above zone is alternative sectors /in toroidal direction/ of a void and a solid steel hardware. Further, the large size of the calculational models employed in this study /about 14 meters x 14 meters/ is expected to be an additional source of a large calculational error.

Therefore, it is expected that the safety factor of ten used in the reference ITER CDA report [3] can not be applied for the shutdown biological dose obtained in this study. It is expected that this safety factor will more than ten depending on a zone of the interest. However, these values of a safety factor are to be highly system dependent and have to be seriously rediscussed during ITER EDA.

The safety factor for the neutron fluxes depends much on the distance from the neutron source (plasma). It is expected that the safety factor for fast neutron flux can range from 1.5-2 to 10 for the fast neutron flux on the back blanket surface and behind the cryostat, respectively [3]. However this is not fully examined.

Safety factors for nuclear heating were not discussed during ITER CDA and, indisputably are to be seriously discussed during ITER EDA. The only safety factor for nuclear heating in TF coils was discussed during ITER CDA and had been recommended, namely 2.

It should be underlined that above the calculational results are to be checked during ITER EDA, e.g. by Monte Carlo calculations

and/or by comparison with experiments. As it was mentioned above, it is almost impossible to use Monte Carlo method for over-all ITER neutron transport calculations. However, it is possible to check some questionable zones pointed out in this study by Monte Carlo calculations, e.g. the radiation streaming through the void cavities (zone 31 in Fig. 2.4) in the top zone of ITER CDA over-all calculational model Nº2 considered in this study. Thus, it is seriously suggested to investigate at the very beginning of ITER EDA, the possibility of personnel access at the numerous questionable places at the top zone of ITER device.

10. Conclusions.

The major conclusions that can be drawn from this over-all calculational analysis of ITER CDA are :

1. Useful two-dimensional contour maps of 14-MeV, fast and total neutron fluxes and total gamma fluxes were obtained in this study. It is expected that the results of the present study are used as a starting point for the neutronics study of ITER EDA. The one-dimensional distributions of the above fluxes have been provided for some most important cuts of ITER device in toroidal directions as well.

2. The design of a steel-rich /80%SS + 20%H_2O/ top semi-permanent shield behind the divertor plates is recommended. The above shield would decrease a shutdown dose at the zone behind the top maintenance shield plug by 1-2 orders of magnitude in comparison with the case of a water-rich /20%SS + 80%H_2O/ top semi-permanent shield.

3. The results of total nuclear heating calculations in in-vessel and out-vessel components of ITER device are confirmed to be reasonable. These results can be used for thermal/hydraulics analyses of ITER components. However, the safety factors for results obtained in this study are to be discussed further during ITER EDA.

4. The total nuclear heating in the divertor plates was estimated to be 77 MW which is about 60% more than the former rough estimation during ITER CDA. It is well explained by the difference of volume of divertor zone employed in the calculations, namely the rib structure behind the divertor plates was included in the volume of divertor zone in this study.

5. The result obtained in this study for the total nuclear heating of 210 kW in TF coils was substantially overestimated, namely by 4-5 times in comparison with the results shown in the ITER CDA

reference report. The main reason of above error seems to be the geometrical description employed in the calculational model. It is especially critical for the top zone of ITER, namely the zone behind the divertor piping were the total shield thickness /including the vacuum vessel zone/ is less than 60 cm [3]. Further, the homogenization of blanket, shield and vacuum vessel zones and neglecting some design modifications of ITER shield developed during ITER CDA, e.g. neglecting the 4 cm B_4C/Pb layer behind vacuum vessel could be an additional source of overestimation of total heating in TF coils.

6. The net TBR of ITER device with the Japanese reference Li_2O/Be pebble bed driver blanket was estimated to be about 0.5. More detail multidimensional calculations of net TBR are to be done during ITER EDA for heterogeneous realistic calculational models of the above blanket.

7. Useful two-dimensional contour maps of biological dose during reactor operation were obtained in this study for all considered geometrical models.

8. The operational biological dose behind the cryostat ranges from about 10 mrem/h to about 1000 mrem/h at the toroidal midplane and on the surface of top cryostat lid, respectively. It will restrict the personal access in reactor room during the ITER operation.

9. The ITER CDA reference design has serious weak points regarding the biological shield design, e.g. the void zone in the top ITER region between the poloidal field coil and the shield plug. Therefore, the biological shutdown dose at the top zone of the ITER shield plug close to the bellows is in the order of the 0.1 mrem/h without safety factor. However, if the safety factor ranges from 10 to 100, the shutdown biological dose at the top zone of the ITER shield plug close to the bellows will range from 1 mrem/h to 10 mrem/h,

respectively. This value is more than the 0.5 mrem/h limit employed in the reference ITER CDA report [3].

10. An additional shield of 30-40 cm thickness has to be placed in the gap between the concrete cryostat and the wall of a shield plug in order to decrease the shutdown biological dose in the top zone of ITER shield plug close to the bellows well below the limit. The form of this shield was proposed and calculated in this study. In that case, at 24 hours after shutdown, the dose rate is such that human access above the shield plug will be allowed for a limited time.

11. The uncertainty of biological shield calculations in some zones where the neutron/gamma streaming effects are pronounced can reach up to 2 orders of magnitude for DOT3.5 calculations. Thus the above presented over-all ITER CDA neutron transport calculations will have to be recalculated during ITER EDA, say by the Monte Carlo code, at least in some critical zones shown in the present study. Such recalculations would decrease the uncertainty of biological dose rate to a reasonable level, namely the safety factor of 10 adopted during ITER CDA or even less than 10.

12. The safety factors for the biological dose calculations have to be seriously reevaluated during ITER EDA. It is suggested that a safety factor of biological dose would be established depending on the distance from the plasma core as well.

Acknowledgements.

This work was done as a part of ITER CDA-based neutronics analysis conducted in JAERI to support the work during the ITER EDA.

The authors wish to acknowledge the support and encouragement of Dr. S. Matsuda and other members of Department of ITER Project. The authors also want to thank Drs. K. Koizumi, M. Sawa, K. Shimizu, T. Okazaki, T. Hashimoto and N. Kanamori for providing the information developed in Japan after ITER CDA designs of the PF and the TF magnets, the cryostat, the divertor, the vacuum vessel etc. Helpful discussions with Dr. T. Kuroda are appreciated as well.

References.

1. ITER Conceptual Design Report, ITER DS Nº 18.

2. A. J. Glass, "Status and Plans for ITER", Journal of Fusion Energy, Vol. 11, Nº2, 1992.

3. ITER Blanket, Shield and Material Data Base, ITER DS Nº 29.

4. Y. Seki, H. Kawasaki and S. Mori, "Radiation Shielding Considerations for the Repair and Maintenance of a Swimming Pool-type Tokamak Reactor", Nuclear Engineering and Design/Fusion 1(1984) 243-253.

5. K. Maki, "Shielding Design for Fusion Experimental Reactor", JAERI-M 91-017, February 1991 (in Japanese).

6. S. Matsuda et al., "Conceptual Design Study of the Fusion Experimental Reactor (FER)", Proc. 13th Int. Conf. Plasma and Controlled Nuclear Fusion Research, Washington, DC, U.S., IAEA-CN-53/G-2-2 (1990).

7. "U.S. Technical Report for the ITER Blanket/Shield", July/November 1990, Garching, FRG, ITER-TN-BL-5-0-6.

8. O. L. Shchipakin et al., "ITER Biological shielding", Contribution to the Workshop on Nuclear Engineering, Garching, ITER-IL-NE-7-0-1, February of 1990.

9. O. L. Shchipakin, "Biological Shield and Radiation Dose Rates During ITER Maintenance", Presented at the Nuclear Engineering Working Group, Garching, ITER-IL-BL-4-0-16, August 1990.

10. S. Zimin et al., "Some ITER Shield Problems Examination", JAERI-M 92-063 (May 1992).

11. E. Salpietro et al., "Next European Torus Basic Machine", Fusion Technology, Vol. 14, p. 58, July 1988.

12. M. Sawa et al., "Structural Design of Cryostat and Port Penetration of International Thermonuclear Experimental Reactor (ITER)", JAERI-M 92-094, July 1992 (in Japanese).

13. K. Maki et al., "Japanese Contributions to ITER Shielding Neutronics Design", JAERI-M 91-046, March 1991.

14. H. Takatsu et al., "Layered Pebble Bed Concept for ITER Breeding Blanket", 17th SOFT, Roma, Sep. 14-18, 1992.

15. K. Shibanuma et al., "Japanese Contributions to Containment Structure, Assembly & Maintenance and Reactor Building for ITER", JAERI-M 91-080, June 1991.

16. T. Okazaki et al., "Design of Divertor Support Structure", JAERI-M 92-108, July 1992 (in Japanese).

17. Bottura et al., ITER Magnets, ITER DS Nº 26, IAEA, Vienna, 1991.

18. A. B. Chilton, J. K. Shutlis and R. E. Shaw, "Principles of Radiation Shielding", Printice-Hall, Englewood Cliff, NJ (1984).

19. W. A. Rhoades and F. R. Mynatt, The DOT-III two dimensional discrete ordinates transport code, IRNL/TM-4280 (1973).

20. K. Maki et al., "Nuclear Group Constant Set FUSION-J3 for Fusion Reactor Nuclear Calculations Based on JENDL-3", JAERI-M 91-072, 1991 (in Japanese).

21. K. Koizumi et al., "DOG-II : Input Generator Program for DOT3.5 Code", JAERI-M 92-106, August 1992 (in Japanese).

22. H. Kawasaki, K. Maki and Y. Seki, "APPLE-3 : Improvement of APPLE for Neutron and Gamma-ray Flux, Spectrum and Reaction Rate Plotting Code, and of Its Code Manual", JAERI-M 91-058, 1991 (in Japanese).

23. H. Iida and M. Igarashi, THIDA-code system for calculation of the exposure dose rate around a fusion device, JAERI-M 8019 (1978).

24. H. Fukumoto, "New Approach to Neutron-Induced Transmutation, Radioactivity and Afterheat Calculations and Its Application to Fusion Reactors", Journal of Nuclear Science and Technology, **23**[2], p. 97-109 (February 1986).

25. S. Mori, Private communication, JAERI, October 16, 1992.

26. "1990 Recommendations of the International Commission on Radiological Protection", ICRP Publication 60, Published for the International Commission on Radiological Protection by Pergamon Press, 1991.

27. T. Kuroda et al., "ITER Plasma Facing Components", ITER Documentation Series, Nº 30, IAEA, Vienna 1991.

28. S. Mori, Private communication, JAERI, October 26, 1992.

29. K. Maki, Private communication, JAERI, October 26, 1992.

30. W. W. Engle, "A User's Manual for ANISN - A One Dimensional Discrete Ordinates Transport Code with Anisotropic Scattering", K-1693 (1967).